A CARBON NANOTUBE OPTICAL RECTENNA FOR ENERGY HARVESTING

A Dissertation
Presented to
The Academic Faculty

by

Erik C. Anderson

In Partial Fulfillment
of the Requirements for the Degree
Doctor of Philosophy in the
George W. Woodruff School of Mechanical Engineering

Georgia Institute of Technology
August 2020

A CARBON NANOTUBE OPTICAL RECTENNA FOR ENERGY HARVESTING

Approved by:

Dr. Baratunde Cola, Advisor
G.W.W. School of Mechanical Engineering
Georgia Institute of Technology

Dr. Zhuomin Zhang
G.W.W. School of Mechanical Engineering
Georgia Institute of Technology

Dr. Matthew McDowell
G.W.W. School of Mechanical Engineering
Georgia Institute of Technology

Dr. Eric Vogel
School of Materials Science and Engineering
Georgia Institute of Technology

Dr. John Cressler
School of Electrical and Computer Engineering
Georgia Institute of Technology

Date Approved: July 6, 2020

I dedicate this work to my parents

ACKNOWLEDGEMENTS

I first want to sincerely thank Dr. Baratunde Cola bringing me into his group and giving me the lead on this project which has allowed me to develop independence and grow myself as a researcher. I learned a lot more than research from him—Bara has been an unbelievable inspiration and motivator, challenging me to think of the big picture in addition to the science. I would also like to thank all the members of the NEST lab throughout the years. They have been a source of inspiration, wisdom, and friendship. A special thanks goes to Dr. Thomas Bougher for his guidance and supporting me as I learned my way around the lab. I also humbly thank my undergraduate researchers, Aalok Patel and Josh Preston, for their tireless work helping me with various aspects of this project. I would like to gratefully acknowledge my dissertation committee, Dr. Zhuomin Zhang, Dr. Matthew McDowell, Dr. Eric Vogel, and Dr. John Cressler for their time and effort.

Finally, I would like to thank my family for their support. My family has been a constant source of motivation throughout my life, and their endless encouragement has made everything that I do possible. Lastly, and most importantly, I express endless gratitude to my fiancée, Kelsey, who I will shortly call my wife. I stole many moments from her for the sake of this work while she was patient and put up with me throughout.

TABLE OF CONTENTS

LIST OF TABLES

LIST OF FIGURES

LIST OF SYMBOLS

A	nominal device area (m^2)
$\mathcal{A}$	asymmetry (*i.e.* rectification ratio) (-)
A_D	area of a single diode junction (m^2)
C_D	diode capacitance (F)
$D^\star$	specific detectivity (cm Hz$^{1/2}$ W^{-1})
d	thickness of tunneling barrier (m)
E	electron energy (eV)
e	electronic charge (1.602×10^{-19} J)
f	frequency (Hz)
f_c	cutoff frequency (Hz)
H	Hamiltonian (eV)
h	Planck's constant (6.626×10^{-34} J s)
$\hbar$	reduced Planck's constant (1.055×10^{-34} J s)
T_λ	spectral transmittance (%)
I	current (A)
I_D	diode d.c. current (A)
I_L	current of device under illumination (A)
I_{sc}	short-circuit current (A)
i	time-dependent current (A)
i	imaginary unit ($\sqrt{-1}$)
J_n	Bessel function of the first kind of order n (-)
k_b	Boltzmann constant (1.381×10^{-23} J K^{-1})
m_e	electron mass (9.11×10^{-31} kg)
$\mathcal{N}$	nonlinearity (-)
n,m	integers denoting multiphoton absorption and/or emission (-)
P_{in}	incident power; input power (W)
R	resistance (Ω)
R_A	antenna resistance (Ω)

R_D	diode resistance (Ω)
T	temperature (K)
t	time (s)
V	d.c. voltage; applied bias(V)
V_{oc}	open-circuit voltage (V)
V_A	antenna source voltage (V)
V_{ph}	photon voltage (V)
V_ω	a.c. diode voltage amplitude (V)

Greek Symbols

α	ratio of diode voltage to photon voltage (-)
β	diode responsivity (A W^{-1})
β_I	photocurrent responsivity (A W^{-1})
β_V	photovoltage responsivity (V W^{-1})
ε_r	dielectric constant (-)
ε_0	vacuum permittivity (8.854×10^{-12} F m^{-1})
ϵ	relative error (-)
η	power conversion efficiency (-)
η_A	antenna radiation efficiency (-)
η_{AD}	antenna-diode coupling efficiency (-)
η_D	diode rectifier efficiency (-)
η_{imp}	antenna-diode impedance matching efficiency (-)
η_{RC}	RC coupling efficiency (-)
λ	wavelength (nm)
ρ_n	CNT number density (CNT/m^{-2})
Φ	work function (eV)
φ	potential barrier height (eV)
χ	electron affinity (eV)
Ψ	time-dependent wavefunction (-)

ψ	wavefunction (-)
ω	angular frequency (rad s^{-1})
ω_c	angular cutoff frequency (rad s^{-1})
$\omega_c^\star$	effective cutoff frequency (rad s^{-1})
ω_p	plasma frequency (rad s^{-1})

LIST OF ABBREVIATIONS

a.c.	alternating current
ALD	atomic layer deposition
CIM	carbon nanotube–insulator–metal
$\text{CI}^{(m)}\text{M}$	carbon nanotube–multi-insulator–metal
CNT	carbon nanotube
CVD	chemical vapor deposition
LPCVD	low pressure chemical vapor deposition
d.c.	direct current
EDS	energy dispersive X-ray spectroscopy
FNT	Fowler-Nordheim tunneling
FOM	figure of merit
IR	infrared
I–V	current–voltage
MIM	metal–insulator–metal
MIR	mid-infrared
NIR	Near-infrared
PAT	photon-assisted tunneling
PDMS	polydimethylsiloxane
PEDOT:PSS	poly(3,4-ethylenedioxythiophene) polystyrene sulfonate
PHz	petahertz
PV	photovoltaic
Rectenna	rectifying antenna
RF	radio frequency
RIE	reactive ion etching
TEM	transmission electron microscopy
THz	terahertz
SEM	scanning electron microcopy
STEM	scanning transmission electron microscopy
VACNT	vertically aligned carbon nanotube

SUMMARY

The conversion of light to electricity has important applications in solar and thermal energy harvesting and detection. The optical rectenna (*rectifying antenna*) is a unique concept that researchers have been investigating as an alternative to photovoltaic technologies. Comprising an antenna coupled to a rectifying diode, rectennas that can operate at optical frequencies offer potential advantages in the way of enhanced conversion efficiency and lower cost of materials and fabrication. However, optical rectennas have been elusive since the first conceptualization in the 1970s. The challenge of realizing an optical rectenna is in fabricating both a nanoscale antenna that can efficiency absorb light and an ultrafast rectifying diode capable of rectifying the a.c. antenna signal into d.c. electricity. In 2015, Cola *et al*. provided the first demonstration of optical rectification, accomplished using a forest of vertically aligned carbon nanotubes (CNTs), which act as nanoscale antennas with excellent absorption properties. CNT–insulator–metal tunneling diodes fabricated atop the array are ultrafast rectifiers that are responsible for the a.c-to-d.c. conversion. The conversion efficiency of monochromatic visible light was limited to ~10^{-7} % due factors such as antenna-diode impedance mismatch, optical transmission losses, diode performance limitations, and the use of materials that are not stable in air.

This dissertation seeks to overcome these limitations. First, the CNT–insulator–metal tunneling diode structure investigated with the aim of improving electrical characteristics. The effect of the tunneling barrier dimensions on diode properties was studied by means of insulator thickness and electron affinity. Further, incorporating multiple layers of dielectric to tune tunneling was found to enhance asymmetry to upwards of >100 while bypassing the typical work function constraints from the CNT and metal electrodes. This important result facilitated more electrode choices—especially air-stable metals—while simultaneously achieving great asymmetry. This finally translated to the first optical rectification demonstration in air as well as a 10-fold increase in efficiency.

Next, these CNT rectennas composed of multi-insulator tunneling diodes were tested over the full range of visible wavelengths to realize spectral conversion efficiencies above 10^{-5} %; voltage responsivity was significantly improved up to 250 V/W. The photon-

assisted tunneling theory of rectenna operation was modeled and applied to these experimental results. In light of measurements, the model provided strong evidence that the CNTs operate as wavelength-dependent antennas. This further suggested a tradeoff between antenna-limited and diode-limited performance to guide future device optimization.

The broadband rectification picture was captured by initially studying dichromatic photon assisted tunneling theory and comparing simulated results to dual-wavelength measurements. Results show an overall decrease in the photoresponsivity in comparison to peak monochromatic photoresponsivity; this is attributed to frequency mixing in light of the photon assisted tunneling theory. Moreover, the full broadband solar spectrum is tested under direct sunlight, revealing solar conversion efficiency of 5.3×10^{-6} %. The implications of these optical tests involving the multi-barrier structure suggest that significant inefficiencies still remain within the diode—primarily arising from the high resistance that was necessary to realize stable devices in the lab.

Lastly, a new generation of CNT rectenna device structure was created to overcome existing commercialization limitations. Vertically aligned CNT forests were infiltrated with polymer to encapsulate and planarize the CNT tip surface. This facile method lends itself to fabrication simplicity and practical application with the facilitation of new materials and geometries. The embedded polymer–CNT structure employs PEDOT:PSS as a solution-processable transparent electrode. Diodes fabricated atop the planar surface were characterized for electrical properties and sample production yield. These multi-insulator planar diodes were shown to enhance asymmetry by a factor of 2× for two-barrier and 5× for four-barrier diodes, relative to a single-insulator device. These polymer–CNT diodes were used to provide a demonstration of optical rectification at 638 nm, exhibiting photoresponsivity of $\beta \sim 0.65$ µA/W. Inevitably, findings from this new generation of CNT rectenna are promising for a variety of flexible optoelectronic applications.

In summary, this work provides a number of materials investigations and device developments leading to important experimental confirmation of rectenna theory that was unverifiable until now. This progress will ultimately enable better solar and thermal energy harvesting in CNT rectenna devices.

CHAPTER 1. INTRODUCTION

1.1 Research Motivation

The increasing demand on clean energy has pressured the emergence of solar technologies to exploit solar radiation for the production of electricity. The sun provides a constant source of energy to the Earth at about 100 mW/cm^2. Photovoltaic (PV) solar cells have been a mature technology for direct conversion of solar energy into electricity. However, the efficiency of PV solar cells is bounded by the Shockley-Queisser limit to 30 % for single-junction and 55 % for multi-junction solar cells [1]. The materials used in solar cells can have toxicity concerns and processing limitations that make scaling up solar cell research to commercial scales a challenge. For these reasons, alternative solar conversion technologies are attractive to researchers.

The rectenna (*rectifying antenna*) has been proposed as an alternative technology for solar energy harvesting and has been gathering attention of researchers in the last several years [2]. A rectenna features an antenna coupled to a rectifying diode: the antenna absorbs freely propagating electromagnetic radiation which induces an alternating current within. As this a.c. current travels through the diode, it is rectified into useable d.c. power [2]. The components of a classical rectenna are depicted in Figure 1.1.

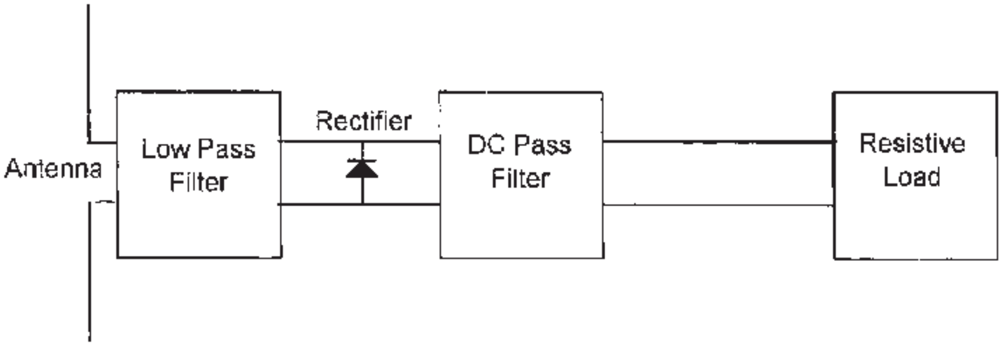

Figure 1.1. The block diagram of a rectenna attached to a load. Reprinted with permission from [3].

The rectenna was first demonstrated by William Brown in 1964 for microwave power transmission, used to wirelessly power a small helicopter (Figure 1.2). The rectenna device consisted of an array of half-wave dipole antennas, connected to semiconductor diode bridge rectifiers. Nowadays rectennas devices are well established for microwave frequency applications and capable of efficiencies in excess of 80 % [4].

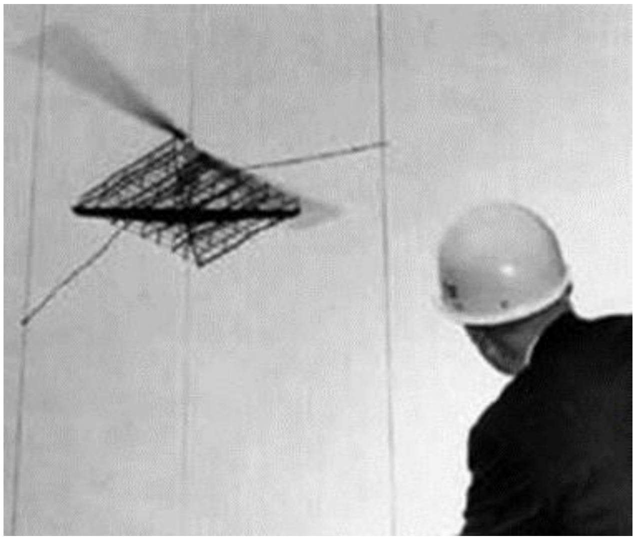

Figure 1.2. Brown’s demonstration of wireless microwave power transmission.

1.1.1 Optical Rectenna Background

The idea of an optical frequency rectenna was initially conceived by Richard Bailey in the 1970s [4]. He originally described conical dipole antennas each connected to a rectifying diode, designed to operate at solar frequencies (Figure 1.3). Unlike semiconductor-based PV cells which are based on the quantum nature of light and are therefore bandgap limited, optical rectennas are primarily based on the wave nature of light and are limited by semiclassical electromagnetic principles of operation [5]. Therefore, rectennas have been theorized to exceed the Shockley-Queisser limit of PVs [5–7].

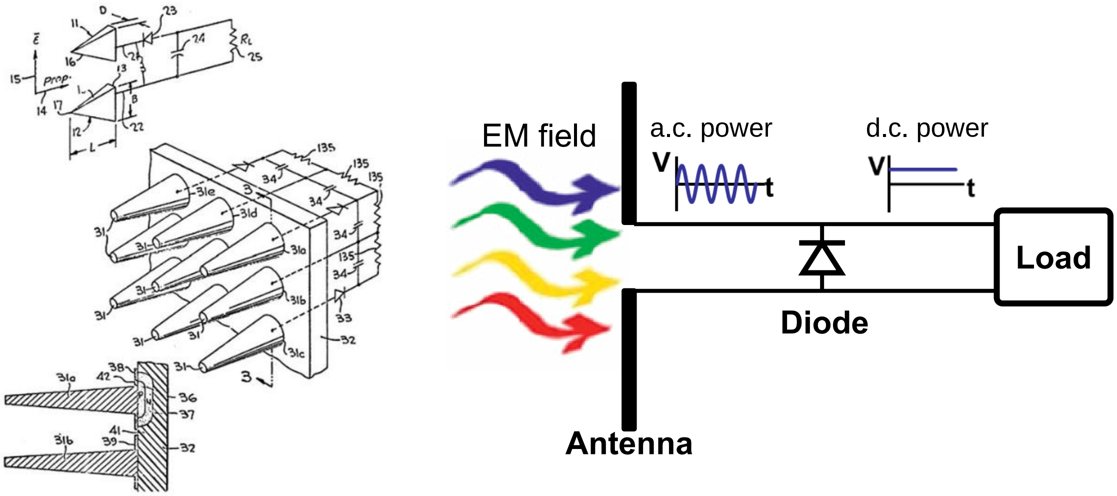

Figure 1.3. (left) Bailey's design for an electromagnetic wave energy converter for rectifying solar radiation. (right) Block diagram of optical rectenna, adapted with permission from [2].

Aside from solar-to-electrical energy conversion [8–12], optical frequency rectification is being researched for other applications such thermal energy harvesting [13, 14] (such as waste heat from high temperature sources), infrared (IR) sensing [15, 16], photodetection, imaging [17, 18], as well as power and information transmission at optical and IR frequencies [2, 19]. The latter application has specific motivation in Earth-to-space power transmission through the IR atmospheric window to overcome atmospheric losses.

Since Bailey's initial proof of concept, the optical rectenna as a solar cell has eluded practical demonstration for several decades. This is primarily due to limited ability to fabricate the nanoscale components needed for an optical rectenna—for instance, fabricating nanoscale antennas that are on the order of the wavelength of incident radiation.

Recent advances in nanoscale fabrication have rekindled interest in optical rectennas [2]. This includes attention devoted to progressing the theoretical understanding of optical rectification, such as studying the behavior of metals and nanostructures in the optical regime, and illuminating the similarities and discrepancies of optical rectification mechanisms versus established classical devices that work at low frequencies [6].

Finally, a breakthrough was reported in 2015 by Sharma *et al*. Led by Baratunde Cola, researchers at Georgia Institute of Technology provided a successful demonstration of optical energy conversion using a carbon nanotube (CNT)-based rectenna [8]. Cola and his team introduced arrays of metallic CNTs as minute antennas with rectifying tunnel diodes fabricated at the tips. The work in this dissertation is an extension of the work originally performed by Cola *et al*.

Other recent investigations that have advanced the field of rectennas include the following: Ward *et al.* [20] studied optical rectification in plasmonic nanogaps. They observed a 1000-fold field enhancement that drove the rectification and observed a photocurrent responsivity of 0.3 nA kW^{-1} cm^2. Briones *et al.* [7] studied arrangements broadband nanoantenna arrangements, reporting a low coupling ratio of 10^{-9} between the diodes (MIM and Esaki) and the nanoantennas. In this case, they attributed the impedance mismatch and the inefficient diode parameters as the main contributors to the low performance. Other bowtie nanoantenna-coupled tunneling diodes have been developed for 28.3 THz. Such as an $Au/Al_2O_3/Pt$ tunneling structure that has shown responsivity of 10 A/W [11]. Researchers from Sandia National Laboratories described power generation from radiating thermal sources using a metal-grating nanoantenna structure coupled to a tunneling diode [14, 21, 22]. The grating leverages epsilon-near-zero effects to confine and enhance incident thermal radiation into the tunneling barrier. They demonstrated 8 nW/cm^2 for a blackbody source at 450 °C. Geometric diodes, proposed by Moddel [23], are designed to meet the impedance matching and low diode capacitance requirements for rectification. They have developed a geometric diode based on graphene, then coupled to a bowtie antenna configuration. A responsivity as high as 0.2 A/W was realized at for 10.6 µm radiation [12].

1.1.2 Design Considerations for Optical Rectennas

For microwave rectennas, the component dimensions need only be microns. However, to operate at optical frequencies the rectenna requires nanoscale dimensions: The challenges and design consideration that need to be met for efficient optical rectification include the following [2].

- An antenna capable of efficiently absorbing optical wavelengths is necessary. This requires a minute antenna with dimensions that are on the length scale of the incident wavelength. It is also necessary to consider the properties of metals at optical frequencies, particularly the high ohmic losses that can occur in optical antennas.

- The rectifying diode must have a response time corresponding to nearly petahertz (PHz) frequencies. There are several supposed approaches to satisfying this requirement. Directly, this can be achieved by making the diode extremely small in order to reach attofarad capacitance which results in the necessary femtosecond diode response time.

- Impedance matching between the antenna and diode elements is also critical to ensure efficient power transfer. The effect of impedance mismatch due to substantially high diode resistance is perhaps the biggest bottleneck affecting efficient conversion.

These considerations put strain on the nanofabrication limits needed to create such necessarily small and fast components. The diode has been of particular hindrance to optical rectenna development. For instance, common lithographic Schottky diodes are not suitable for optical rectification because their cutoff frequency is limited to low THz due to depletion capacitance. Instead, a variety of alternative diode concepts have been researched that may be suited for optical rectification. Some promising technologies that researchers have investigated include geometric diodes, which are inverted arrowhead-shaped electrodes that preferentially funnel the current in one direction [23–25]; traveling-wave diodes, which feed the antenna source as a surface plasmon wave through parallel transmission lines [9]; and metal–insulator–metal (MIM) tunneling diodes.

To address these design requirements, I will next introduce carbon nanotubes as a material that has proven to be advantageous for optical rectennas.

1.2 Overview of Carbon Nanotubes

Since the discovery by Iijima in 1991 [26], carbon nanotubes (CNTs) have been of tremendous interest. As one-dimensional nanostructures, CNTs are one of the most important and promising materials to nanoelectronics and optoelectronics because of their remarkable optical, electrical, and mechanical properties. Often depicted as a cylindrically rolled up sheet of graphene, CNTs have diameters usually around 10's of nanometers and lengths that are typically on the order of microns. Depending on their chirality, the band gap of single-wall CNTs can range from semiconducting to metallic. However, multiwall CNTs (MWCNTs) are ordinarily metallic due to the statistical presence of different chiralities within coaxial nanotubes [27]. Aside from outstanding mechanical strength (specific strength ~48,000 kN-m/kg), CNTs also have high thermal conductivity (3000 W/m-K) and electrical conductivity (>10^6 S/m), as well as chemical stability [28, 29]. These properties have garnered attention for applications in nanoscale interface materials, transistors, PV solar cells, and many others.

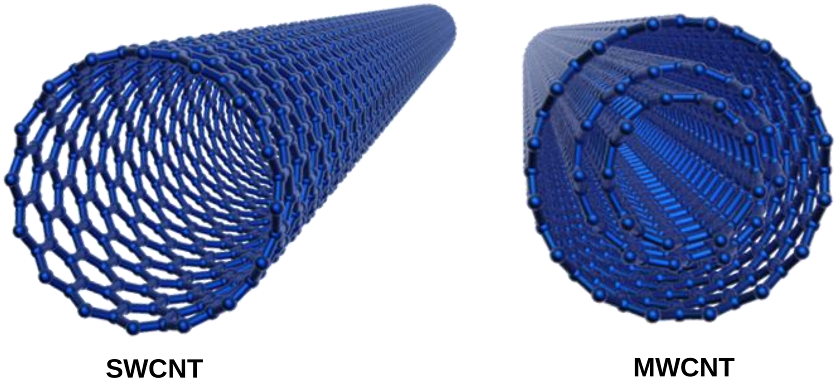

Figure 1.4. Depictions of a single-wall and multiwall carbon nanotube.

It is also possible to fabricate arrays of vertically aligned CNTs, which is the variety of CNT that is the focus of this work. Vertically aligned CNT forests are advantageous in optical rectennas as a contributing component to both the antenna and diode components:

Antenna: Arrays of metallic CNTs make exemplary optical antenna elements owing to their small size, high mobility, and extraordinary facility of multiwall CNTs to broadly absorb electromagnetic energy. Arrays of aligned CNTs have been shown to demonstrate antenna-like interactions with electromagnetic radiation, exhibiting polarization dependence and antenna-length effects [30–34].

Diode: Aside from the good electrical conductivity of CNT arrays, the minute size of CNTs give them their greatest utility when used for rectifying diodes. As will be elaborated later on, the nanometer scale of the CNT tips facilitates an ultra-small area that is a critical component of attaining an ultrafast rectifying diode.

1.3 Dissertation Outline

This dissertation is a substantial extension of the CNT optical rectenna originally reported by Sharma *et al*. This work presents improvements to the CNT rectenna design and our fundamental understanding of rectenna operation. Devices were mainly fabricated as aligned CNT forests grown on Si wafers. CNT-based metal–insulator–metal tunneling diode structures were created along the CNT tips. This body of work focuses on advancements using air-stable materials. The following is an outline of this dissertation.

Chapter 2 provides relevant background information on optical rectennas, including the classical rectenna picture, an overview of the individual antenna and diode components and recent approaches, and theory of the optical rectification through photon-assisted electron transport. Lastly, this chapter introduces the carbon nanotube rectenna device as the first rectenna demonstration of optical power conversion, also presenting outstanding issues that motivate this dissertation.

Chapter 3 explores the CNT tunneling diode with the goal of improving the diode characteristics. This includes studying the influence of the electron tunneling barrier on diode performance, principally via the dielectric thickness and dielectric material choice.

Chapter 4 expands on the previous study by investigating CNT diodes utilizing multiple dielectrics in combination to further enhance diode tunneling characteristics. Multi-insulator CNT diodes were examined with a variety dielectric combinations and insulator thickness to enhance electrical performance.

Chapter 5 demonstrates air stable optical rectification using performance-enhanced multi-insulator CNT devices. Power conversion of monochromatic light is discussed with respect to the diode figures of merit.

Chapter 6 presents a model of rectenna optical response developed using photon-assisted tunneling theory. The simulated response is presented in light of experiments to explain and validate optical measurements. A related efficiency analysis is conducted to elucidate routes for future improvements in optical power generation.

Chapter 7 studies broadband rectification, specifically by exploring rectification under dual-wavelength illumination. This chapter uses the insight gained from the monochromatic rectification studies in Chapter 6 to simulate the dichromatic photon-assisted tunneling response and compare to measurements. Lastly, a demonstration of broadband solar conversion is provided under real-life conditions.

Chapter 8 investigates infiltrating CNT forests with insulator media with the goal of planarizing the CNT tip surface and facilitating fabrication ease and commercialization potential. Specifically, this chapter examines infiltration with polymer media and subsequent fabrication of planar CNT tunneling diode arrays with polymer electrodes, which are ultimately used to demonstrate proof-of-principle optical rectification.

Chapter 9 describes broader applications of the CNT rectenna besides solar energy harvesting. This includes the potential of CNT rectennas for infrared detection and harvesting, power transmission, and other novel technologies.

Chapter 10 concludes the dissertation with a summary of key findings and provides recommendations for future research.

CHAPTER 2. RECTENNA BASICS

This chapter provides an introduction to the core concepts of the rectenna—starting from the classical microwave rectennas and extension to optical frequencies, an overview of both nanoantenna and rectifying diode components, and the principle theory of optical rectification.

2.1 Rectenna Classical Operation

Low frequency rectification is often classically depicted as an a.c. voltage oscillation traveling through the diode component that has sufficient nonlinearity to generate a net d.c. current. The rectification mechanism is the result of the diode asymmetry inhibited the a.c. current flow in one direction and allowing current to pass through the other direction.

The classical response of a rectenna can be found for incoming radiation that is picked up in the antenna which induces a small sinusoidally alternating voltage across the coupled diode, V_ω, along with the d.c. applied bias. In the case of a MIM tunneling diode, this is understood as a modulation in the Fermi level at either side of the potential barrier. The time-dependent current that arises from the a.c. signal is given through the d.c. current, $I(V_{dc})$, as

$$i_L(t) = I(V_{dc} + V_\omega \cos(\omega t)). \tag{2.1}$$

By performing a Taylor expansion on equation (2.1), the a.c. modulated current is

$$i_L(t) \approx I(V_{dc}) + V_\omega \cos(\omega t) \left.\frac{dI}{dV}\right|_{V_{dc}} + \frac{1}{2} V_\omega^2 \cos^2(\omega t) \left.\frac{d^2 I}{dV^2}\right|_{V_{dc}} + \cdots \tag{2.2}$$

The expression for the net d.c. current flowing through the diode is found by calculating the time-averaged current under the a.c. illumination, $I_L = \langle i_L(t) \rangle$. The result is the classical response for small-signal rectification:

$$I_L \approx I(V_{dc}) + \frac{1}{4} V_\omega^2 \frac{d^2 I}{dV^2} = I(V_{dc}) + I_{rect}. \tag{2.3}$$

Equation (2.3) can be expressed in terms of the diode resistance, $R_D = \left(\frac{dI}{dV}\right)^{-1}$, and responsivity, $\beta = \frac{\frac{1}{2}\left(\frac{d^2I}{dV^2}\right)}{\frac{dI}{dV}}$. wherein the rectified current is found to be

$$I_{rect} = \frac{V_\omega^2}{2}\left(\frac{\beta}{R_D}\right) \tag{2.4}$$

and the maximum output power is

$$P_{out} = -\frac{V_\omega^4\, \beta^2}{16\, R_D}. \tag{2.5}$$

Equation (2.4) is the classical square-law rectification ($I_{rect} \propto V_\omega^2$) that portrays the rectified current as dependent upon the square of the a.c. voltage signal produced in the diode. Equations (2.4) and (2.5) highlight the significance of the diode properties on the rectified current: the rectified power depends upon the responsivity of the diode and the strength of the a.c. voltage (which is controlled by the power of the input signal), while diode resistance adversely impedes power rectification.

2.1.1 Rectenna Circuit

Sanchez *et al.* developed an approach for antenna-coupled MIM diodes to rectify small signals at microwave frequencies. They used an equivalent circuit to model to the antenna receiver as a voltage source in parallel with the diode. This model facilitated calculations to optimize the power transfer between antenna and diode for microwave and IR frequencies. This rectenna circuit is useful tool to understand the requirements and limitations for high frequency rectification.

The rectenna equivalent circuit is represented by an antenna in parallel with the rectifying diode (Figure 2.1). The antenna is represented as a small-signal a.c. voltage source of magnitude V_A oscillating at the frequency of the incoming radiation, ω. This antenna voltage is calculated according to

$$V_A = \sqrt{8R_A P_{in}}. \tag{2.6}$$

P_{in} is the input power received by the antenna. The antenna radiation resistance, R_A, depends upon the antenna geometry as well as conductive and dielectric losses from the antenna material. In order to reduce ohmic dissipation in the antenna and improve the radiation efficiency, radiation resistance should be larger than ohmic resistance in the antenna. It is also pointed out that the power received by the antenna is not necessarily identical to the incident power of the radiation source, rather, incoming efficiency losses must also be accounted for. These may include power transmission loss through a semi-transparent top electrode as well as antenna radiation efficiency. For simplicity, this rectenna model assume the power received in the antenna is the same as the incident power unless otherwise noted.

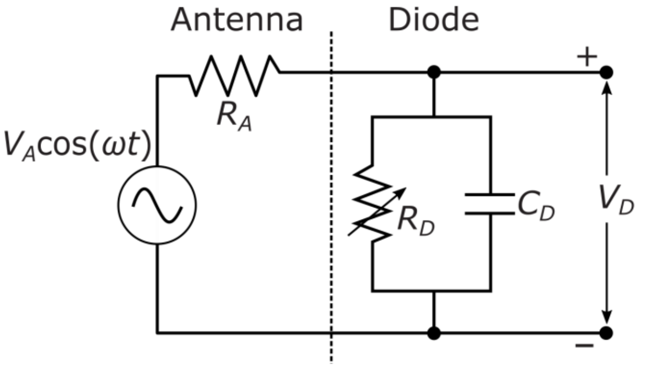

Figure 2.1. Antenna-coupled diode equivalent circuit representation of optical rectenna.

The rectifier is modelled by a nonlinear resistor, R_D, in parallel with a capacitor, C_D, which accounts for the switching time of the diode. Based on this equivalent circuit, the voltage developed across the diode is found from voltage division using the antenna and diode impedances (Z_A and Z_D, respectively):

$$V_D = V_A \frac{Z_D}{Z_D + Z_A} = V_A \frac{R_D}{(R_A + R_D + i\omega R_A R_D C_D)} \ . \tag{2.7}$$

The power transferred from the antenna to the diode depends is subject to coupling loss. Hence, the antenna-to-diode coupling efficiency can be found in taking the ratio of the power received by in the diode, P_D, to the antenna input power:

$$\eta_{AD} = \frac{P_D}{P_A} = \frac{V_D^2/2R_D}{V_A^2/8R_A}. \tag{2.8}$$

For this system with the antenna in parallel with a rectifying diode, the coupling efficiency alludes to the operating frequency of a rectenna. In terms of R_A, R_D, and C_D the coupling efficiency between the antenna and diode is [35]

$$\eta_{AD} = \frac{4\frac{R_A R_D}{(R_A + R_D)^2}}{1 + \left(\omega \frac{R_A R_D}{R_A + R_D} \mathrm{C_D}\right)^2} = \frac{4\frac{R_A R_D}{(R_A + R_D)^2}}{1 + \left(\frac{\omega}{\omega_c}\right)^2} \tag{2.9}$$

where ω_c is the angular cutoff frequency evaluated by

$$\omega_c = 2\pi f_c = \frac{1}{\bar{R} C_D} = \frac{R_A + R_D}{R_A R_D\, C_D} \approx \frac{1}{R_A C_D}. \tag{2.10}$$

where $\bar{R} = R_A || R_D$ is the equivalent resistance of R_A in parallel with R_D. The rightmost approximation in equation (2.10) arises when the diode resistance is much larger than the antenna resistance, $R_A \ll R_D$. This is often the case for MIM diodes which have high tunneling resistance. Hence, this approximation will be predominantly used in this work unless noted otherwise.

The coupling efficiency term is crucial to our understanding of the rectenna operating limits. To gain a better picture of this, η_{AD} can be further distributed into an impedance matching component

$$\eta_{imp} = \frac{4R_A\, R_D}{(R_A + R_D)^2} \tag{2.11}$$

and an RC component that reflects the effect of the diode’s finite cutoff frequency

$$\eta_{RC} = \frac{1}{1 + \left(\frac{\omega}{\omega_c}\right)^2}. \tag{2.12}$$

The impedance matching between the diode describes how much loss is incurred in the transmission of the a.c. antenna power once delivered to the diode for rectification. The power transfer is maximized when $R_A = R_D$, which is to say perfect impedance matching between antenna and diode elements: $\eta_{imp}(R_A = R_D) = 1$. In reality however, the diode resistance is usually significantly higher than R_A. With R_A generally on the order of ~100 Ω, the impedance matching efficiency term can be approximated as

$$\eta_{imp}(R_A \ll R_D) = \frac{4R_A}{R_D}. \tag{2.13}$$

The implication of equation (2.13) shows that the diode resistance has a significant effect on impedance mismatch. This has been a highlight of many optical rectenna reports. Mitigating the impedance mismatch by improving the diode is one of the primary motivations of this dissertation.

η_{RC} signifies the operating regime of the rectenna due to a finite diode response time. When the incident frequency is above the cutoff frequency, ω_c, efficiency will drop off on the order of $\eta_{RC} \sim \left(\frac{\omega}{\omega_c}\right)^{-2}$. Therefore, a high cutoff frequency is critical to rectifying optical light. It then follows that to achieve high conversion efficiency capacitance should be minimized. Assuming the capacitance relation for a planar junction, $C_D = \frac{\varepsilon\varepsilon_0 A}{d}$, efficiency coupling can be realized by reducing the junction area of the diode. For optical radiation, attofarad capacitance is required, which necessitates nanoscale device dimensions [8, 12, 25].

Therefore, in order to efficiently rectify optical frequencies, *both* the antenna and diode components must be considered. Sections 2.2 and 2.3 will cover the individual antenna and diode components in more depth.

2.2 The Antenna

Antennas have been widely used across a range of frequencies for the collection or transmission of electromagnetic radiation. Conventional radio frequency (RF) antennas convert freely propagating electromagnetic waves into guided signals within the metal antenna elements. As discussed earlier, Bailey's innovative concept using optical antenna-coupled diodes was the first proposed idea that leveraged the wave-nature of light for harnessing solar power. Several types of nanoscale antennas have since been developed to accomplish this goal, including but not limited to whisker, dipole, spiral, and bowtie antennas.

Optical nanoantennas—functioning at infrared or visible frequencies—strongly enhance nanoscale light-matter interactions by efficiently converting freely propagating radiation into localized optical fields. This is the operating principle for the absorption of incident light in an optical rectenna. Research in nanoantennas for optical emission and absorption is motivated by advancements in plasmonics. These are fostering interest for other applications including photodetection, sensing, light emission, thermal energy transfer, wireless communication, and spectroscopy [19].

Dipole antennas are the simplest form of antenna featuring two thin, mirrored wires that operate under resonant conditions according to the dipole dimensions. However, dipole antennas are inferior to other more complicated antenna designs (*e.g.* bowtie, spiral, log-periodic) at efficiently absorbing broadband radiation and therefore pose an obstacle for broadband solar rectification.

Current understanding of nanoantennas is mostly based on concepts carried over from RF antenna theory. A nanoantenna's geometric structure and dimensions are closely related to its absorption and polarization properties. The radiation efficiency of an antenna is given as the ratio of the radiated power to total power dissipated:

$$\eta_A = \frac{P_{rad}}{P_{tot}} = \frac{P_{rad}}{P_{rad}+P_{loss}}. \tag{2.14}$$

For efficient signal transmission, the antenna length should be similar to the wavelength of interest for efficient conversion. A have-wave dipole antenna, for instance should be made with length equal to λ/2 to achieve resonance and generate a local field enhancement that maximizes efficiency. Therefore, extension to optical wavelengths compels nanoscale dimensions [19].

The principles of RF antennas are well established, and can serve as a starting point to understand the optical frequency response of nanoantennas [36]. However, the wavelength scaling breaks down at optical frequencies because of the electronic properties of metals at optical frequencies no longer behave as perfect conductors. There is a lag in the electronic response in relation to the external field due to finite electron mass, which causes ohmic losses near the surface. Ohmic losses are proportional to the conductivity of the material, which in turn is related to the optical frequency dielectric constant. Using the Drude-Sommerfield model for a free electron gas, the optical frequency dielectric constant can be estimated by

$$\varepsilon(\omega) = \varepsilon_\infty - \frac{\omega_p^2}{\omega^2 + i\gamma\omega} \tag{2.15}$$

where ω_p is the plasma frequency of the metal and γ is a damping constant. Classical dipole antenna theory can be adjusted for nanoantennas operating at optical frequencies, wherein the metal plasma frequency is relevant, to entertain a modified effective wavelength, λ_{eff}, that may be calculated from a linear wavelength scaling rule [19, 37]:

$$\lambda_{eff} = n_1 + n_2\left(\frac{\lambda}{\lambda_p}\right) \tag{2.16}$$

where λ_p is the plasma wavelength and n_1 and n_2 are coefficients that depend on antenna geometry and static dielectric properties. This equation is valid for antenna radii smaller than the wavelength of light.

Current research into nanoantennas is driven by advances in fabrication. There are many emerging materials and concepts related to optical antennas. CNTs are particularly suited to address challenges in nanoantennas for optical frequencies.

2.2.1 Carbon Nanotubes as Nanoantennas

Metallic CNTs are great candidates as optical antennas for their electrical conductivity, naturally high aspect ratio, and ease of fabrication as a nanostructure [32, 38, 39]. CNTs have better conductivity than metals at the nanoscale (~10 nm diameter) which is needed for high frequency a.c. signals. Recent investigations, both theoretical and experimental, have established that various CNT structures are capable of behaving as nanoantennas—including isolated CNTs, bundles, and well-aligned arrays [30, 32, 40]. The high frequency electrical properties of CNTs are governed by intraband π–electron motion for THz and IR frequencies and interband π–electron transitions between valance and conductive zones for optical light. A broad THz conductivity peak has been monitored for both semiconducting and metallic single-wall CNT structures, which is an important quality for antenna applications as well as ultrafast optoelectronics in general.

It has been shown that metal nanotubes (such as multiwall CNTs) interact with light in the same manner as conventional dipole antennas [40]. In analyzing the antenna properties of graphene and CNTs, the Fermi velocity is usually taken as $\approx 0.01c$, where c is the speed of light. Then the plasma wavelength of CNT nanoantennas can be estimated as $\lambda_p \approx 0.01\lambda$. Analysis of nanoantenna arrays have suggested that the radiation resistance can be estimated by

$$R_{rad} = \frac{2\pi}{3} Z_0 \left(\frac{l_{eff}}{\lambda}\right)^2 . \tag{2.17}$$

Antenna radiation resistance is given as a function of wavelength λ, where $Z_0 = 120\pi\ \Omega$ is the characteristic impedance of free space, and l_{eff} is the effective antenna length which depends upon the angle of the antenna relative to the incident field and also accounts for the effective wavelength due to optical frequency scaling [41]. Researchers have shown that light absorption can benefit from optical density of a nanowire array. When nanorods and nanowires in an array are spaced closer together than the incident wavelength, an array effect forms that supports guided modes and plasmon-mediated interactions between nanotubes. Large enhancements in field distribution result that can shift the resonant absorption behavior.

One promising aspect of CNT nanoantennas is their ability to be easily grown in dense, aligned arrays. CNTs can be synthesized to control diam, length, and inter-tube spacing. Substitutional doping (such as N or B) is another way of chemically controlling antenna properties of CNTs [36]. Aligned CNTs have confirmed antenna-like interactions with electromagnetic radiation, exhibiting polarization dependence and antenna-length effects [30–34]. These effects can be controlled to tune CNT devices to various frequency-dependent applications.

Experimental demonstrations of aligned metallic CNT nanoantenna arrays have been performed at THz and near-IR (NIR) [30]. For instance, simulations by Lan *et al.*

showed that THz antenna gain increases with CNT antenna length. (Figure 2.2) [42]. In dense CNT arrays (spacing $\ll \lambda$) polarization effects are reduced. This is a result of diffusive scattering induced by near field antenna-antenna interactions, which obscures the well-defined lobe patterns. The fact that metallic multiwall CNTs have been proven to behave as optical antennas according to classical antenna analogy is promising for leveraging CNTs in a variety of optoelectronic structures.

It should be mentioned that this body of work does not aim to directly test the characteristics of the CNT nanoantenna array nor model the CNT nanoantennas. Rather, this dissertation will focus on providing preliminary, if not indirect, evidence of the CNT nanoantenna behavior through observations of rectenna power conversion. More controlled experiments and rigorous model are needed to validate the CNT nanoantenna array properties discussed in this work.

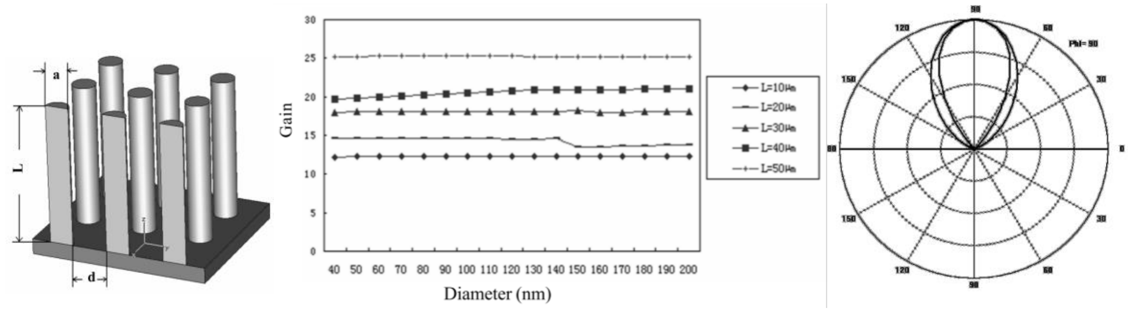

Figure 2.2. Model structure of an aligned CNT antenna array and the simulated antenna gain and directivity for 5 THz radiation. Adapted with permission from [42].

2.3 The Diode

The function of the diode in a rectenna is to rectify the a.c. signal provided by the antenna into d.c. to the load. It is therefore essential for a rectifying diode to have a response time that is sufficiently fast to match the incident frequency—in the case of optical rectification this amounts to femtosecond switching speeds and ultralow capacitance [34]. It has been a challenge to create a diode that can rectify optical frequencies. Schottky diodes are not suitable, as their limit of operation is only in the far IR. Several alternative types of diodes have been investigated by researchers in order to meet the RC frequency response requirements of the optical rectifier. Some of these promising approaches are discussed in this section.

The diode also has to have good electrical properties. This is quantified through the current–voltage (*I*–*V*) behavior of the diode. The typical figures of merit (FOMs) used to characterize the electrical performance of a diode are the dynamic resistance, R; asymmetry, $\mathcal{A}$; nonlinearity, $\mathcal{N}$; and responsivity, β. From a diode's *I*–*V* characteristics, these figures can be calculated by

$$R = \frac{1}{I'} \tag{2.18}$$

$$\mathcal{A} = \left|\frac{I(+V)}{I(-V)}\right| \tag{2.19}$$

$$\mathcal{N} = \frac{I'}{I/V} \tag{2.20}$$

$$\beta = \frac{1}{2}\frac{I''}{I'}\,. \tag{2.21}$$

As mentioned previously, diode resistance must be low to achieve good impedance matching with the antenna. For an antenna with $R_A \sim 100\ \Omega$, the coupling efficiency is below 1 % when with diode resistance is 10 kΩ. Asymmetry (also sometimes referred to as the rectification ratio) is a simple measure of the diode's rectifying ability based on the ratio between the forward- and reverse-bias currents. $\mathcal{A}$ quantifies the forward current in relation to the reverse bias leakage, values of $\mathcal{A} \sim 10$ or higher is desirable. Responsivity measures how efficiently the diode can rectify. Nonlinearity and responsivity are related to the curvature of the *I*–*V* characteristics.

The majority of this dissertation will focus on MIM diodes, which satisfy the femtosecond switching time required for optical rectification [43, 44]. A MIM diode is a thin film technology composed of two electrodes separated by a nanometer-scale insulator (*i.e.* a dielectric or oxide) to create a potential energy barrier through which electrons can tunnel. Dissimilar electrodes form a potential gradient within the barrier that produces asymmetric *I*–*V* response [45]. The thin barrier also gives the MIM diode low capacitance for necessarily ultrafast response time.

2.3.1 Metal-Insulator-Metal Diodes

The most popular rectifier being studied for optical rectennas is the metal–insulator–metal (MIM) diode. MIM diodes are composed of a thin insulator sandwiched between two metal electrodes. These diodes operate via nonlinear quantum mechanical tunneling of electrons through the insulating layer. The thickness of the insulator layer should be on the order of several nanometers to enable the principle tunneling mechanism. The electron tunneling is an extremely fast process: the tunneling time calculated from wavepacket propagation is estimated to occur on the order of 10^{-16} s [46]. The ultrafast response time is an advantage over semiconductor diodes. Thus, MIM diodes are promising for optical rectennas [46, 47] as well as other electronic applications that require operation in IR and THz regimes such as IR photodetectors [15, 16], switching memories [48–50], imaging and display devices [51, 52], and power transmission [2].

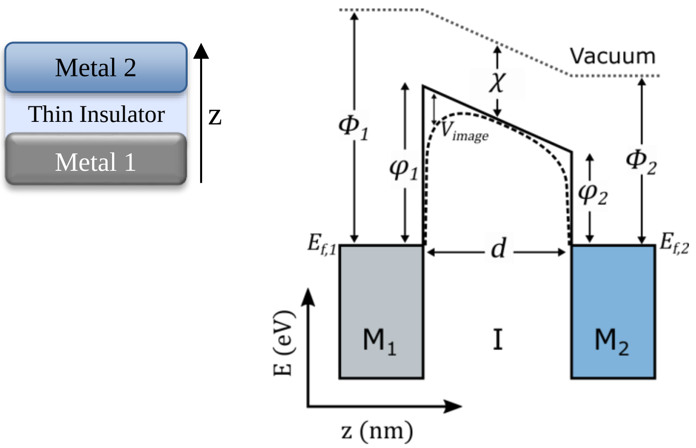

Figure 2.3. Potential energy band diagram for a MIM diode dissimilar metal electrodes, each described by their work function, Φ. The insulator has thickness d and electron affinity χ. The effect of image potential is shown as the dashed line.

The diode properties are determined by the shape of the potential barrier that is formed in the MIM, and therefore depend considerably on the choice of metals and insulator [53–57] (Figure 2.3). Good rectifying behavior is achieved by using two dissimilar metals such that the work function (Φ) difference between electrodes creates a gradient in the tunneling energy barrier that leads to asymmetric electron conduction. The insulator dielectric affinity establishes the height of the barrier ($\varphi = \Phi - \chi$) relative to the metal work functions.

Asymmetric *I*–*V* behavior is the result of nonlinear electron tunneling under an applied bias. As shown in Figure 2.4, under forward bias, electrons tunnel from around the fermi level of the first metal to the second metal, giving a net positive current. In contrast, under negative bias this condition is reversed, and net negative current is the result. However, the asymmetric potential barrier established by dissimilar electrodes means that the current is much lower due to a larger barrier that hinders electron tunneling under negative bias (essentially related to the area of the tunneling barrier).

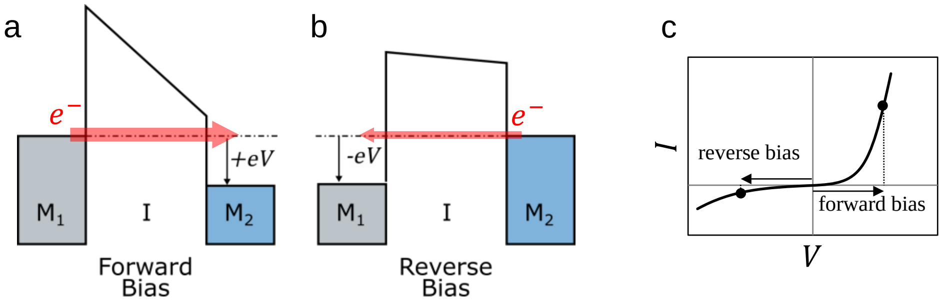

Figure 2.4. Energy band diagram for an asymmetric MIM under (a) forward bias and (b) reverse bias, along with (c) qualitative diode *I*–*V* behavior.

An ideal diode is difficult to achieve in practice due to conflicting characteristics of the FOMs and rectenna requirements. Generally, high nonlinearity and asymmetry is achieved using a thick insulator and a tall tunneling barrier (*i.e.* low χ) in combination with dissimilar electrode metal. However, tunneling resistance scales exponentially with the insulator thickness [58]. Furthermore, the selection of metals that have sufficient work function difference is often limited. The cutoff frequency must also be accounted for: C_D scales inversely with the dielectric thickness for a planar MIM, so making the insulator too thin will hinder high frequency operation. Balancing the electronic properties of MIM diodes has been the focus of much rectenna research [55, 59–62] and will make up a significant portion of this work.

2.3.2 *Double-Insulator MIM diodes*

An alternative way of achieving good diode properties can be accomplished by layering two or more insulators between the metal electrodes. In a double-insulator, or metal–insulator–insulator–metal (MIIM), configuration the tunneling barrier is based upon the properties of both dielectrics. Each layer forms a potential barrier with heights corresponding to the respective electron affinity value. Dissimilar insulators can thus form a highly asymmetric barrier. MIIM diodes have experimentally been shown to significantly enhance *I*–*V* asymmetry, nonlinearity, and responsivity versus a comparable single-barrier MIM [53, 62–64].

There are two primary mechanisms that govern tunneling phenomenon in MIIM structures: resonant tunneling and step tunneling. The mechanism depends upon the barrier structure and is sensitive to the applied bias. Resonant tunneling occurs when a triangular quantum well is created between barriers (Figure 2.5). The tunneling probability is substantially higher at the quantized resonant energy states. Therefore, when enough bias is applied such that the Fermi level of either metal coincides with a one of these bound energy states, electron tunneling is abruptly enhanced, leading to sharp turn-on in current that produces high asymmetry. The quantum well formed between insulators must be sufficiently deep and wide enough to form bound quantum states at reasonable bias [62, 65]. The turn-on voltage at which bound states form, and thus resonant tunneling begins, can be adjusted by changing the thickness of the first insulator, though a thick insulator will reduce tunneling current.

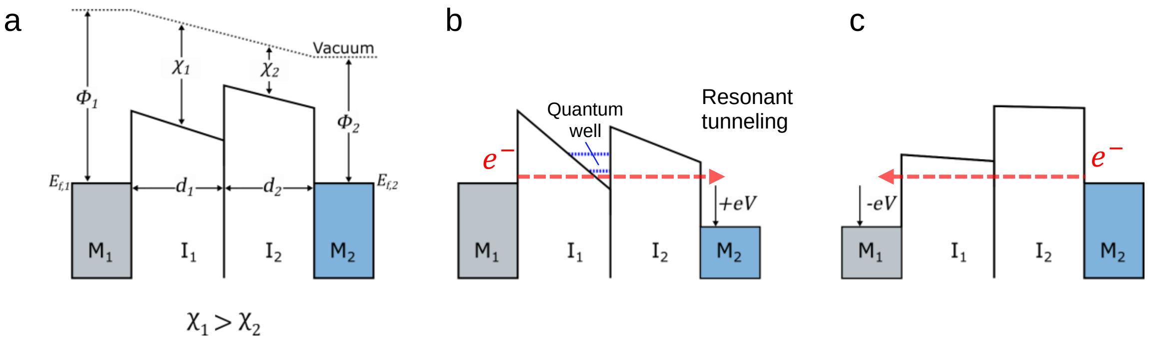

Figure 2.5. Illustration of resonant tunneling in a MIIM with $\chi_1 > \chi_2$. (a) Zero bias, (b) forward bias, and (c) reverse bias.

Step tunneling is the second mechanism that can induce asymmetric behavior in a MIIM (Figure 2.6). It is the result of a double-insulator stack creating a cascading potential barrier. Step tunneling occurs when enough bias is applied such that the lower of the two insulator barriers drops beneath the metal Fermi level. At this point electrons need only tunnel through the remaining, taller barrier [53]. This mechanism is largely polarity dependent because under the reverse direction electrons must tunnel through the full thickness of the double-barrier. The onset of step tunneling depends on the insulator thicknesses and value of the high electron affinity material, whereas the difference in insulator electron affinities influences the magnitude of asymmetry.

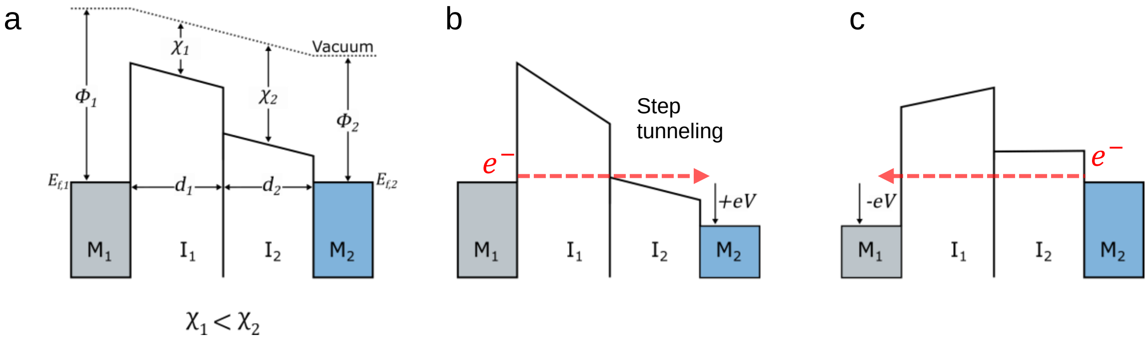

Figure 2.6. Illustration of step tunneling in a MIIM with $\chi_1 < \chi_2$. (a) Zero bias, (b) forward bias, and (c) reverse bias.

There has been a lot of work recently on MIIM diodes that have focused on experimentally testing or simulating planar devices with various metal and insulator combinations. Some combinations that have been explored include Ni/NiO/ZnO/Cr [66], Cr/Al_2O_3/HfO_2/Cr [54], Co/Co_3O_4/TiO_2/Ti [64], ZCAN/Al_2O_3/Ta_2O_5/Al [53], and ZCAN/HfO_2/Al_2O_3/Al [63]. Noureddine, *et al.* investigated MIIM devices with Al_2O_3 and Ta_2O_5 to optimize resonant tunneling. They reported asymmetry and nonlinearity values up to 8 with total barrier thickness below 5 nm [65]. Alimardani *et al.* combined defect-dominated conduction in a high electron affinity insulator with direct tunneling through a low affinity insulator to improve low-voltage asymmetry up to 10 and reaching a maximum of 187 at 1.2 V [53]. Aside from MIIM diodes, other combinations of multi-insulator MIM diodes have also been investigated. For instance, tiered step tunneling in triple-layer combinations of Cr/Cr_2O_3-Al_2O_3-HfO_2/Cr showed high asymmetry and nonlinearity [54].

Also, a comparison of quad-insulator Cr/TiO_2-Al_2O_3-TiO_2-Al_2O_3/Cr to double-insulator Cr/TiO_2-Al_2O_3/Cr showed nearly 30-fold enhancement with the four alternating layers [67]. These studies show that there is a high level of interest in developing MIIM devices, which possess great capability as a high frequency rectifier for rectenna devices.

2.3.3 Challenges Implementing MIM Diodes to Rectenna

Despite the work being performed to improve MIM and MIIM for rectenna, challenges still remain related to the fabrication and implementation to high frequency applications:

- *Insulator fabrication*. The insulator fabrication method needs to guarantee a uniform, thin, and defect free layer. Two common methods for forming a nanometer thin insulator include native oxide formation (e.g. thermal oxidation, gas phase oxidation, vapor deposition) and atomic layer deposition (ALD).

- *Insulator defects*. Pinholes in the oxide will introduce an additional electron conduction component in parallel to tunneling. This contribution can be orders of magnitude higher than the tunneling current. Pinhole formation is usually due to the oxide formation process. But high applied currents during operation can cause Joule heating that induces thermally enhanced electromigration which forms pinholes. Second, *I–V* characteristics may depend on the density of trap states. Electron tunneling can take place through traps, which can increase current. However, this can also hinder the response time of the diode.

- *Figures of merit*. As mentioned, there is a challenge inherent to balancing the trade-offs between various diode FOMs along with the RC time constant. Low resistance, needed to maximize impedance matching with the antenna, requires a small energy barrier to enhance tunneling conduction. However, diode capacitance favors a thick dielectric.

- *Diode area*. If dielectric thickness is constrained, low capacitance can also be achieved by reducing the area of the diode. Although this leads to fabrication challenges.

2.3.4 *Traveling Wave Diodes*

Another solution to overcome the RC limitations is the traveling-wave diode. Instead of locating the diode element at the antenna feed-point, a traveling-wave diode uses a MIM transmission line structure. The antenna creates a surface plasmon wave that propagates down the transmission line. As the wave travels, the MIM gradually rectifies the signal. In this configuration, the RC time constant is based on the impedance of the line instead of the inherently capacitive lumped-element metal–insulator–metal tunneling diode. Traveling-wave diode structures have been demonstrated for 10.6 µm and 1.6 µm. The limitations of this structure arise from propagation loss reducing coupling efficiency.

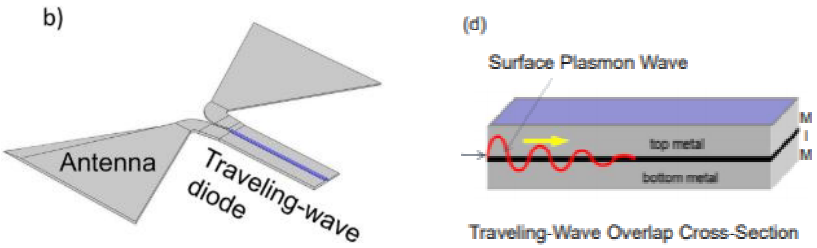

Figure 2.7. Traveling-wave diode operating as traveling surface plasmon wave from the antenna is gradually rectified across the metal–insulator–metal transmission line. Adapted with permission from [68].

2.3.5 *Geometric Diodes*

Geometric diodes leverage asymmetric structure for their rectification mechanism instead of asymmetric material properties. One method of exploiting geometric enhancement is to pattern a thin film conductor into an inverted arrowhead (Figure 2.8). The asymmetric structure preferentially funnels electrons by spatially restricting flow in one direction and encouraging conduction in the other, thereby realizing asymmetric charge transport expected for a diode. These structures satisfy the low RC time constant needed for optical rectification: the planar structure gives low capacitance, while the conducting metal film ensures low resistance.

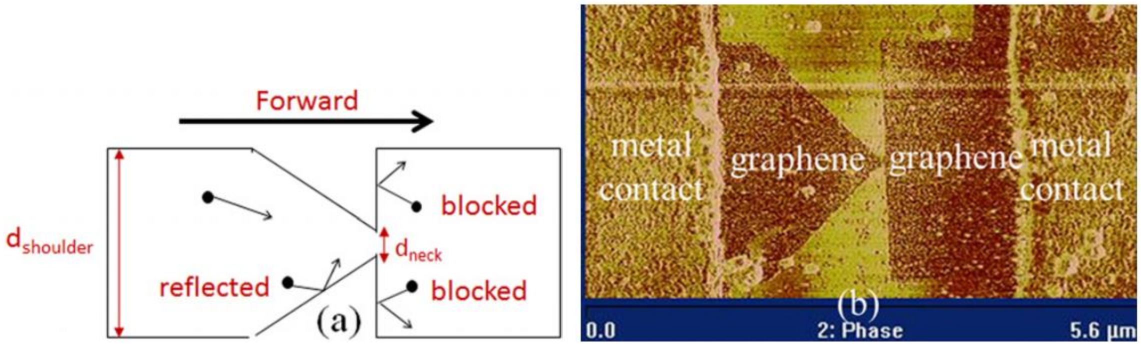

Figure 2.8. (left) Schematic of a geometric diode and (right) graphene geometric diode. Adapted with permission from [23].

For geometric diodes to operate, the constricting neck must be close to the mean-free-path length of charge carriers in the film. Moddel has reported a geometric diode using patterned graphene [23, 69]. Graphene is an ideal material for geometric diodes and make for promising optical rectennas due to their conductivity. The graphene can also be patterned into bowtie antenna designs to facilitate the absorption of THz radiation [23, 25, 70]. Still, the asymmetry of geometric diodes at present is not enough for practical solar rectification.

2.3.6 Carbon Nanotube Diodes

There are several opportunities to incorporate CNTs in diode. The great conductivity of metallic CNTs makes them a good electrode material. Doping semiconducting CNTs can enable p–n junctions for various diode applications. For instance, a room temperature THz detector was realized by making p–n junctions between horizontally aligned, doped CNTs [71]. This type of structure cannot work as an optical frequency detector however, due to the limited response time of charge the carriers.

The high aspect ratio of CNTs can also provide them with an enormous field enhancement factor due to the asymmetric structural effect [39]. This has been demonstrated in various manners, such as in a field emitter configuration. Meanwhile, Shin *et al*. fabricated a metal–insulator–CNT diode at the base of a single vertically oriented multiwall CNT. The field enhancement was above 10^4 and produced current densities that were drastically improved compared to non-field enhanced MIM. This design has potential for optical rectification because in addition to the high CNT aspect ratio providing an electrical field enhancement, the minute CNT tip achieves ultralow junction capacitance.

The capability of CNTs to be fabricated in aligned arrays is another important factor that offers the prospect for creating dense networks of CNT-based diodes. The density, however, plays a crucial role. It has been shown that densely packed CNT arrays encounter a screening/shielding effect that effectively reduces the geometric field enhancement of high aspect ratio CNTs (Figure 2.9)

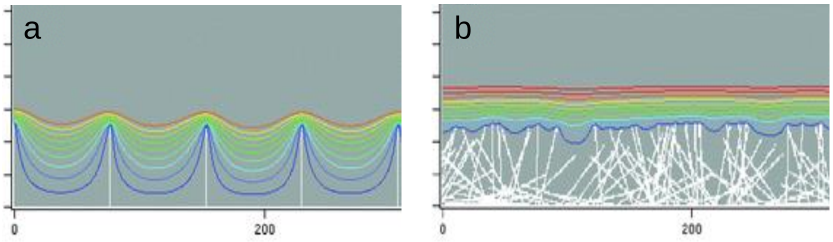

Figure 2.9. Equipotential lines of (a) aligned CNTs exhibiting electric field enhancement and (b) dense CNTs where screening occurs. Adapted with permission from [72].

2.4 Rectenna Semiclassical Theory

An optical rectenna is described by semiclassical principles, wherein the incident electromagnetic radiation is treated classically as a sinusoidally propagating wave that is coupled through the antenna, while the electronic behavior of the diode is treated under quantum mechanics. At optical frequencies the photon energy is high enough in relation to the input power that photons are quantized and thus the quantum nature of the electromagnetic field must be accounted for with respect to the diode interaction. The incident optical field, treated as a classical time dependent perturbation, interacts with electrons in the antenna that propagate as plasmons to the diode. This semiclassical approach in the diode is accounted for using the theory of photon-assisted tunneling (PAT).

When the incident field is strong and the energy of single photon is small, the approach resembles a continuum and semiclassical theory converges on classical rectenna operation.

2.4.1 Photon-Assisted Tunneling Theory

This section details the approach developed by Tien and Gordon for deriving the illumination current of a rectenna via photon-assisted electron transport [73]. Incident radiation captured by an adjacent antenna source creates an oscillating voltage in addition to the d.c. bias across a diode: $\tilde{v}_D = V + V_\omega \cos{(\omega t)}$. MIM diode current is treated as the quantum tunneling of individual electrons through a thin potential barrier. We then consider the oscillation, $V_\omega \cos{(\omega t)}$, as a perturbation in the electron's original Hamiltonian, H_0. Based on the perturbed state, $H_L = H_0 + eV_\omega cos(\omega t)$, the perturbed electronic wavefunction has the form

$$\Psi_L(\vec{r}, t) = \psi(\vec{r}) e^{-\frac{iE_0 t}{\hbar}} \left(\sum C_n e^{-in\omega t} \right), \tag{2.22}$$

which satisfies the time-dependent Schrödinger equation with coefficients $C_n = J_n\left(\frac{eV_\omega}{\hbar\omega}\right)$. J_n is the Bessel function of the first kind with argument $\frac{eV_\omega}{\hbar\omega}$. Equation (2.22) then becomes

$$\Psi_L(\vec{r}, t) = \psi(\vec{r}) \sum_{n=-\infty}^{\infty} J_n\left(\frac{eV_\omega}{\hbar\omega}\right) e^{-\frac{i(E_0 + n\hbar\omega)t}{\hbar}} . \tag{2.23}$$

This equation makes it clear that the effect of the incident light is to shift the electron energy by $n\hbar\omega$, occurring with probability $J_n(eV_\omega/\hbar\omega)$. n signifies the number of photons absorbed or emitted by the electron in a multi-photon process [74]. The total wavefunction is the weighted sum of all possible photon-assisted states. The nature of the Bessel function is such that the probability of an electron experiencing emission or absorption from multiple photons decreases rapidly with n. To clarify the physical impact of the photon absorption on the original wavefunction we seek to describe the result in terms of electron current density. Recombining terms into the unperturbed wavefunction, Ψ_0, and realizing that the modulated energy terms $E_0 + n\hbar\omega$ can be inserted into the argument of the original wavefunction, $\Psi_0(E_n = E_0 + n\hbar\omega)$, the total wavefunction that describes the effect of illumination becomes

$$\Psi_L = \sum_{n=-\infty}^{\infty} J_n\left(\frac{eV_\omega}{\hbar\omega}\right)\Psi_0(E_0 + n\hbar\omega)\,. \tag{2.24}$$

The net illuminated current in this system is calculated from Ψ_L through [75]

$$I_L = \frac{-e\hbar \mathrm{A}}{2m_e}\left[\Psi_L^* \nabla \Psi_L \; - \Psi_L \nabla \Psi_L^*\right]. \tag{2.25}$$

A is the junction area, m_e is the electron effective mass, and Ψ_L^* is the complex conjugate of the wavefunction. Inserting the wavefunction from equation (2.24) into equation (2.25) gives

$$I_L = \sum_{n=-\infty}^{\infty} J_n^2\left(\frac{eV_\omega}{\hbar\omega}\right)\cdot\left\{\frac{-e\hbar \mathrm{A}}{2m_e}\left[\Psi_0^*(E_n)\nabla\Psi_0(E_n) - \Psi_0(E_n)\nabla\Psi_0^*(E_n)\right]\right\}. \tag{2.26}$$

It should be clear that the expression within the curly brackets is identical to the original unperturbed d.c. current, but shifted in energy according to n multiples of photon energy; I_L is the superposition of each photon energy-modulated d.c. current and weighed by the square of the probability amplitude (*i.e.* $J_n^2\left(\frac{eV_\omega}{\hbar\omega}\right)$). The unperturbed energy is simply the applied d.c. electrical potential $eV = E_o$. Similarly, if we express the photon energy as a voltage $V_{ph} = \hbar\omega/e$ then PAT theory finally gives $I_L(V)$ in terms of the dark diode current, $I_D(V)$, through

$$I_L(V) = \sum_{n=-\infty}^{\infty} J_n^2(\alpha)\, I_D\big(V + nV_{ph}\big)\,. \tag{2.27}$$

where $\alpha = \frac{eV_\omega}{\hbar\omega}$ characterizes the strength of the incident field V_ω in terms of the photon energy. For $\alpha < 1$ only the $n = (0, \pm 1)$ terms are significant, which implies that the photon-assisted electrons are primarily affected by single-photon emission and absorption. This is deemed the *quantum regime* of rectenna operation since the photons are quantized. Alternatively, for $\alpha \gg 1$, which occurs when the incident field is strong or the frequency is low, then each electron absorbs many photons and energy excitation approaches a continuum akin to classical operation. The importance of equation (2.27) is that it can be used to calculate the net rectified current for a device under monochromatic illumination using only the dark *I*–*V* curve of the diode. For theoretical investigations, the diode is usually assumed to be piecewise ideal, such that the dark *I–V* is modeled as a perfect linear resistor under positive bias with zero leakage current in reverse bias.

For a rectenna converting optical frequencies at low power, equation (2.27) can be approximated to the first order of terms since $J_n^2(\alpha \ll 1)$ drops off rapidly with n. In the quantum regime, the expression for PAT can be simplified by approximating the Bessel function to get

$$I_L(V) = \left(1 - \frac{\alpha^2}{4}\right) I_D(V) + \frac{\alpha^2}{4}\left(I_D\left(V + V_{ph}\right) + I_D\left(V - V_{ph}\right)\right). \tag{2.28}$$

It should be obvious that for an ideal diode with zero reverse current, this relation results in a shift of the $I_L(V)$ towards the second quadrant, producing a positive short-circuit current (I_{sc}) and negative open-circuit voltage (V_{oc}). These are the results of illuminated device behavior that characterize the optical rectification mechanism, and once again highlight the contrast between a rectenna and a PV solar cell.

Furthermore, this PAT theory can be expanded for multi-spectral and broadband illumination, as has been generalized by Tucker *et al.* [76–78]. This will be discussed in Chapter 7.

2.5 The Carbon Nanotube Optical Rectenna

The CNT optical rectenna demonstrated by Sharma *et al.* [8] marked a transition in rectenna studies—it gave encouragement that scalable approaches to realizing an efficient solar rectenna were possible. They developed vertically aligned forests of multiwall CNTs and fabricated MIM diodes at the tip of each CNT. In the resulting structure (Figure 2.10), the CNTs serve as both highly absorbing nanoantennas as well as the lower metal electrode for the tunneling diode. The advantage of having each CNT serve as both the nanoantenna and part of the diode lies in minimizing power transmission loss between the components.

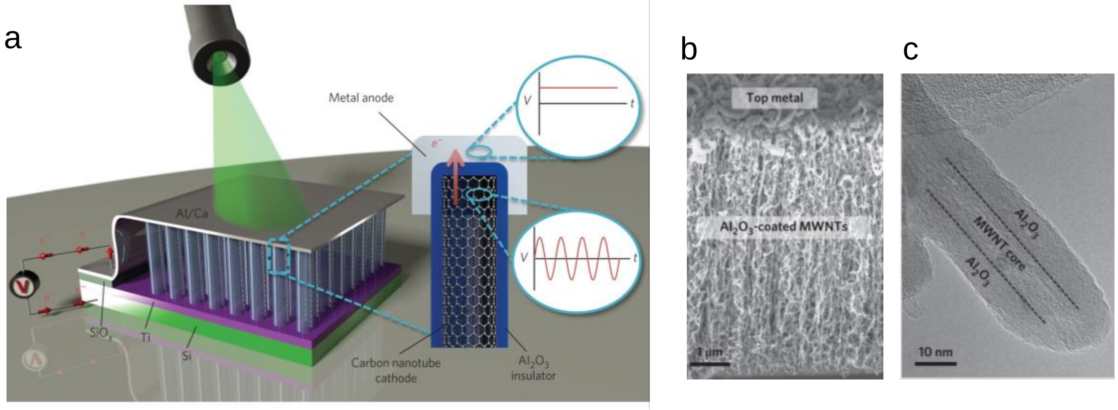

Figure 2.10. (a) Schematic of the CNT optical rectenna with (b) SEM images of the CNT array and (c) TEM images of the oxide-coated CNT tip. Adapted with permission from [8].

The diode was formed by depositing a thin dielectric insulator and metal electrode over the CNTs tips. The insulator was 8 nm Al_2O_3 deposited using atomic layer deposition (ALD); this process allowed for growth of defect-free, conformal, and reliable dielectric coatings. To finish the diode, a low work function (2.9 eV) Ca electrode was deposited to on top to give the diode its asymmetry versus the 5 eV work function of the CNT (Figure 2.11). This multiwall CNT tunneling diode structure was crucial for realizing an optical rectenna. The CNT diameter was ~8 nm, so the accompanying diode fabricated at each tip has the ultralow capacitance (1.7 aF) producing a cutoff frequency ~800 THz that was necessary for optical power conversion. These large-area vertical arrays of CIM diodes were promising compared with other rectifying MIM devices that require expensive, complicated, and challenging fabrication techniques over limited areas.

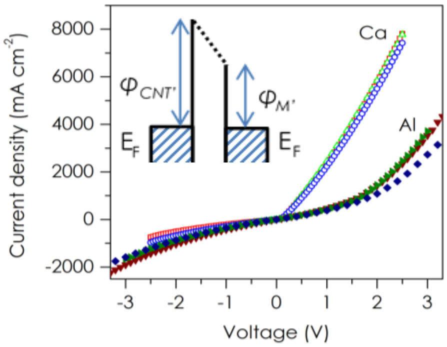

Figure 2.11. *I–V* scans showing asymmetric diode behavior for low work function Ca electrode (ΔΦ~2.1 eV) versus Al (ΔΦ~0.7 eV). Inset depicts the potential barrier. Adapted with permission from [8].

2.5.1 *Optical Rectification*

Figure 2.12 shows the optical rectification photoresponse. For 532 nm illumination the intensity was 26 mW cm^{-2}. In relation to the dark *I–V* curves, the response exhibited a shift into the second quadrant (*i.e.* $-V_{oc}$ and $+I_{sc}$) for power generation as well as an increase in the forward bias current. These characteristics indicate optical rectification and not a photovoltaic response. The photoresponse of this CNT rectenna device was at least six order of magnitude higher than previous optical rectification studies. Further, the intensities used here were around 10,000 times lower than a previous study of optical rectification by Ward *et al*. [20].

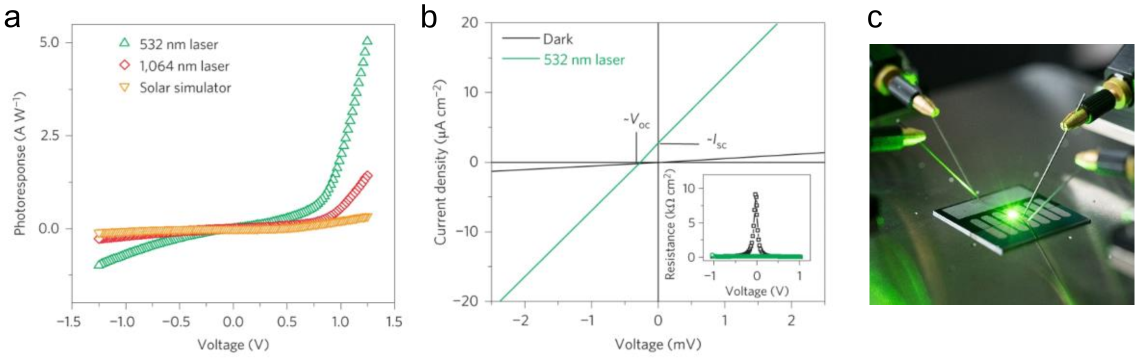

Figure 2.12. Optical rectification response and device under test. Adapted with permission from [8].

In Figure 2.13(a) the observed polarization dependence is more evidence of rectification. Such polarization sensitivity is consistent with classical antenna behavior and alludes to the role of the CNT as an antenna component, corroborated by nanoantenna studies on aligned CNT arrays [30, 34].

s

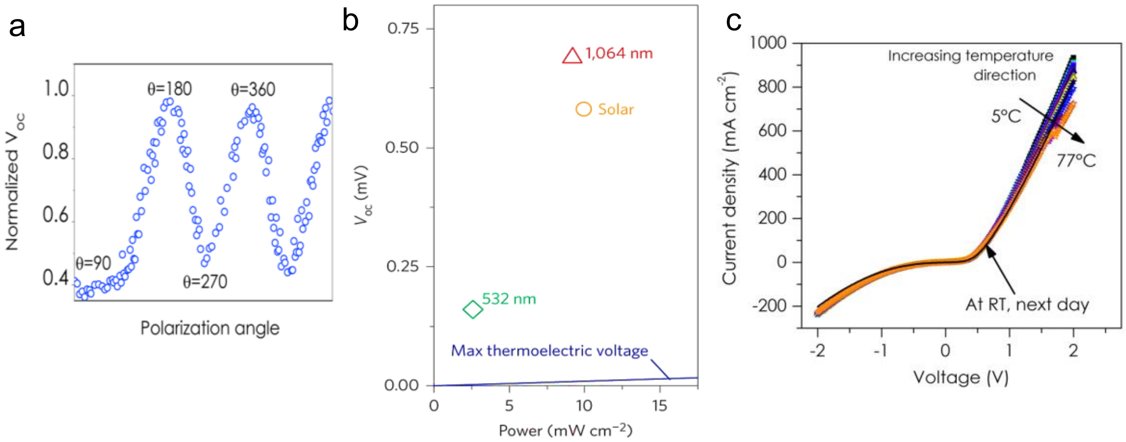

Figure 2.13. (a) Polarization dependence. (b) V_{oc} measured under 532 nm, 1064 nm, and 1.5 AM solar illumination. (c) Temperature independent diode *I*–*V* scans. Adapted with permission from [8].

The spectral dependent response is summarized in Figure 2.13(b). The conversion efficiency of 532 nm was 3×10^{-7} % with a peak efficiency of 10^{-6} % occurring at 1064 nm[*]. It is interesting that the response to broadband solar illumination was so much lower than the response to monochromatic wavelengths—particularly the short-circuit current which was 10 times smaller than that of monochromatic light of similar intensity. This was speculated as due to frequency mixing under broadband illumination. This question is still of interest and discussed in this dissertation in light of photon-assisted tunneling. The devices did not show detectable change in *I*–*V* during up to 77 °C due to the dominant tunneling mechanism that is largely temperature-independent. This temperature independence is another advantage of optical rectennas versus PVs.

---

[*] These values represent the external conversion efficiency. The original publication factored in power loss from the 10 % Ca electrode transmissivity.

Sharma *et al.* attributed the low observed rectenna conversion efficiency to considerably large junction resistance: for an array density of 10^{10} CNT/cm^2, resistance comes out to ~1TΩ per junction. This leads to considerable impedance mismatch against the antenna that is expected to be on the order of 100 Ω.

2.5.2 Issues and Challenges Remaining

The following is an overview of the limitations and outstanding challenges that remain after the CNT optical rectenna was introduced. These factors are designed to put in perspective the issues that will be addressed within this dissertation.

- *Impedance mismatch*. Because of the extraordinary resistance of the CNT diode junction, impedance matching is expected to make up the largest portion of the efficiency loss. The challenge of lowering resistance is necessary to maximize power transfer from the antenna to the diode. For the MIM diode, a considerable part of the device resistance emerges from the tunneling resistance. One route to improving the antenna-diode impedance match is to reduce the thickness of the potential barrier, which exponentially affects tunneling resistance. This approach is limited by the fabrication ability to precisely and conformally coating thin oxide films on CNTs. There also remains potential to improve the electrical conductivity of the electrodes to reduce diode resistance.

- *Electrode transparency*. There is room for improving the transmission of light through the top electrode for absorption by the CNTs, as the use of Ca was estimated to pass only 10 % of this incident power. Thus, increasing transmission into the CNT array should have a straightforward effect on conversion efficiency. Electrode transparency can be increased by using a thinner metal layer. However, as mentioned above, this must also be balanced with the metal's electrical conductivity, which diminishes with reduced film thickness. Still, there are a variety of materials available that could be advantageous for a conductive and transparent top electrode, including some more novel materials such as ITO, PEDOT:PSS, or Ag nanowires. Moreover, different applications of the rectenna, such as for IR detection, may require different spectral properties for the top electrode.

- *Unstable materials*. The use of Ca electrodes rendered these devices inoperable in air because of the tendency of Ca to oxidize immediately. This is especially problematic from the perspective of the diode because most low work function metals that would otherwise be ideal for producing highly asymmetric and nonlinear tunneling are susceptible to oxidation. The challenge with the top electrode then lies in finding a material that has practical air stability while balancing the work function, conductivity, and optical transparency required for light transmission and conversion.

- *Understanding of the antenna*. There is still much in the way of the nanoantenna behavior that is unknown in these rectenna devices. The observed polarization dependence supports the notion of the CNTs acting similarly to classical antennas. However, other typical antenna effects still remain untested—the most prominent of which is as the effect of CNT antenna length on radiative properties. There is opinion that the dense CNT forest encourages optical coupling between neighbouring CNTs which enhances absorption and overall power conversion. Finally, the antenna radiation efficiency is also unknown. That, along with the guessed at value for antenna radiation resistance, makes progressing our understanding of the CNT antenna operation important for establishing an efficient optical voltage.

- *Understanding of the rectification mechanism*. Optical rectification experiments provided evidence supporting photon-assisted tunneling in the rectenna conversion process. These demonstrated results were primarily in qualitative agreement with photon-assisted transport (e.g. second-quadrant power generation). A more thorough employment of the rectenna theory to model the CNT rectification process is needed to elucidate the contributions of the antenna as well as more robustly characterize the role of the diode on efficiency limitations. For further improvements to be made it is essential to study the various efficiency losses in detail, including optical transmission losses, losses in the antenna, and shortcomings in the diode. These details are necessary to prioritize improvements in the rectenna elements and better guide material requirements. Also, the demonstration of solar rectification showed weak performance relative to monochromatic light conversion. Theory of broadband rectification is needed to explain this limitation. Ultimately, a robust model of the CNT rectenna behavior would be invaluable for pinpointing the limits that can be practically achieved in the rectenna.

These issues are addressed in this dissertation with the aim of bringing this CNT rectenna structure to practical application. First, characterization of the diode tunneling barrier will be presented in an effort to reduce tunneling resistance by coordinating the choice of dielectric and thickness. And tradeoffs will be explored with respect to other nonlinear diode properties as well as fabrication limits that affect device yield. Second, multi-insulator tunneling diodes are exploited to bypass the need for low work function electrode metals that are chemically unstable. This improvement allows CNT rectennas to be fabricated with Al or Ag in place of Ca. Furthermore, this multi-insulator approach gives more freedom to manipulate the diode properties such that asymmetry can be enhanced without the resounding impacts on resistance. These contributions lead to improved performance and understanding of the CNT tunneling diode structure. Optical rectification is tested in air for the improved devices and analyzed with a model of rectenna photon-assisted tunneling theory to gain valuable insight into both the role of the CNT as a dipole antenna as well as individual mechanisms contributing to efficiency loss. Finally, in an effort refine the performance, this dissertation will explore innovative materials and device structure redesigns. This includes investigating transparent and conductive polymer materials alongside polymer encapsulation that promises more robust, low-cost, and large-scale manufacturing that leans to commercializing this technology.

CHAPTER 3. STUDY OF CNT–INSULATOR–METAL TUNNELING DIODES

Since the first report of the CNT optical rectenna, the diode component has been the primary focus due to the limitations in efficiency that are supposed to arise from inadequacies in the CNT–insulator–metal (CIM) diode performance. In this chapter, the important advancements in the CIM diode are presented by investigating the impact of the tunneling barrier geometry on diode characteristics. The impact of barrier height and width are explored by controlling the insulator thickness and dielectric affinity, respectively. Various dielectrics have been examined as the oxide barrier, including Al_2O_3, HfO_2, TiO_2, ZrO_2, and ZnO.

3.1 Methods

Diodes comprised vertically oriented multiwall CNT forests with insulator and metal layers coating the top of the array (Figure 3.1). Al or Ag metals were studied as air-stable top electrodes. Varying thickness of Al_2O_3 was examined, as well as the choice of various dielectric oxides in order to control the dielectric affinity. CNT tip opening was implemented to increase electrical connections to the inner multiwall and the effect on diode properties was assessed.

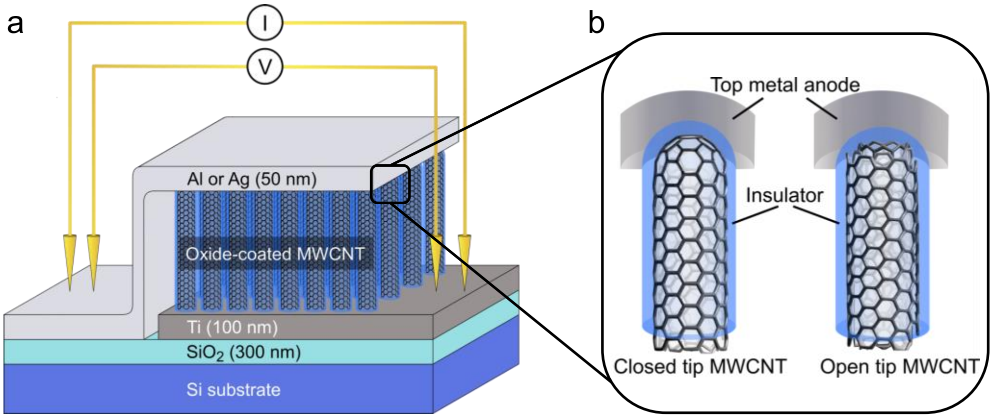

Figure 3.1. (a) Schematic of CNT–insulator–metal device structure. (b) Illustration of the diode junction formed at the top of the nanotube, with either closed or open CNT tip.

3.1.1 *Device Fabrication*

The following is an overview of the process steps, depicted in Figure 3.2: (1) catalyst deposition, (2) CNT growth, (3) conformal oxide deposition, (4) top electrode device patterning.

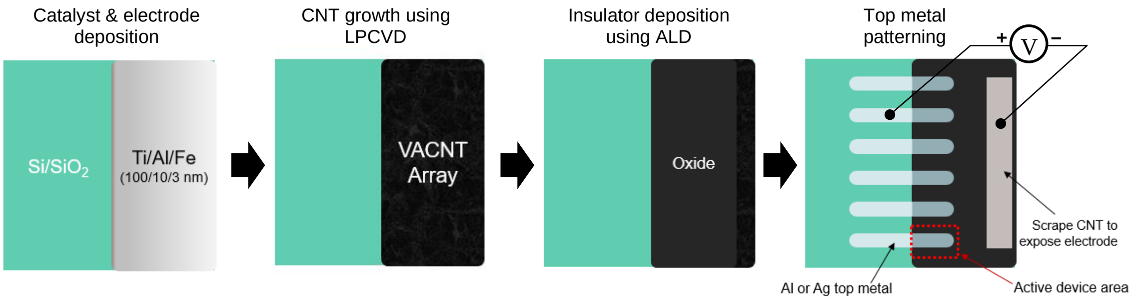

Figure 3.2. Process flow for CNT diode fabrication.

<u>CNT Growth</u>

CNTs were grown on high resistivity Si substrates that are coated in a 300 nm thick layer of thermally grown SiO_2. The SiO_2 provides the devices electrical isolation from the substrate and creates a zone for probing away from the active device area. Catalyst was deposited on the substrate using a Denton Explorer e-beam ($<2\times10^{-6}$ torr). The catalyst was Ti/Al/Fe (100/10/3 nm) and deposited at rates of 1.5, 0.5, and 0.1 Å/s, respectively. The Ti/Al forms a bottom electrode that will electrically connect all the CNTs after growth and provide a conductive surface for *I*–*V* measurements. Specifically, the role of the Ti layer is to provide good adhesion to the substrate to prevent CNT delamination. Fe is the catalyst, with Al assisting as a buffer layer.

Vertically aligned CNTs were grown from the catalyst using LPCVD at 850 °C and 1 kPa with C_2H_2 carbon source gas (Aixtron Black Magic$^{©}$). Growth times between 150–180 s produce multiwall CNTs with a forest height around 10–30 µm, diameter ~10 nm, and an average of 6 walls.

CNT Tip Etching

In some cases, the CNTs tips were etched with O_2 plasma prior to diode fabrication. This idea, initially explored by Shah *et al*., was to characterize the impact of removing the outer hemispherical caps so as to unhide the inner multiwalls. The additional points of electrical contact have been seen to reduce the CNT electrical resistance [79]. The CNT caps were removed by reactive ion etching (RIE, Unaxis) with 30 s exposure to 80 W O_2 plasma. This RIE process was used throughout Chapter 3 and then when otherwise noted.

Oxide Deposition:

The quality of the insulator layer is critical to MIM diode performance. ALD was used to form the dielectric layer as it is the most precise method of forming reliable conformal coatings. Oxide layers with thickness between 2 and 8 nm were deposited on the CNT array by ALD at 250 °C. Prior to the deposition cycles, 300 s of O_2 plasma was incorporated to oxidize the surface of the CNTs and introduce hydrophilic moieties (–OH and –COOH), to promote uniform nucleation of the oxide and conformal deposition.

During deposition of Al_2O_3, trimethylaluminum (TMA) and water (H_2O) vapors were used with 30 s purge times between cycles to allow vapors to diffuse completely into the array and coat the CNT lengths. Other dielectric materials were deposited using identical ALD processes at 250 °C with 30 s purge times. In place of TMA, the precursor used for each alternative material was tetrakis (dimethylamido) hafnium(IV) for HfO_2, tetrakis (dimethylamido) titanium(IV) for TiO_2, tetrakis (dimethylamido) zirconium(IV) for ZrO_2, and diethyl zinc for ZnO. Deposition rates were calibrated by depositing the oxides on a Si wafer and measuring thickness using ellipsometry (Woollam M2000).

Top Electrode Metal Deposition:

To complete the device structure, 50 nm top electrode metal was deposited (Figure 3.3). Since this work is focused on investigating air-stable materials, Ag or Al electrodes (Lesker or Sigma Aldrich) are deposited by thermal evaporation (~10^{-7} torr) at 1 Å/s with a shadow mask. Thermal evaporation was used to minimize penetration of atoms from the top metal into the dielectric layer during deposition. The 50 nm thickness is based on the thickness of metal that would be deposited on a planar structure. The active area of each device defined by the shadow mask was 7.6 mm^2. Experiments performed in this chapter involved fabricating 2–5 batches of samples for a given experimental condition and typically at least 5 devices were measured from each sample to gather for statistics.

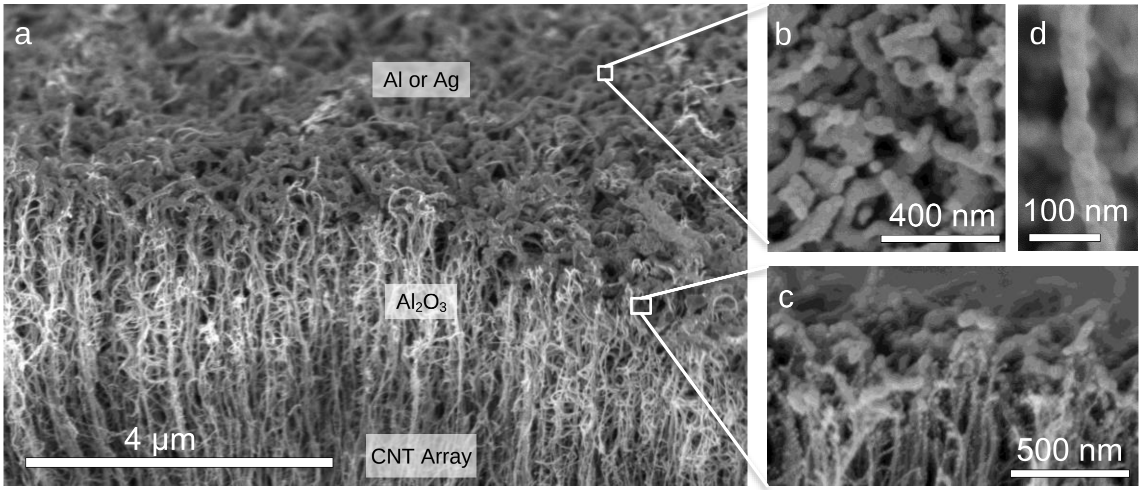

Figure 3.3. (a) SEM image of full CNT/Al$_2$O$_3$/metal device. (b) Top view and (c) side view images of 50 nm Ag deposited at the top of the array. (d) Close up of Ag-coated CNT.

3.1.2 Characterization

I–V characteristics were measured using a Keithley 2450 d.c. source meter connected to an electrical probe station (Cascade MicroTech). All measurements were performed in air at room temperature. Diode parameters ($R(V)$, $\mathcal{A}(V)$, $\mathcal{N}(V)$, $\beta(V)$) were calculated from fitting *I–V* curves to a high order polynomial†. Scanning electron microscopy (SEM) images were collected using a Hitachi SU8230 at 1–5 kV acceleration voltage. Scanning transmission electron microscopy (STEM) images were obtained from an aberration-corrected Hitachi HD-2700 operated at 200 kV and equipped with energy dispersive X-ray spectroscopy (EDS) for elemental mapping. For STEM imaging, oxide-coated CNTs were scraped off of the device substrate using plastic tweezers and deposited

---

† Throughout this dissertation the current, I, will not be symbolically distinguished from current density (usually J). Instead, variables expressing current and current density will be made apparent from the specified units (A or A/cm^2, respectively) based on nominal diode area. Similarly, device resistance $R(V)$ may be expressed using areal units (Ω cm^2) when appropriate to normalize between devices.

on a Cu or Ni TEM grid coated with a carbon mesh. Metal work functions were verified using a Kelvin probe in air (Table A.1).

3.2 Effect of Insulator Thickness

Diode resistance is currently one of the greatest hindrances to CNT rectenna efficiency. The CIM diode reported by Sharma *et al.* had resistance calculated on the order of 1 TΩ per CNT diode junction, with an overall device resistance achieving 7.5 kΩ cm^2 due to the cumulative array density of ~10^{10} CNT per cm^2. Shah *et al.* reduced diode resistance to 100 Ω cm^2 by investigating several top metal materials and thicknesses, lower insulator thicknesses, and by opening the CNT tips for additional multiwall-insulator conduction channels [79]. This work explores insulator thickness down to 2 nm to assess the feasibility of fabrication and consequent electrical tradeoffs of thinning the insulator.

In this CIM structure, either Al or Ag was used as the top electrode to form air-stable devices. Ag and Al both possess similar work functions (Φ~4.3 eV, see Table A.1), so they can be interchanged later according to the need for either the conductivity and oxidation resistance of Ag or the higher optical transmissivity of Al. The minimal work function difference (ΔΦ~0.3 eV) established between multiwall CNTs and Al or Ag is expected to produce minor diode asymmetry.

In Figure 3.4(a), a clear exponential relationship is found between resistance and insulator thickness, consistent with MIM tunneling theory [45, 63, 80]. It is interesting to note that the logarithmic change in resistance with thickness is less pronounced than ordinary MIM diodes. Since these CNT devices are a parallel network of billions of diode junctions over a large area, we expect that some shorting of individual junctions is leading to a dilution of the cumulative diode tunneling behavior. Even though minimizing resistance is crucial for efficient diode coupling with the antenna component of the rectenna, this manner of thinning the Al_2O_3 layer to lower resistance affects other necessary diode parameters. For instance, lessening the insulator lowers diode asymmetry (Figure 3.4(b)), as the thinner insulator causes direct tunneling to dominate instead of the more asymmetric Fowler-Nordheim tunneling (FNT) behavior.

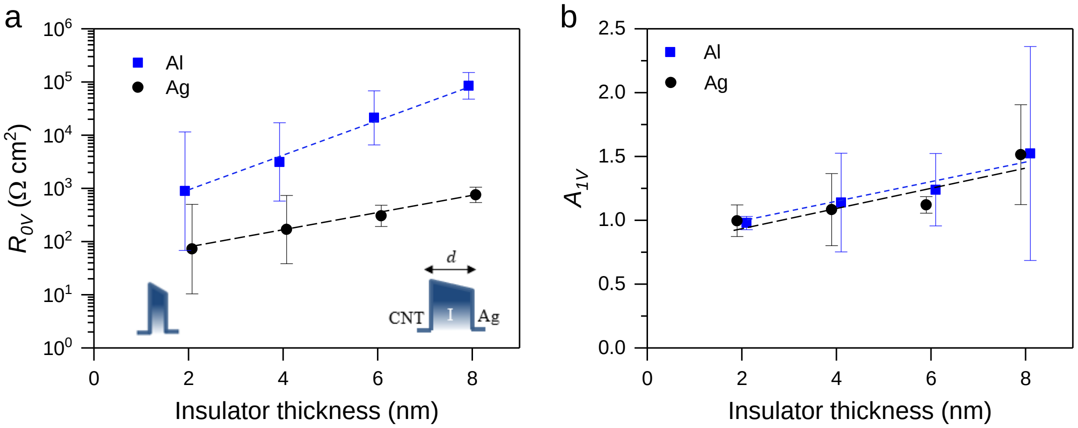

Figure 3.4. Plots of (a) zero-bias resistance, R_{0V}, and (b) asymmetry at 1 V, A_{1V}, as a function of Al_2O_3 insulator thickness. Data markers with error bars represent the geometric mean and geometric standard deviation of around 5–15 devices. Note that resistance is expressed in terms of the current density, and so is normalized to device active area.

Furthermore, for Al_2O_3 <4 nm there is a drastic increase in device-to-device variation as well as significantly more frequent occurrence of short-circuited devices. These variations are attributed to our limited ability to reliably fabricate uniform and pin-hole free oxide layers onto vertical CNT arrays using ALD. This is further investigated by assessing the conformal oxide coating. In Figure 3.5(a) the cross section STEM image of an insulator- and metal-coated CNT forest reveals that an 8 nm Al_2O_3 coating only penetrates about 5 µm into the array, despite the 30 s extended ALD purge times. Though Figure 3.5(b) verifies that the conformal deposition of Al_2O_3 is continuous across the entirety of the coated portion of the CNT length. The image reveals the oxide-coated CNT diameter is ~25 nm. Assuming the multiwall CNT diameter is approximately 8 nm based on prior TEM images [8], the image confirms that the Al_2O_3 coating is ~8 nm thick. After taking diameter measures from multiple CNTs across the device, we confirm that the Al_2O_3 coating is consistent throughout the array with a thickness variation of 1–2 nm between CNTs. Importantly, this insulator thickness variation has an exponential effect on the measured diode current density. If the Al_2O_3 thickness is deposited at ~2 nm, the natural deposition variation that we have observed may translate to a significant shorted CNTs across the device array. Resistance measurements for 2 nm presented in Figure 3.4 support this. In summary, this investigation has determined that the existing ALD process for the oxide layer has a lower limit of 2 nm.

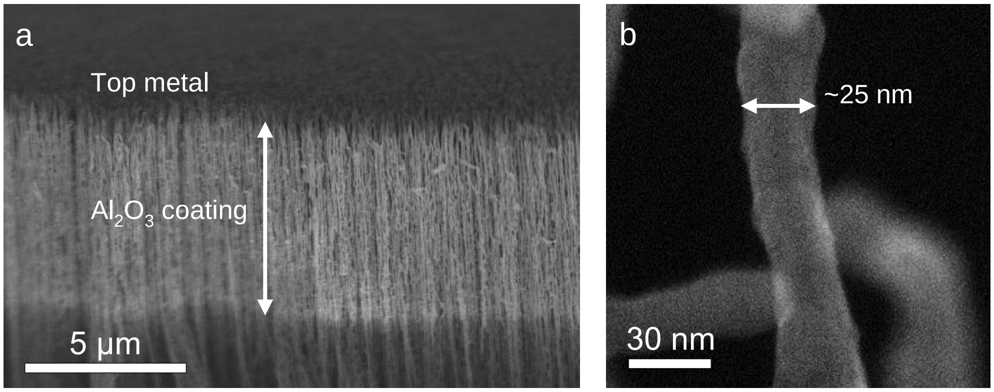

Figure 3.5. STEM images verify the presence of 8 nm Al_2O_3 deposited on the CNT forest. (a) Al_2O_3 conforms to the upper ~5 µm of the forest. (b) STEM images confirm the Al_2O_3 coating is ~8 nm.

3.2.1 Comparison of Al and Ag Electrodes

Lastly, we observe that Al electrodes produce CIM diodes with resistance that is two orders of magnitude higher than Ag (~3000 Ω cm^2 for Al and ~200 Ω cm^2 for Ag with 4 nm Al_2O_3). The resistivity of 50 nm planar Al (23×10^{-8} Ω m) is higher than Ag (3×10^{-8} Ω m). However, the sheet resistance of these metals is too low (< 10 Ω sq) in comparison to tunneling resistance to fully explain this discrepancy [79]. We surmise that Ag could be either diffusing or penetrating into the Al_2O_3 layer during deposition, despite our efforts to minimize penetration using low energy thermal evaporation of top electrodes. The possibility of penetration is detrimental to the fabrication of devices with very thin oxide layers. A possible route to ensure minimal penetration would be to lower the sample temperature during evaporation.

3.3 Effect of Insulator Electron Affinity

Since χ controls the height of the MIM tunneling barrier, the choice of dielectric material strongly affects the final diode characteristics. Ideally, χ should be close to one of the electrode work functions such that a shallow barrier near the metal-insulator interface minimizes turn-on voltage and maximizes asymmetry. Simulations of the effect of insulator electron affinity on MIM diode properties showed strong sensitivity to the barrier height [81]. Even minor changes in χ would alter R by orders of magnitude. In this study, CNT diodes were examined as a function of the insulator material and its electron affinity. Samples were tested using various oxides to with dielectric affinity values between 1.7 eV (Al_2O_3) and 4.3 eV (ZnO) (see Table A.2).

Zero-bias resistance was found to vary exponentially with χ (Figure 3.6(a)). As χ increases, the resulting shallower barrier experiences increased electron tunneling probability. As observed with insulator thickness, the magnitude change in resistance from χ is weaker than expected for a planar MIM device. Again, this is likely the due to defects and variability in in the single CIM junctions accumulating throughout the array.

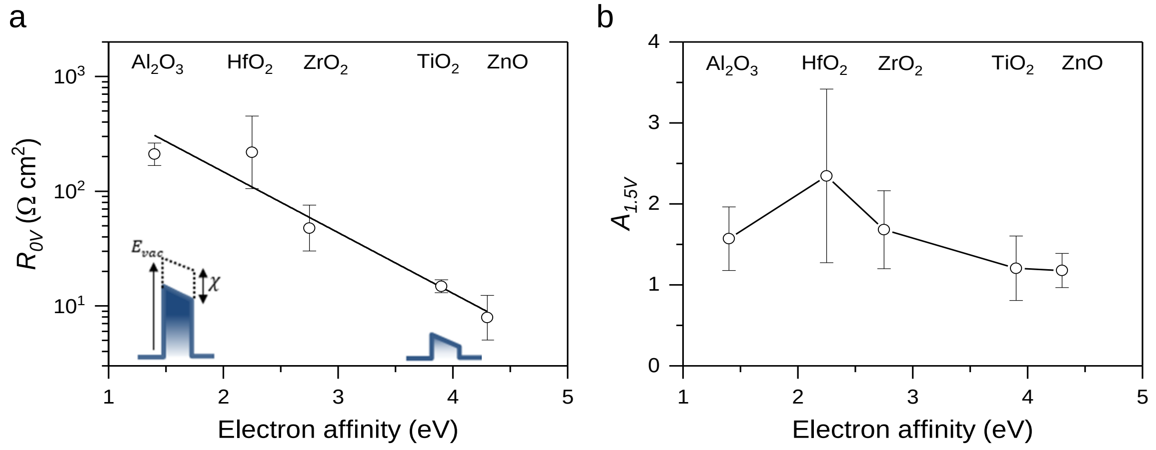

Figure 3.6. Plots of (a) zero-bias resistance, R_{0V}, and (b) asymmetry at 1.5 V, $A_{1.5V}$, as a function of electron affinity for 6 nm of Al_2O_3, HfO_2, ZrO_2, TiO_2, or ZnO. Electron affinity values (Table A.2) are taken from literature under similar fabrication conditions.

There is also an effect of barrier height on asymmetry [81]. Using 1.5 V bias as a benchmark, asymmetry is found to increase slightly from $\mathcal{A}(1.5\ \mathrm{V}) = 1.5$ with Al_2O_3 (χ = 1.4 eV) to 2.3 with HfO_2 (χ = 2.25 eV) (Figure 3.6(b)). This reflects the transition from a trapezoidal barrier to more triangular, enabling further manifestation of asymmetric Fowler-Nordheim tunneling (FNT) [58]. Surprisingly, asymmetry then decreases as electron affinity is raised above $\chi \sim 2.25$ eV. This asymmetry reduction suggests that the dominant electron conduction mechanism transitions from tunneling to more symmetric bulk- and defect-limited conduction for large electron affinity [80, 82]. Bulk-limited mechanisms can arise from defect sites (traps) in the dielectric. Electrons can use these traps as intermediaries to assist tunneling (trap-assisted tunneling, TAT) or be thermally emitted from a trap to the conduction band (Poole-Frenkel emission, PFE). Since traps behave similarly under forward and reverse bias, these mechanisms result in low diode asymmetry.

The conduction mechanisms of various dielectrics have been discussed in detail in other reports, [55, 80, 82] and specific details regarding dominant mechanisms governing devices used in this work can be found in Appendix B.1. Briefly, Al_2O_3 was found to exhibit clear direct tunneling behavior with FNT beginning at 2.2 V. At low voltages, HfO_2 primarily demonstrates direct tunneling, but transitions to PFE and TAT behaviors at moderately large biases. The competing mechanisms around 1 V cause large device-to-device variations in HfO_2 from fabrication variability. With even higher χ, we see more evidence of bulk-limited conduction dominating at lower voltages, explaining the trend of decreasing asymmetry. Even though higher electron affinity lowers resistance, substituting insulator materials can adversely affect temperature-sensitive applications as thermal conduction mechanisms may no longer be negligible [55, 82, 83].

3.4 Multiwall CNT Tip Opening

Even though a thin tunneling barrier is ideal to minimize diode resistance, we are limited to how thin we can deposit Al_2O_3 due to fabrication challenges (increased pin-holes) as well as reduced asymmetry and higher capacitance. An additional technique to mitigate device resistance was studied by Shah *et al*., who demonstrated an etching process to remove the hemispherical graphitic CNT cap prior to diode fabrication [79]. Opening tips exposes the inner walls to enable more direct electrical contact at the multiwall CNT-insulator interface (Figure 3.1(b)). The CNT tip opening was investigated on metal-coated CNTs. They reported up to 45 % reduction in contact resistance for CNT-metal junctions. I have since progressed this investigation to study the effect of CNT tip removal on insulator thicknesses as low as 2 nm, additional Al and Ag top electrodes, as well as alternative oxide materials to explore the influence of dielectric affinity.

In Figure 3.7, STEM images confirm that etching removes the hemispherical MWCNT tips. We see that a subsequently deposited Al_2O_3 layer entirely coats the CNT tip after the cap is removed (Figure 3.7(c)). This provides important visual confirmation that the exposed inner wall are now readily available to make electrical connections.

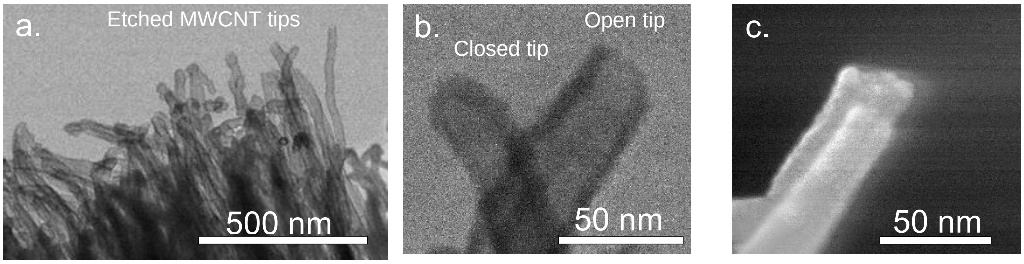

Figure 3.7. STEM images of the multiwall CNTs after tip etching and then coating in 8 nm Al_2O_3. (a) CNT forest showing some fraction of multiwall CNT tips remain closed despite etching. (b) Side-by-side comparison of a closed and open multiwall CNT tip. (c) Secondary electron STEM image shows the flat oxide coating atop the etched-open CNT which verifies that etching is responsible for the open tip and not mechanical breakage from handling during imaging preparation.

Electrical characterization of the etch-tip CNT diodes show that resistance can be lowered up to 75 % (Figure 3.8), consistent with prior results [79]. This relative effect is also independent of the Al or Ag top metal, showing that it is affecting the baseline resistance of the metallic CNTs by introducing more electrical connections. However, the relative change in resistance greatly diminishes to barely <5 % when the insulator is increased to 8 nm. This is because the tunneling resistance for the thick Al_2O_3 layer dominates over the CNT contact resistance, and the effect of tip opening becomes negligible. This has strong implications moving forward. For devices that are fabricated with thick insulator layers, tip opening may not be worth the time and effort to realize a possibly insignificant reduction in resistance.

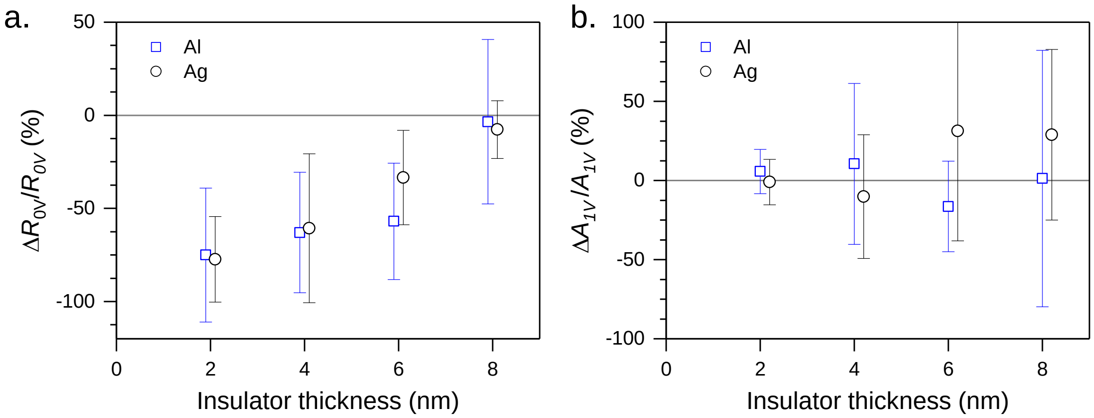

Figure 3.8. Effect of CNT tip opening on diode parameters. (a) Relative change in zero-bias resistance, R_{0V}, and (b) 1 V asymmetry, A_{1V}, after etching open tips, as a function of Al_2O_3 thickness with Al or Ag top electrode.

The effect of multiwall CNT tip opening is also compared for various oxides. There is a consistent reduction in resistance when opening the tips, generally independent of dielectric affinity (Figure 3.9). On average, 54 Ω cm^2 reduction was observed. This provides further evidence that the CNT–insulator contact resistance is isolated from the insulator tunneling resistance [79].

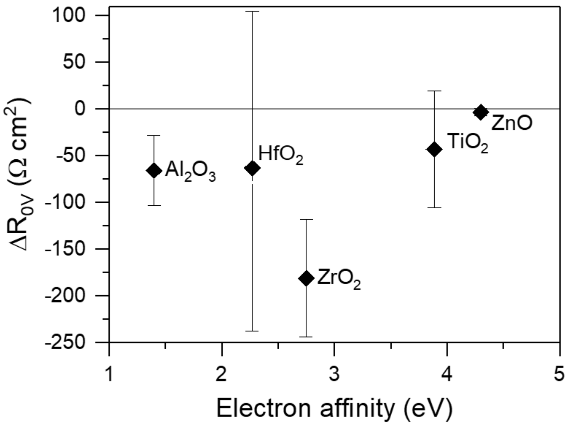

Figure 3.9. Change in zero-bias resistance, ΔR_{0V}, after CNT tip opening for 6 nm.

In summary, this section characterized the effect of CNT cap removal to enhance diode electrical conductivity. The process was shown to reduce resistance in most cases regardless of insulator material or thickness. However, the effect is negligible for thick insulators that have pronounced tunneling resistance. Also, this method of RIE cause unequal etching of the CNT array, which makes the forest height highly variable. We have generally seen that this variability introduced in the RIE step translates to more sample variability. Therefore, due to the adverse effect on device fabrication consistency, more complicated device structures presented in this work hereafter will forgo the use of RIE and CNT tip opening.

3.5 Summary

This chapter featured important incremental advances in our understanding of the CNT tunneling diode by studying the tunneling barrier geometry for Al and Ag top electrodes. The use of Al and Ag electrodes produces weak asymmetry due to the minimal work function difference between the metallic CNTs. Insulator thickness and potential barrier height both exponentially affect the diode resistance. These results bolster the notion that the CIM diode behavior is consistent with common planar MIM diodes. The magnitude of these effects is considerably weaker than an ideal MIM due to non-negligible series and shunt resistances that are present in the diode array from large-area fabrication variability and defects. Further, study of the effect of removing the closed hemispherical CNT tip revealed an improvement in CNT contact resistance that was consistent across various dielectric materials.

It was found that HfO_2 gives the best balance of asymmetry and resistance for the CIM diodes. However, this is somewhat offset by the large variability (both device-to-device and scan-to-scan) in CNT/HfO_2/metal devices. ZrO_2 is another reasonable choice that balances low resistance due to a shallow potential barrier with mild asymmetry and improved stability. In the next chapter, we will consider CIM diodes that utilize multi-insulator laminate tunneling structures. The use of HfO_2 or ZrO_2 will be leveraged in combination with Al_2O_3 due to their relatively shorter barrier and their tunneling-dominated conduction mechanisms.

These results have recently been externally corroborated. Berdiyorov and Hamoudi simulated single CNT–insulator–Ag structures using Green's function and density functional theory [84]. They investigated HfO_2 and ZnO insulators and showed similar values for asymmetry as was experimentally reported here, specifically that HfO_2 is the superior asymmetric dielectric ($\mathcal{A} \sim 2$). Moreover, their simulations verified that removing the hemispherical CNT tip reduces resistance, which they explain via suppressed electron back-scattering. Interestingly, they also explored chemical doping of CNTs as a suggested direction to enhance electronic transport properties. This is an exciting route for future experiments to pursue that will be mentioned in Chapter 10.

CHAPTER 4. MULTI-INSULATOR CNT TUNNELING DIODES

4.1 Motivation

The design of the CIM diode relies on competing requirements for asymmetric and low resistance electron tunneling. Specifically, balancing a thin but still asymmetric trapezoidal tunneling barrier is difficult and puts heavy demands on the diode materials [44, 85]. As illustrated in the previous chapter, metals that are chemically stable enough to perform in realistic environments often do not possess adequately low work function to produce asymmetric diodes. Since the multiwall CNTs used in this work have $\Phi \sim 5$ eV, a low work function material like Ca ($\Phi = 2.1$ eV) has been required to induce a practical asymmetry ($\mathcal{A} \sim 10$). This is not feasible in practice due to the immediate oxidation of Ca in air.

An alternative approach to attaining high nonlinearity, responsivity, and asymmetry is by fabricating diodes with two or more insulators. Double-barrier metal-insulator-insulator-metal (MIIM) diodes have great asymmetry, nonlinearity, and responsivity versus single-barrier MIM counterparts [53, 62–64]. The dominant tunneling mechanisms involve the configuration of the double-insulator structure. As described in Section 2.3.2, this includes resonant tunneling through a bias-dependent potential well formed between insulators; and step tunneling, where a tunneling barrier 'step' reduces the tunneling distance and increases current in one polarity.

Both mechanisms can be achieved through proper tailoring of the dielectrics with less restrictions required on the part of the electrodes. Dissimilar insulators, each having appropriate values of electron affinity, χ, and relative permittivity, ε, is the key to high diode asymmetry. The benefit of a MIIM, therefore, lies in the ability of the double-barrier structure of inducing asymmetry in structures that otherwise have minimal or no metal–metal work function difference.

This chapter covers important developments in the performance of the carbon nanotube tunneling diode array as a high frequency rectifier. Multi-insulator CNT tunneling diodes are investigated to optimize the tunneling characteristics using air-stable materials.

4.2 Asymmetry Enhancement Using Double-Insulator CIM Diodes

First, we demonstrate and study the enhancement of asymmetry using a CNT–double-insulator–metal tunneling diode (denoted as CI^2M instead of CIIM for clarity in depicting the number of insulators). The CI^2M structures that will be evaluate comprise either CNT/Al_2O_3-insulator/Ag or CNT/insulator-Al_2O_3/Ag structures (Figure 4.1(a)).

These double-barrier diodes are fabricated using similar methods outlined in Chapter 3. Vertical CNT forests are grown and then the double-insulator laminate coating is deposited with ALD. The two oxides are formed by amending the original ALD recipe to include the initial plasma pretreatment followed by sequential deposition of both dielectrics. The deposition rates and precursors are identical to the single-insulator processes described before. In this section, 8 nm total oxide thickness is used as a balance between minimizing the tunneling thickness and assuring discrete conformal coatings between dielectrics, which was established previously as ~4 nm. Finally 50 nm Ag is evaporated on the top of the array to form 0.076 cm^2 devices. The air-stable Ag electrode highlights the development of diodes that are capable of practical operation.

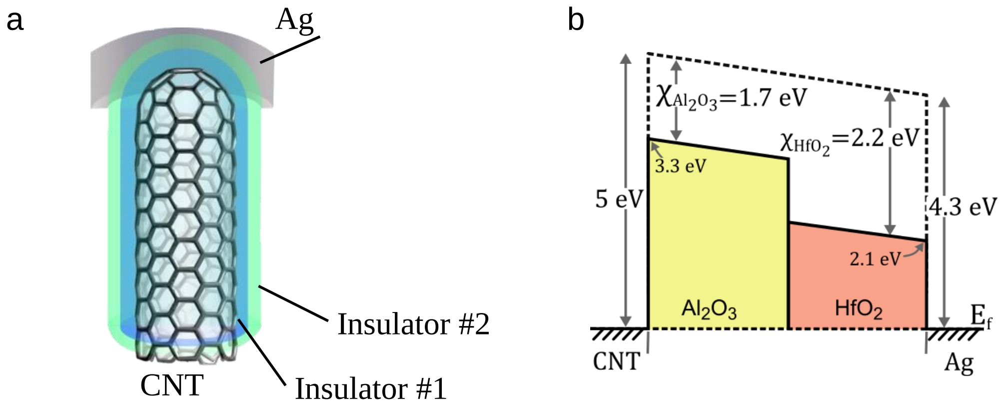

Figure 4.1. (a) Depiction of single CI^2M junction. (b) Potential barrier diagram of CNT/Al_2O_3-HfO_2/Ag with barrier edges indicated.

First, the *I*–*V* characteristics of a CNT/Al_2O_3-HfO_2 (4/4 nm)/Ag diode is measured for comparison with a comparable 8 nm CNT/Al_2O_3/Ag device. The barrier diagram of the Al_2O_3-HfO_2 CI^{2}M is shown in Figure 4.1(b) for reference. *I*–*V* curves show higher current under forward-bias for CI^{2}M than for CIM. This is also reflected in the gradual increase in asymmetry up to $\mathcal{A}\sim16$ (Figure 4.2). Nonlinearity and responsivity are also superior. At 0.5 V for instance, nonlinearity of $\mathcal{N} = 3.5$ is achieved in the double-insulator device versus $\mathcal{N} = 1.3$ in the single-insulator. Peak responsivity also doubles when incorporating two insulators. This confirms the promising nature of the double-insulator tunneling barrier in enhancing the asymmetry of CNT diodes that otherwise possess minimal work function difference.

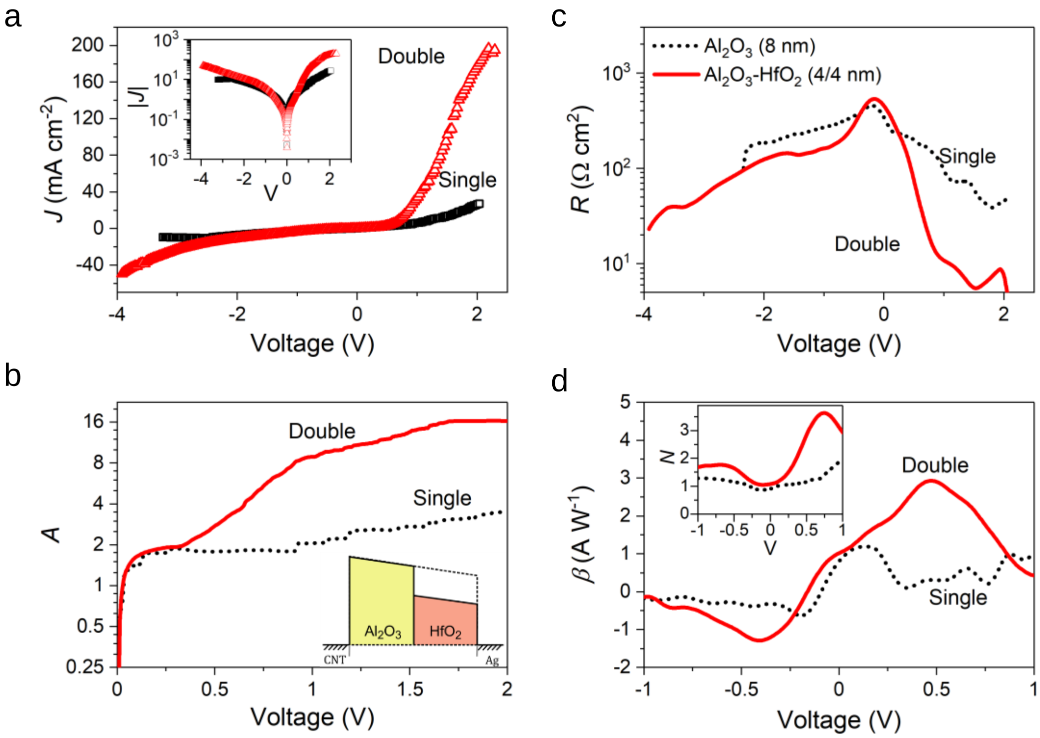

Figure 4.2. Diode electrical characteristics comparing single-insulator Al_2O_3 (8 nm) and double-insulator Al_2O_3-HfO_2 (4/4 nm) CNT devices. (a) Current density, J, (b) resistance, R, (c) asymmetry, $\mathcal{A}$, and (d) responsivity, β, with inset depicting nonlinearity, $\mathcal{N}$.

The characterization of CI^{2}M devices is expanded to including various double-layer dielectric combinations. We test the influence of the electron affinity dissimilarity (χ_1 vs. χ_2) on asymmetry using either Al_2O_3-I_2 or I_1-Al_2O_3, again with 8 nm total double-layer thickness. In general, most double-insulator structures produced some asymmetry enhancement relative to single-insulator CNT/Al_2O_3/Ag devices. Al_2O_3-HfO_2 exhibits highly nonlinear and asymmetric behavior in accordance with step tunneling between the low-χ Al_2O_3 and high-χ HfO_2. At 1 V the mean asymmetry in this structure is $\mathcal{A}(1V) = 24$, and in several devices, $\mathcal{A}(1V) > 60$ (Figure 4.3). However, the asymmetry of Al_2O_3-I_2 configurations decreases to unity as the electron affinity of the second insulator increases. As χ_2 increases, electron conduction through the second insulator transitions from tunneling to bulk-limited mechanisms, which dilutes the gains from step tunneling between the layers. We also observe asymmetry enhancement for the reversed configurations of ZrO_2-Al_2O_3 and TiO_2-Al_2O_3 (Figure 4.3). ZrO_2-Al_2O_3 demonstrates a distinct turn-on voltage around 0.5 V which suggests resonant tunneling (see $\mathcal{A}(V)$ curves in Figure B.2 of Appendix B), after which asymmetry rapidly increases to 8.

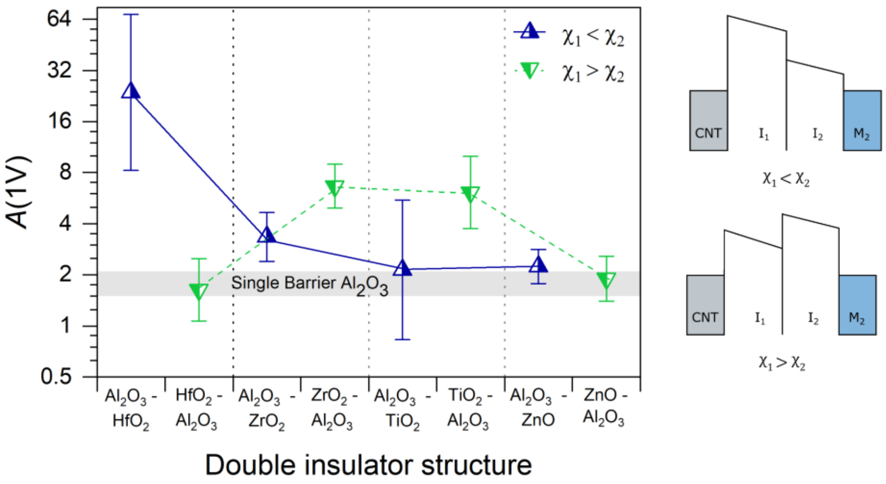

Figure 4.3. Plot of asymmetry, $\mathcal{A}(1V)$, for various CI^{2}M devices. Double-insulator structure is (4/4 nm). The shaded region represents the asymmetry range of typical 8 nm Al_2O_3 device.

Most previous work on MIIM diodes has focused on experimentally testing or simulating planar devices with various metal and insulator combinations. Alimardani *et al.* achieved $\mathcal{A} = 187$ at 1.2 V with ZCAN/Al_2O_3-Ta_2O_5/Al and $\mathcal{A} = 82$ with ZCAN/HfO_2-Al_2O_3/Al for 5 nm of insulators [53, 63]. In comparison, CNT/Al_2O_3-HfO_2/Ag, achieved a mean asymmetry of $\mathcal{A}(1V) = 24$ and peaking at 32 beyond 2 V. The mean current density of our CNT/Al_2O_3-HfO_2/Ag devices was $J = 30$ mA/cm^2 at 1 V and passing 200 mA/cm^2 past 2 V. This is an order of magnitude greater than the peak current density reported in similar ZCAN/Al_2O_3(3.5nm)-HfO_2(5nm)/Al structures [63]. Noureddine, *et al*. tuned the resonant tunneling behavior in Cr/Al_2O_3-Ta_2O_5/Al with 5 nm total insulator to achieve a maximum asymmetry of $\mathcal{A} = 8$ and $J > 200$ mA/cm^2 [65]. Our devices have been fabricated on relatively large areas (>7 mm^2) compared to existing planar MIIM diodes and are therefore capable of large, practical current levels (1 mA) [63, 64, 67].

Previous CNT/Al_2O_3/Ca devices with a work function difference of $\Delta\Phi = 2.1$ eV yielded $\mathcal{A}\sim 11$ [8]. We have shown that CNT diode arrays can be fabricated to produce even higher asymmetry with only $\Delta\Phi = 0.7$ eV through incorporating several dielectric layers. This is very promising in suggesting that work function is no longer a strict requirement for efficient diode operation. A new realm of CNT diode structures using air-stable materials is now possible.

4.2.1 STEM Confirmation of Double-Insulator Coatings

In Figure 4.4, STEM-EDS images of a multiwall CNT coated with 4/4 nm Al_2O_3-HfO_2 verify that both oxides are distinctly and conformally layered. Elemental maps allow us to confirm the thickness of each layer is 4 nm. The thickness of either dielectric varies by around ±0.3 nm over the length of an individual CNT and varies by less than 1 nm between CNTs throughout the array. Minute variations in either insulator thickness can have a profound effect on electron tunneling. This is important for optimizing diode figures of merit because insulator thickness is limited to above the level of deviation, which hinders the potential barrier geometry and puts constraints on device performance. Therefore, minimizing insulator thickness variation by improving the conformal ALD process is recommended.

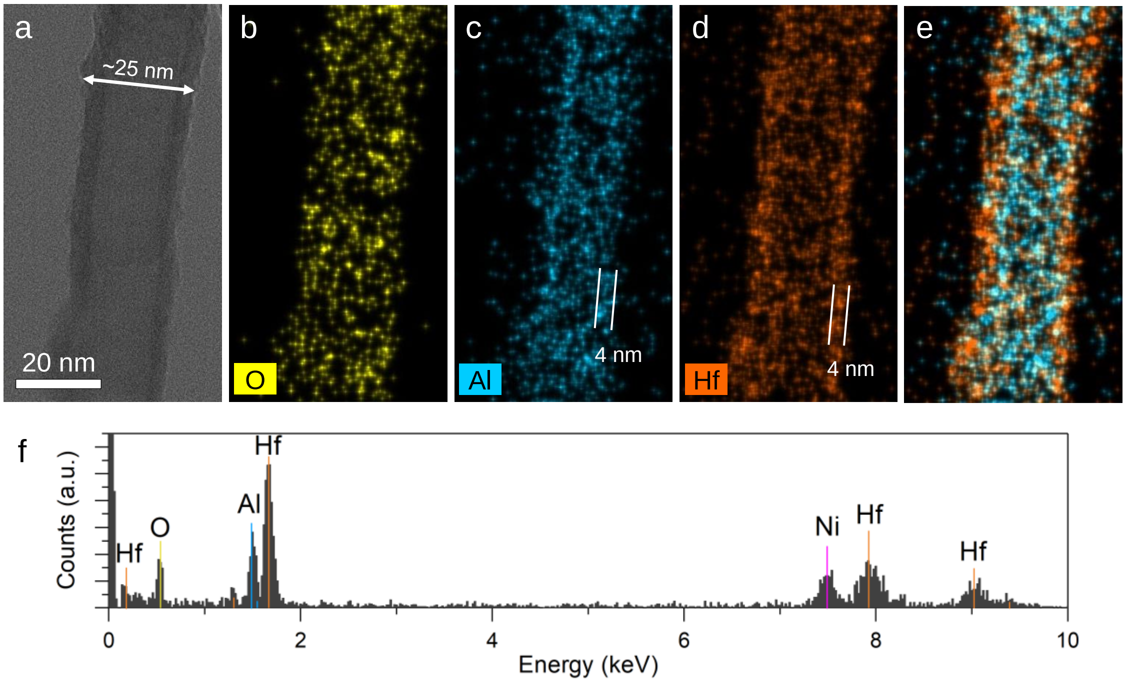

Figure 4.4. (a) STEM image, and (b-d) EDS elemental maps from a CNT coated with Al_2O_3/HfO_2 (4/4 nm). (e) Overlapping Al and Hf signals emphasize the boundary between layers. Al_2O_3 and HfO_2 coatings are both 4.0 ± 0.3 nm thick. (f) EDS spectrum of oxide-coated CNT forest (note: Ni signal is from the TEM grid).

4.3 Multi-Insulator CIM Diodes

Having demonstrated the capability for improving diode characteristics with two tunneling barriers, we will further explore the possibilities for enhanced diode performance in multi-insulator CIM diodes. This section will present an electrical characterization of multi-insulator CIM diodes having as many as four dielectric layers (note: we will use $CI^{(m)}M$ as condensed notation indicating a CNT diode with m insulators). The barrier will feature alternating layers of Al_2O_3 and ZrO_2. ZrO_2 is used as the auxiliary dielectric in place of HfO_2 as it has a larger dielectric affinity ($\chi = 2.75$ eV), giving less tunneling resistance from a lower potential barrier while not so low as to be dominated by FPE, TAT, hopping, etc.

4.3.1 Current-Voltage Characteristics of Multi-Insulator CNT Diodes

Figure 4.5 presents *I–V* characteristics of several multi-insulator CIM devices with up to four layers of insulator (alternating Al_2O_3 and ZrO_2). Total insulator thickness is 12 nm. The current magnitude is reasonably similar for all devices, which is expected for devices of the same thickness. In the CI^2M and CI^4M devices, forward current eventually surpasses that of the single-insulator CIM with enough bias. The asymmetry of the CNT/Al_2O_3/Ag is only ~2 due to the low $\Delta\Phi$. Asymmetry in the multi-insulator devices, however, all exceed that of the single-insulator CIM by several-fold at after 1.3 V forward bias (Figure 4.5(c)). Nonlinearity also improves 2–3 times. Even more promising, an enhancement in asymmetry as high as 50× can be seen for the CI^4M device.

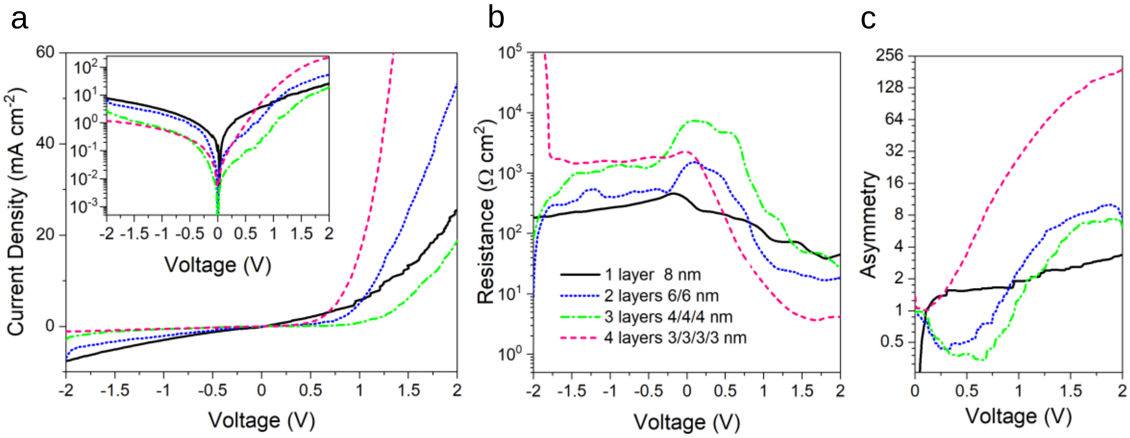

Figure 4.5. CNT diode figures of merit with varying number of Al_2O_3 and ZrO_2 multilayers.

Figure 4.6 illustrates energy band diagrams for each configuration to further understand the potential mechanisms leading to individual device behaviors. The sharp increase in forward current from Figure 4.5(a) is expected for multi-insulator diodes and this turn-on likely indicates the onset of step tunneling. The turn-on voltage at which each device demonstrates this sudden increase in current, and therefore enhanced asymmetry, varies with the number of layers (Figure 4.5(c)). For a CI^2M diode with 6/6 nm Al_2O_3-ZrO_2 turn-on begins at 0.9 V. As expected, the quad-insulator configuration with 3/3/3/3 nm Al_2O_3-ZrO_2-Al_2O_3-ZrO_2 improves the diode asymmetry and nonlinearity even further. The turn-on voltage of CI^4M is low (~0.5 V) and the sharp increase in forward current raises the asymmetry to a remarkable value of ~250. These values for turn-on voltage and the corresponding asymmetry fits what we can infer based on the potential barriers depicted in Figure 4.6(f) and Figure 4.6(l). CI^2M and CI^4M devices both exhibit step tunneling under forward bias due to the outer ZrO_2 layer. Yet, step tunneling manifest at lower bias in CI^4M since the outermost ZrO_2 layer is very thin, requiring less bias. Diodes with more than two barriers can display several tunneling mechanisms at various biases. For instance, the CI^4M barrier shown in Figure 4.6(j-l) may exhibit a combination of step tunneling over the 4th insulator (ZrO_2) at low bias, but is also susceptible to resonant tunneling due to the various quantum wells that can be formed amongst the layers at different biases.

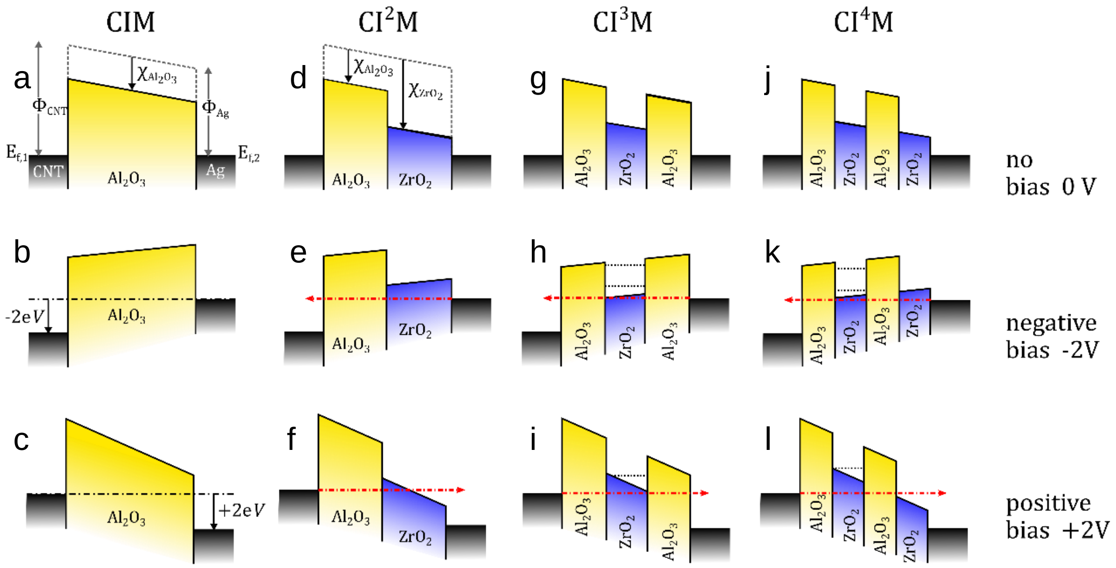

Figure 4.6. Energy band diagrams for multi-insulator CIM diodes used in this study.

Interestingly, CI^2M and CI^3M devices demonstrate rectification reversal ($\mathcal{A} < 1$) at low bias. This could be partly due to defect-enhanced tunneling [53, 55]. In CI^2M, for instance, traps in the ZrO_2 may enhance low reverse bias conduction through the layer (via TAT or PFE), coupled with tunneling through the Al_2O_3. Electrons may tunnel through traps in the dielectric before being thermally emitted to the conduction band, similar to Schottky emission [82]. As with Schottky emission, this trap-enhanced conduction is highly temperature dependent. Therefore, the performance of multilayer devices operating at elevated temperatures may be adversely affected as thermally-activated conduction mechanisms begin to dominate. The suitability of devices for thermal applications like waste-heat recovery is thus heavily dependent upon the diode structure.

The behavior of CI^3M is more complicated. We expect to see significant resonant tunneling in both directions due to the deep rectangular quantum well formed by low-barrier ZrO_2 surrounded by Al_2O_3 peaks. (Figure 4.6(g-i). However, an additional contribution from step tunneling of the inner ZrO_2 layer is possible under negative bias, which would cause reversed asymmetry. At high bias the asymmetry flips, increasing past $\mathcal{A} > 1$ as the outer Al_2O_3 layer forms a triangular barrier, leading to asymmetric Fowler-Nordheim tunneling [58].

4.3.2 Verification of Conformal Multi-Insulator Coating

Small variations in insulator thickness will greatly affect the tunneling behavior in multi-insulator devices, so we must confirm that our insulators are depositing with accurate and conformal coatings. Layer dimensions are verified by imaging a quad-insulator-coated multiwall CNT tip using STEM-EDS. The total thickness is chosen to be 16 nm to ensure each 4 nm layer is thick enough to clearly resolve. Elemental maps of Al and Zr confirms the existence of four distinct layers of Al_2O_3 and ZrO_2 (Figure 4.7). Each layer is conformal and uniform with thickness of 4 nm, as expected, and sub-nanometer variation.

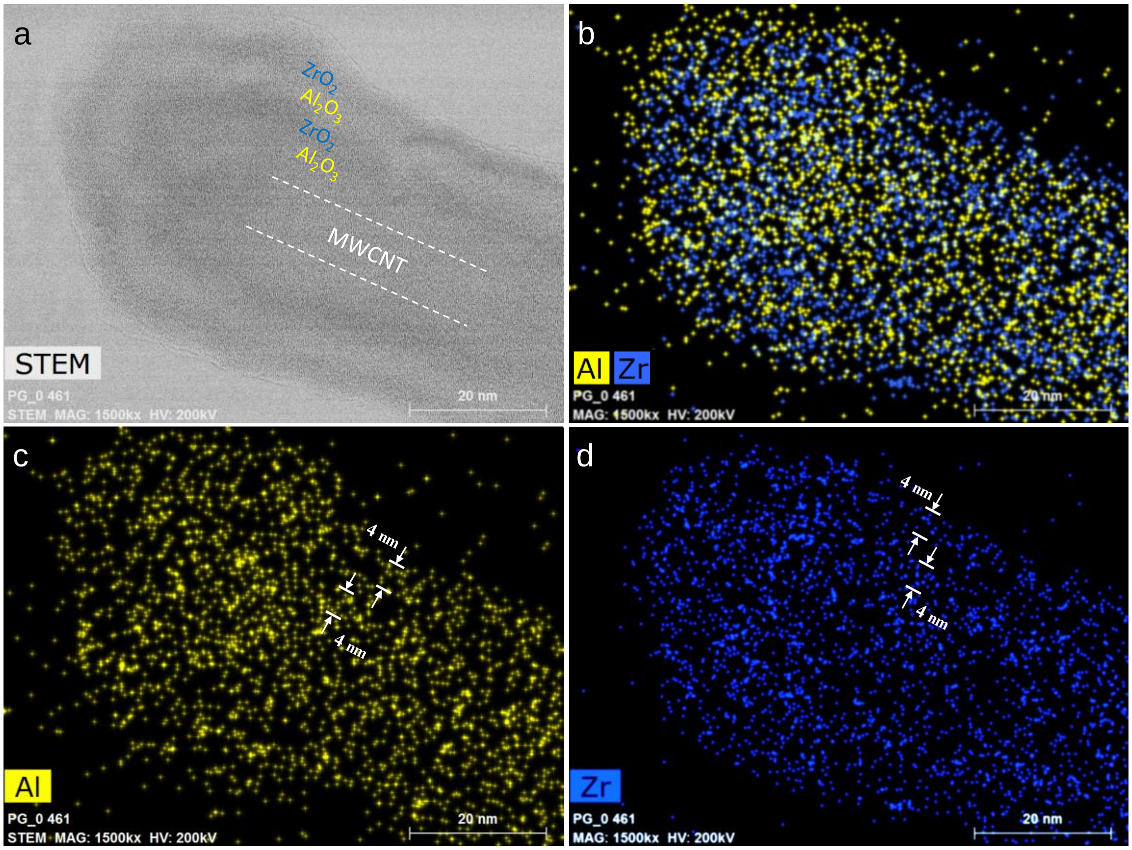

Figure 4.7. (a) STEM image of a single multiwall CNT coated with Al_2O_3-ZrO_2-Al_2O_3-ZrO_2 (4/4/4/4 nm). (b-d) Elemental maps of Al and Zr illustrate the distinct coatings and verify that each layer is 4 nm.

4.3.3 Study of Multi-Insulator Thickness on Figures of Merit

Next, in an effort to improve device operation, multi-insulator CIM diodes are examined with a range of thicknesses to further assess the impact of the additional layers on diode behavior. Each multi-layer configuration exhibits different dominant conduction mechanisms at various bias regimes, so the diode FOMs are standardized for comparison: R is taken at zero bias to assess the tunneling resistance before any turn-on occurs; $\mathcal{A}$ is evaluated at 1.5 V to ensure turn-on voltage is reached in all configurations.

We see in Figure 4.8(a) that increasing total insulator thickness results in exponentially higher resistance. This agrees with tunneling theory and is quantitatively consistent with previous reports [79, 86]. For a given thickness, the number of individual layers does not appreciably affect zero-bias resistance since conduction occurs through direct tunneling near zero bias. Though some deviation between configurations can be attributed to the difference in Al_2O_3 and ZrO_2 electron affinities causing differences in the barrier heights depending on insulator configuration. Additionally, incorporating multiple insulators significantly enhances asymmetry, regardless of thickness (Figure 4.8(b)). An 80-fold increase in asymmetry is seen for the 16 nm CI^{4}M structure, as $\mathcal{A}$ reaches 320. The turn-on voltage of this device is also even lower (~0.25 V) than observed in the earlier 12 nm CI^{4}M from Figure 4.5.

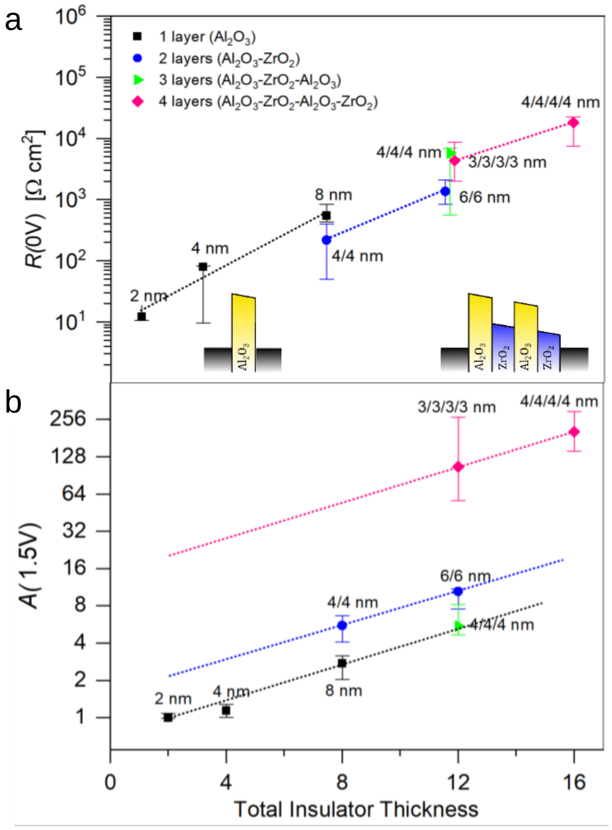

Figure 4.8. Figures of merit for CNT diodes with varying number of insulating layers (alternating Al_2O_3 and ZrO_2). (a) Zero-bias resistance, $R(0V)$ and (b) asymmetry at 1.5 V, $\mathcal{A}(1.5V)$. Colored lines, indicating 1–4 insulator layers, provide a visual guide. Insets show representative single- and quad-insulator energy band diagrams.

The low turn-on and high asymmetry are encouraging for use in optical rectennas. It is expected that the 80-fold increase in asymmetry of the CI^{4}M will translate to 10–100 times increase in rectenna conversion efficiency. For photon-assisted tunneling, the open-circuit voltage is particularly dependent upon the turn-on voltage of the diode relative to the photon energy of the incident radiation. Therefore, the reduced turn-on voltage of ~0.25 V implies a broad wavelength range of rectification <5 µm is possible.

Before devices can be optimized for specific wavelengths of radiation the electron transport of the diode must be improved. The expansive characterization of multi-insulator CIMs with various geometries enables better design of the device towards specific applications by selecting the insulator configuration that will give optimal performance in the desired operating regime.

4.3.4 Capacitance Measurement

As the electrical characteristics of these improved CNT diodes has been established for various thickness, the inclusion of multiple dielectric combinations brings about questions concerning the capacitance of these newfound diode. Sharma *et al.* reported single-junction capacitance as low as 1.7 aF for 8 nm Al_2O_3. For multi-insulator diode structures capacitance is affected by both materials' dielectric constant. Any difference in capacitance between a device with a single layer of Al_2O_3 and multiple layers of Al_2O_3 and ZrO_2 will directly impact the RC coupling efficiency.

Capacitance was determined for the CNT/Al_2O_3/ZrO_2/Al_2O_3/ZrO_2(2/2/2/2 nm)/Ag diode. The individual diode capacitance was estimated by first measuring the overall device capacitance with an Agilent E4980A LCR meter up to 1 MHz and a.c. amplitude of 50 mV_{rms}. Since the device is composed of an array of CNT diodes acting in parallel, the average junction capacitance, C_D, can be calculated based on the equivalent capacitance, $\bar{C}$, of a parallel network of diodes using the expression

$$\bar{C} = \sum C_i = nC_D = (\rho_n A)C_D. \tag{4.1}$$

The total number of CNT diodes, n, is the product of the CNT number density (ρ_n~10^{10} CNT/cm^2) and the device area (A = 0.076 cm^2). For the Al_2O_3/ZrO_2/Al_2O_3/ZrO_2 device, capacitance was measured in the range of $\bar{C}$~ 2.3–3.0 nF. The capacitance per junction is calculated as C_D~ 3.5 ± 0.5 aF (Figure 4.9).

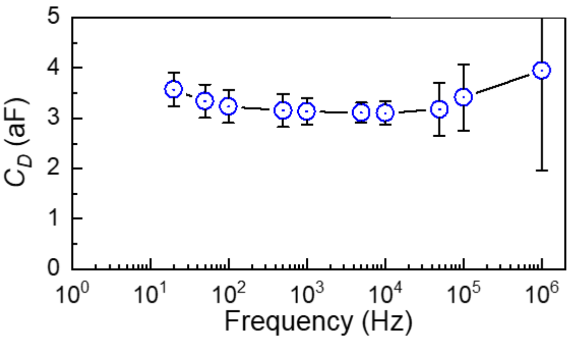

Figure 4.9. Junction capacitance, C_D, of a 8 nm CNT/Al_2O_3-ZrO_2-Al_2O_3-ZrO_2/Ag diode.

4.4 Summary

CNT diode arrays have been demonstrated utilizing multiple dielectric layers to tailor and enhance tunneling. The multi-insulator diodes boast improved performance while retaining air-stable materials. The double-barrier CI^2M devices exhibit 3–10 times asymmetry magnification relative to an equivalent single-barrier diode. It has also been established that increasing the insulator layers improves asymmetry and nonlinearity with minimal penalty to resistance. The CI^4M device, comprising multi-layer Al_2O_3-ZrO_2-Al_2O_3-ZrO_2 structure displays outstanding asymmetry >100 with a turn-on voltage as low as 0.25 V. The combination of asymmetry and low turn-on voltage meet valuable requisites for optical and IR rectification. Moving forward, this study provides a foundation upon which it is possible to further engineer these multi-insulator CNT diode structures to attain an efficient high frequency rectifier.

CHAPTER 5. OPTICAL RECTIFICATION IN MULTI-INSULATOR CNT RECTENNAS

This chapter marks the important evolution of the CNT rectenna by providing demonstrations of optical rectification in air using the nonvolatile diodes developed in Chapter 4. Herein, optical tests are carried out with the improved CI^{2}M and CI^{4}M diode structures and rectenna behavior is examined with respect to the diode properties. Last, a robust CI^{4}M rectenna, possessing impressive reliability and measurement consistency, facilitates a thorough examination of optical rectification across the visible spectrum.

5.1 Methods

CNT rectennas featuring several different multi-layer CIM diode structures are tested for optical response. Fabrication details of the individual CNT diode structures follow the methods outlined in Chapter 4. To assess the relationship between diode properties on optical rectification, diodes featuring combinations of Al_2O_3-HfO_2 and Al_2O_3-ZrO_2 are chosen. Insulator thickness was also varied to obtain differing values of diode FOMs.

Optical characterization implemented monochromatic laser diodes connected to a thermoelectrically cooled mount (Thorlabs TCLDM9). Lasers with wavelengths between 404 nm (742 THz, 3.07 eV) and 1064 nm (282 THz, 1.16 eV) were passed through a diffuser to produce uniform illumination over the device and minimize potential thermoelectric effects. Laser intensity up to $P_{in} = 200$ mW/cm^2 was used[‡]. The typical device area was $A = 0.076$ cm^2. All electrical and optical measurements were carried out in air at room temperature (depicted in Figure 5.1). Device electrical characteristics were

---

[‡] Incident power and intensity will both be expressed using P_{in}, with areal units denoting intensity according to device nominal area.

assessed ahead of time to confirm reasonable diode characteristics. Dark *I*–*V* curves were recorded between optical measurements to verify diode consistency.

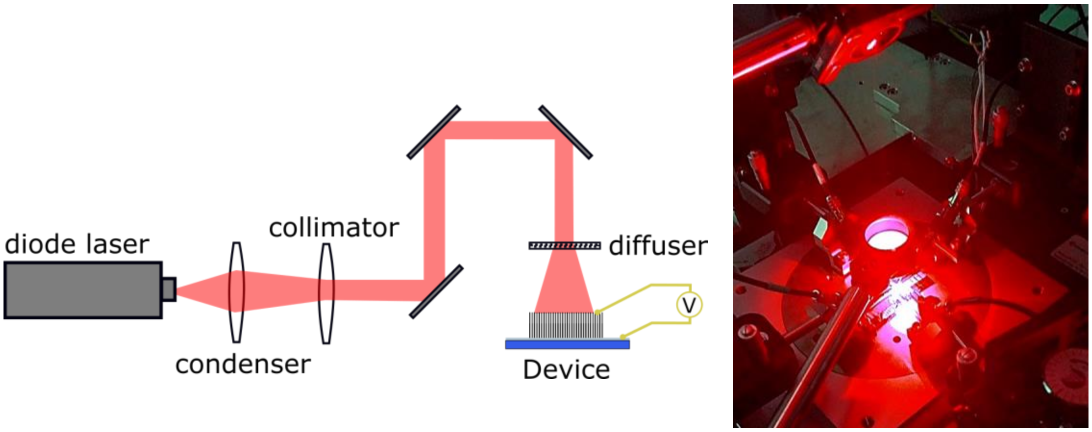

Figure 5.1. Optical test setup and photograph of device under testing.

5.2 Demonstrated Air Stable Rectification

The CNT/Al_2O_3-HfO_2/Al structure marks the first demonstration of rectenna power conversion in air using laser power on par with terrestrial solar intensities [86]. This specific double-insulator Al_2O_3-HfO_2 (4/4 nm) diode configuration achieves good asymmetry $\mathcal{A} \sim 5$, current density around 0.8 mA/cm^2, and peak diode responsivity of 3 A/W. The low turn-on voltage (0.4 V) maintains high voltage response.

Upon illumination with 638 nm and 1064 nm lasers at 20 mW/cm^2, devices exhibit an increase in forward current and second quadrant power generation consistent with optical rectification (Figure 5.2) [20, 74]. To eliminate other sources of photo-generated voltage, we tested for the thermoelectric effect (using a device with 100 nm fully opaque top metal) and band gap effect (using a device with no oxide layer) and observed no measurable response. The measured optical open-circuit voltage and short-circuit current density are $V_{oc} = –11$ mV and $I_{sc} = 0.5$ μA/cm^2; we note that the V_{oc} reported here is approximately two orders of magnitude higher (Figure 5.2(c)) in the visible and near-IR than the single-insulator CNT/Al_2O_3/Ca device from Sharma *et al.* [8]. The the open-circuit voltage response is 7.6 V/W making these devices a possible candidate for photodetection. In contrast, the previous CNT/Al_2O_3/Ca rectennas had current density up to 2000 mA/cm^2

compared with ~1 mA/cm^2 in the CNT/Al_2O_3-HfO_2/Al devices under similar illumination. The reduced photocurrent can be linked to the higher CI^{2}M diode resistance, which is due to the lower work function difference from Al ($\Delta\Phi = 0.7$ eV) in comparison to Ca ($\Delta\Phi = 2.1$ eV) [8]. Despite lower I_{sc}, the substantial increase in photovoltage gives a 10-fold increase in conversion efficiency to 7×10^{-6} %. Most importantly, this structure is air-stable, which represents a major accomplishment for rectenna.

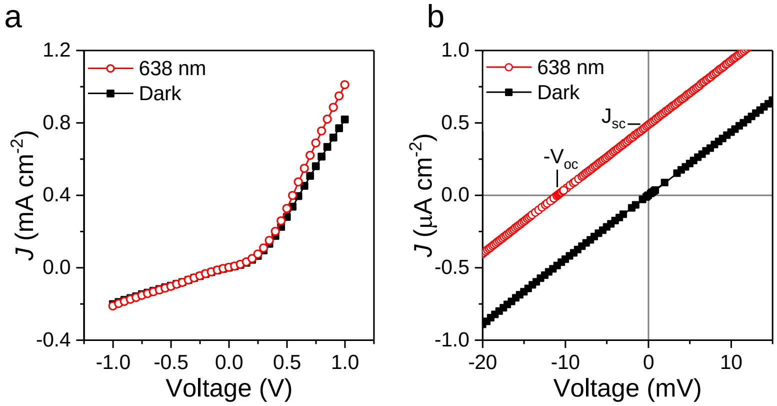

Figure 5.2. Optical rectification of visible light using CNT/Al_2O_3-HfO_2 (4/4 nm)/Al rectenna device. (a) *I–V* characteristics show an increase in forward current under 638 nm illumination. (b) High resolution scans indicating V_{oc} and I_{sc}.

A comparable Al_2O_3-HfO_2 diode with Ag as the top electrode was also tested. The particular device only had $\mathcal{A} \sim 2.7$ and did not produce a measurable rectenna photoresponse. This underscores the importance of the diode asymmetry on rectifier ability.

5.2.1 *Tuning the Multi-Insulator CNT Diode for Efficient Rectification*

Next, additional multi-layer CIM diode structures were tested under illumination to study the impact of diode characteristics on optical response. An overview of the optical responses, diode FOM, and the generating device structure is summarized in Table 5.1. In each case, conversion efficiency is calculated at the maximum power point (MPP) and relative to the incident laser power, $\eta = P_{out}(V_{MPP})/P_{in}$. First, it is apparent that the η scales with both asymmetry and current density. Specifically, the V_{oc} is improved by orders of magnitude with marginal increase in $\mathcal{A}$. Devices that incorporate more insulator layers display progressively better asymmetry, such that V_{oc} nearly 100 mV can be achieved with a CI^{4}M diode. On the other hand, it is clear that device conductance is largely linked to the short-circuit current responsivity, β_I. The devices having a thick insulator displayed high resistance from reduced tunneling probability. As a result, β_I was less lessened at a rate of about one decade for every 2.5 decade reduction in diode current. Of course, these trends neglect to account for the wavelength and power dependence of the rectenna response. Nonetheless, the results provide useful qualitative insight into the effect of diode FOMs for which to motivate and guide additional study for Section 5.3.

Table 5.1. Response to illumination for various CNT rectenna structures studied in this body of work.

Device Structure	**Diode FOM**		**Illuminated Response**				
	I_{1V} (A/cm^2)	$\mathcal{A}_{1V}$ (-)	λ (nm)	P_{in} (mW/cm^2)	$\beta_{I_{sc}}$ (A/W)	V_{oc} (mV)	η (%)
CNT/Al_2O_3(8 nm)/Ca [8]	2	10	532	26	6.5×10^{-5}	-0.16	3×10^{-7}
			1064	92	7×10^{-5}	-0.69	10^{-6}
			AM 1.5 solar	100	3×10^{-6}	-0.58	4×10^{-8}
CNT/Al_2O_3-HfO_2(4/4 nm)/Al [86]	8×10^{-4}	5	638	20	2.5×10^{-5}	-11	7×10^{-6}
			1064	25	1.5×10^{-5}	-5	1.6×10^{-6}
CNT/Al_2O_3-HfO_2(4/4 nm)/Ag	10^{-2}	2.7	808	100	n/a	n/a	n/a
CNT/Al_2O_3-ZrO_2 (4/8 nm)/Al	7×10^{-5}	8	808	200	10^{-7}	-50	2×10^{-7}
CNT/Al_2O_3-ZrO_2-Al_2O_3-ZrO_2(3 nm×4)/Al	10^{-3}	60	450	30	1×10^{-5}	-63	1.9×10^{-5}
CNT/Al_2O_3-ZrO_2-Al_2O_3-ZrO_2(4 nm×4)/Al [87]	8×10^{-6}	>100	404	5	1.0×10^{-6}	-67	1.6×10^{-6}
			450	5	1.2×10^{-6}	-81	2.5×10^{-6}
			532	5	1.6×10^{-6}	-95	3.4×10^{-6}
			638	5	1.5×10^{-6}	-96	3.0×10^{-6}
			808	5	1.1×10^{-6}	-75	1.6×10^{-6}
			980	5	0.9×10^{-6}	-60	1.3×10^{-6}

Overall, highest conversion efficiency achieved to date is 1.9×10^{-5} % ($\lambda = 450$ nm, 30 mW/cm^2) in a CNT/Al_2O_3-ZrO_2-Al_2O_3-ZrO_2 (3/3/3/3 nm)/Al device. This device has a great balance of $\mathcal{A}\sim 60$ while maintaining relatively high current density of $I(1V)\sim$ 1 mW/cm^2. $\beta_I\sim$10 µA/W is nearly comparable to the CNT/Al_2O_3/Ca rectenna, except that the V_{oc} is improved by 100. With further manipulation of the tunneling structure to carefully boost current without sacrificing asymmetry, efficiency could be raised even higher. Next, a more meticulous study of optical rectification will be performed to elucidate the spectral and power dependencies on rectenna performance.

5.3 Comprehensive Optical Rectification Study Using a Robust Quad-Insulator CNT Diode

This section uses a highly robust 16 nm CI^{4}M diode structure to conduct a meticulous investigation of rectification across the full visible spectrum. The structure is composed of Al_2O_3-ZrO_2-Al_2O_3-ZrO_2 (4/4/4/4 nm) insulator stack with Al capping electrode (Figure 5.3). Even though the thick insulator concedes high tunneling resistance, the remarkable stability and repeatability of this dielectric stack makes it attractive for a much-needed fundamental study of optical rectenna device physics.

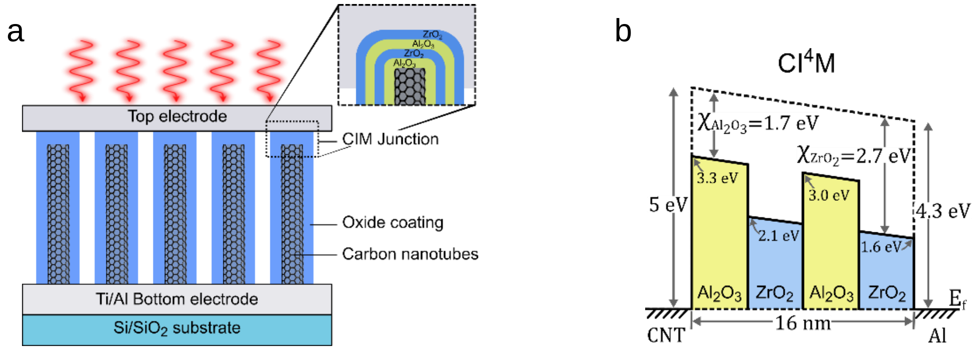

Figure 5.3. (a) Schematic of the CI^{4}M-based CNT optical rectenna comprising CNT/Al_2O_3-ZrO_2-Al_2O_3-ZrO_2/Al and 16 nm insulator. (b) Energy band diagram of the diode.

5.3.1 *Diode I–V Characteristics*

Figure 5.4 depicts the measured dark electrical response of the rectenna; this is equivalent to the diode *I–V* characteristics. The CI^{4}M diode exhibits excellent nonlinearity and asymmetry that peaks around 245, low diode turn-on voltage around 0.3 V, and peak responsivity of $\beta = 6.1$ A/W. These characteristics are suitable for optical rectification. The zero bias resistance is $10^7\ \Omega\ \mathrm{cm}^2$ is unusually high—a consequence of the thick insulator. Nonetheless, this possesses the other traits that are needed for comprehensive study of optical rectification. Namely, the structure has superior scan stability. *I*–*V* scans are consistent, even over the course of several weeks exposed to air. Devices do not show any hysteresis when performing *I*–*V* scans in both directions. Lastly, since the oxide is so thick, devices can be measured over a relatively large bias range up to ±3 V before exhibiting signs of dielectric breakdown. The measurable bias range will crucial in subsequent chapters when these measurements are combined with theory to predict rectenna behavior.

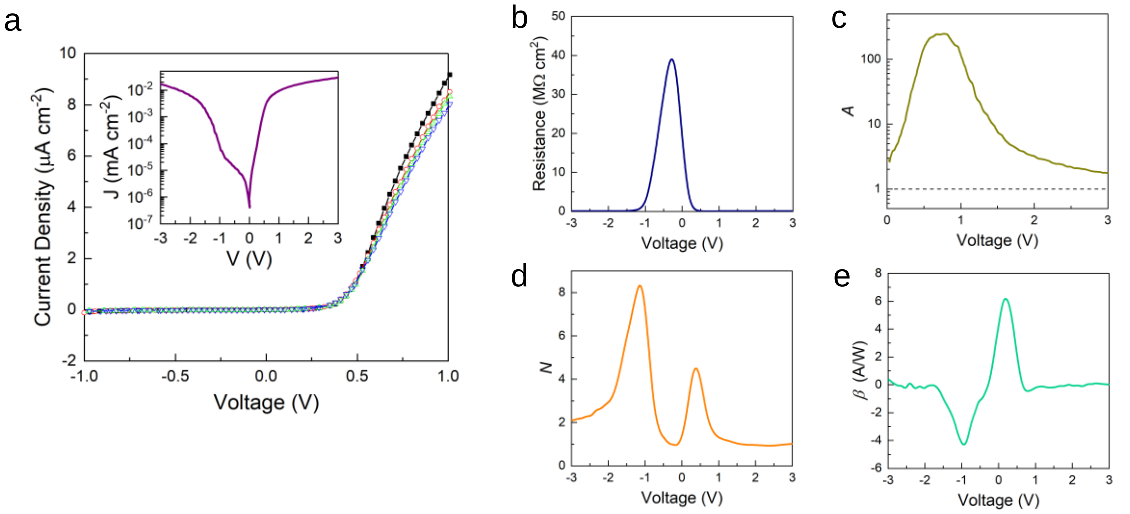

Figure 5.4. Dark *I*–*V* characteristics for 16 nm CI^{4}M device. (a) *I*–*V* curves showing device reproducibility. (b-e) Diode figures of merit: (b) resistance, R, (c) asymmetry, $\mathcal{A}$, (d) nonlinearity, $\mathcal{N}$, and (e) responsivity, β.

The diode characteristics are a result of the advanced quad-insulator laminate, which has been described previously (Figure 5.3(b)). The high asymmetry manifests at comparatively low bias due to step tunneling over the shallow outer ZrO_2 layer. The thick potential barrier maintains low reverse bias leakage current. However, this complex structure also shows inadvertent reverse bias tunneling current past –0.8 V. This could either be explained by resonant tunneling, due to a quantum well forming inside Al_2O_3-sandwiched ZrO_2 layer (layer #2), or an ancillary reverse bias step tunneling through either short ZrO_2 barriers. Next, optical rectification will be demonstrated in this structure.

5.3.2 *Optical Rectification Measurements*

Optical rectenna characterization is conducted with monochromatic lasers ranging from $\lambda = 404$ nm to 980 nm. Illuminated *I–V* curves for the CNT/Al_2O_3-ZrO_2-Al_2O_3-ZrO_2 (4/4/4/4 nm)/Al are shown in Figure 5.5. Incident laser intensity is 5 mW/cm^2 to keep the response stable and minimize sample heating (discussed in Section 5.3.2.1). There is a large increase in the forward bias current under during illumination, as well as a shift into the second quadrant—both indicators of the rectification mechanism.

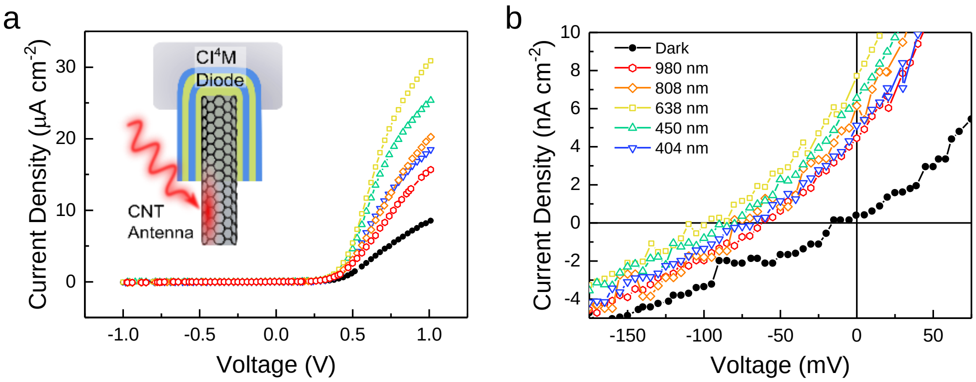

Figure 5.5. (a) *I–V* curves for 5 mW/cm^2 illumination between 404 – 980 nm. (b) High-resolution *I–V* scans.

The optical response exhibits wavelength dependence, though the trend is not monotonic with frequency. Even though the Al top electrode may exhibit wavelength-dependent transmissivity, attempts at accounting for the transmission loss in the Al did not clarify results, nor simplify this trend. This is elaborated in Section 5.3.2.2. For the wavelengths that were tested, the peak power generation occurs around 532 nm. Open-circuit voltage is $V_{oc} = –95$ mV and short-circuit current density is $I_{sc} = 8.0$ nA/cm^2. The conversion efficiency at the maximum power point is $\eta = 3.4\times10^{-6}$ %. Input power is based upon the incident intensity and does not account for possible electrode transmission losses. Efficiency is lower than the peak efficiency that was observed in a comparable 12 nm CI^{4}M diode (Table 5.1). The power loss is expected to originate from the large resistance of the thicker tunneling barrier, even though $\mathcal{A}$ and turn-on voltage are much better. It must be noted that the actual power that is input to the CNTs is expected to be much less than the incident measured power. This is explored in Chapter 6. Despite the low efficiency, voltage responsivity at open-circuit is $\beta_V = 250$ V/W, which is the largest responsivity that has been observed in all measured CNT rectenna configurations.

Figure 5.6 makes it apparent that the photocurrent is proportional to the intensity of the illumination. The measured optical response is very stable in time with a rapid ON/OFF switching that also supports rectification and not a transient photothermal phenomena. The power dependence is due to light-matter interactions in the CNT antenna, where the intensity of the incoming radiation field increases the resulting a.c. optical source voltage established over the antenna.

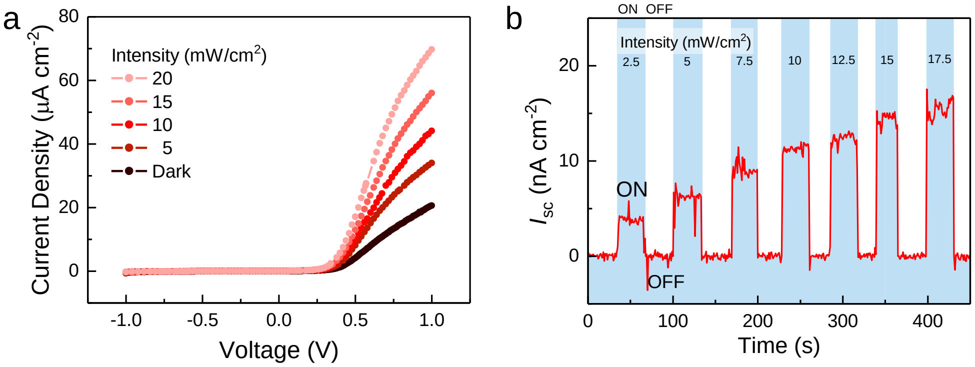

Figure 5.6. (a) I–V scans for varying laser intensity ($\lambda = 638$ nm). (b) Time-dependent short-circuit current, I_{sc}, response.

Despite the low current, the large photovoltages that can be achieved here make this device a feasible candidate for photodetection technologies. This is illustrated by estimating the detectivity as a figure of merit to classify the photodetector sensitivity. Specific detectivity is a normalized measurement that conveys how small of a signal that can be detected, expressed as

$$D^{\star} = \frac{\sqrt{A\Delta f}\,\beta_I}{I_n} \tag{5.1}$$

where A is nominal device area of 0.076 cm^2, and Δf is the system bandwidth. I_n is the noise current due to Johnson and shot noises, given by

$$I_n = \sqrt{\left(\frac{4k_bT}{R_D} + 2eI_D\right)\Delta f} \tag{5.2}$$

k_b is the Boltzmann constant; T is the absolute temperature, assume to be 300 K here for room temperature operation; R_D is the diode resistance; and e is electronic charge. Around zero bias Johnson thermal noise dominates. Figure 5.7(a) shows the estimated detectivity as a function of wavelength. The peak detectivity is $D^{\star} = 4\times10^{7}$ cm Hz$^{1/2}$/W for $\lambda = 532$ nm. This is still several orders of magnitude lower than commercially available Si photodetectors that operate in the visible spectrum. One promising advantage of the CNT rectenna as a photodetector remains its promising temperature insensitivity, as observed by Sharma *et al*. Also, because of the strong photocurrent observed under forward bias, detectivity is at least 500-fold higher if the CNT rectenna is operated as a biased detector (Figure 5.7(b)). The detectivity here is on the order of other detectors being researched for a variety of novel visible and IR applications [88, 89]. If detectivity remains high through the IR spectrum then the CNT rectenna could be a strong contender for IR sensing.

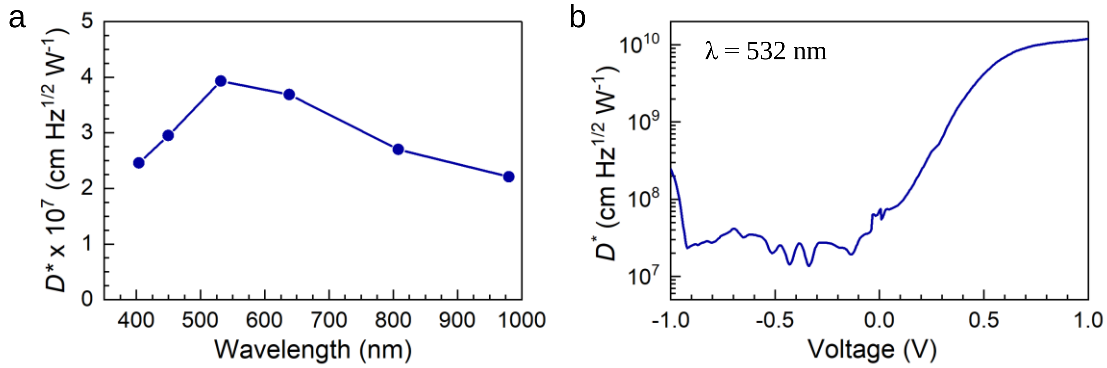

Figure 5.7. Specific detectivity, $D^{\star}$, as a function of (a) wavelength (0V) and (b) bias.

5.3.2.1 Evidence Ruling Out Thermoelectric Response

There is widespread concern that temperature gradients could induce thermal voltages that may be misconstrued for rectification [20, 90]. This section provides evidence to rule out thermal behavior. An IR camera is used to capture the surface temperature rise across the device under 100 mW laser concentrated at ~5 mm^2 spot size.

Despite this significantly higher laser intensity than optical measurements (2 W/cm^2), there was only a 2 ºC temperature differential established across the device (Figure 5.8). This was reduced nearly to zero when a diffuser was implemented. Moreover, the transient temperature rise under the laser heating is on the order of 1–10 s, illustrating that the fast photoresponse seen in Figure 5.6(c) is likely not due to sample heating.

In principle, metallic CNTs should have zero Seebeck coefficient [71]. Even if there was a thermoelectric effect between any of the metal layers or the substrate, the observed temperature difference would result in a V_{oc} several orders of magnitude smaller than the measured optical response [91]. The use of a diffuser throughout *I*–*V* measurements further mitigates any temperature gradient that might cause thermoelectric effects. We thus rule out thermally-induced behavior in the observed response.

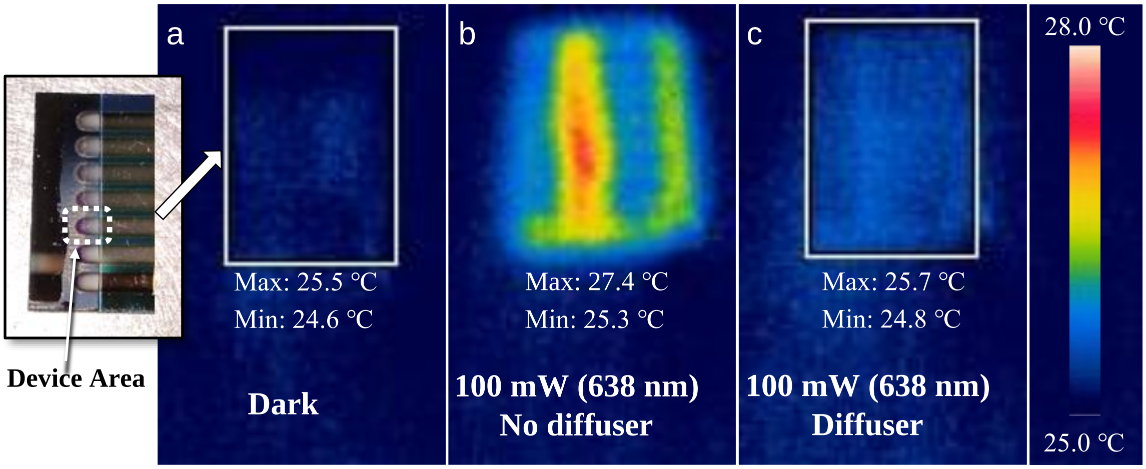

Figure 5.8. Infrared images of the rectenna device under 100 mW illumination ($\lambda = 638$ nm) show only 2 °C temperature rise with direct laser beam and no significant temperature change under a diffuser.

5.3.2.2 Transparency of Top Electrode

The input power that is experimentally measured does not consider reflection or transmission through the top metal layer before passing into the CNT array for antenna absorption. Here we attempt to account for transmission losses and the effect on the internal rectenna power conversion efficiency. 50 nm planar Al was deposited on glass. The transmittance was calculated for each available wavelength of laser by measuring the transmitted power through the glass slide. Values were adjusted to account for the ~90 % transmittance of the glass. The resulting Al transmission was therefore estimated in the range of 1–6 % across the visible spectrum, shown in Figure 5.9(a).

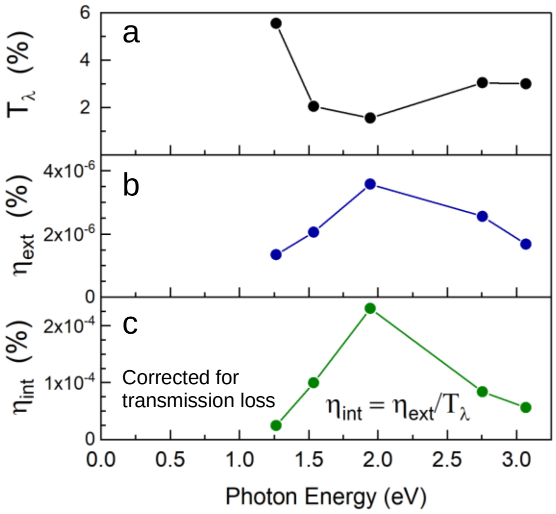

Figure 5.9. (a) Spectral transmission T_λ as a function of photon energy for 50 nm planar Al. (b) External conversion efficiency, η_{ext}, based on measured incident power. (c) Internal conversion efficiency based on the power transmitted through the Al: $\eta_{int} = \eta_{ext}/T_\lambda$.

To estimate the effect of spectral transmittance on rectenna conversion efficiency, the conversion efficiency was calculated based on the net transmitted power, giving the internal power conversion efficiency of $\eta_{int} = \frac{P_{out}}{P_{transmitted}} = \frac{P_{out}}{T_\lambda \times P_{incident}} = \eta_{ext}/T_\lambda$. Overall, accounting for T_λ improves the internal conversion efficiency to 2.3×10^{-4} % at $\lambda = 638$ nm.

However, we emphasize caution when assuming correspondence between the planar Al metal and metal-coated CNT forest. In Chapter 6 we will see that accounting for power losses through transmission in this way does not fully capture the discrepancy in input power that is suggested by a model of photon-assisted tunneling. It is suspected that the mesh of metal-coated CNTs allows light to diffusely reflect and pass through the gaps deeper into the array until ultimately being absorbed by CNTs. In this situation, the real input power to the CNT rectenna junctions might be independent of the Al metal transmittance. Therefore, to prevent erroneous calculations and provide consistent efficiency metrics, CNT rectenna conversion will continue to be based upon the measured external laser power that is incident upon the device.

5.4 Summary

This chapter has provided study of the CNT rectenna using improved, air-stable multi-insulator CIM diodes. Evidence points to the first demonstration of optical power rectification in air, to the best of our knowledge. This is accomplished with a CNT/Al_2O_3-HfO_2/Al diode that demonstrates $\eta = 7\times10^{-6}$ %. A variety of CNT rectenna structures are then tested to discern the effect of diode properties on rectified response. Ultimately, a maximum efficiency of 1.9×10^{-5} % is measured in a high asymmetry CI^{4}M rectenna. This marks a 20-fold improvement (60-fold in the visible spectrum) relative to the first rectenna conceived by Sharma *et al*. We can infer from device testing that efficiency can be further improved by mitigating tunneling resistance. Despite the remarkably improved rectenna response, one outstanding issue with the multi-insulator diode is in the fabrication variability. Deviations from variability in the insulator is further compounded by the multiple layers. This has led to degradation during prolonged electrical measurements that limits the minimal thickness of the oxide layers during the present fabrication process.

Lastly, a stable 16 nm CI^{4}M rectenna facilitates in-depth optical measurements across the visible spectrum. The device reveals a wavelength-dependent rectenna response. Further clarification of the wavelength dependency—along with the role of power losses, antenna mechanism, and a.c.-to-d.c. transmission losses—is needed. Next, these optical measurements will be examined in light of photon-assisted electron transport to broaden our understanding of the fundamental rectification processes within these CNT devices.

CHAPTER 6. MODELING PHOTON-ASSISTED TUNNELING IN CNT RECTENNAS

Photon-assisted theory (PAT) theory is used here to model the illuminated rectenna behavior. The measured dark *I*–*V* behavior is inserted into the PAT equation to simulate the rectenna response in relation to the corresponding experimental optical measurements described in Section 5.3. The comparison of simulations to measurements allows us to better understand the rectification mechanism in the CNT device. This also elucidates loss mechanisms such as the antenna-diode coupling mismatch and provides guidance for device improvements.

6.1 Theory of Photon-Assisted Tunneling

We use the Tien-Gordon approach of PAT described in Section 2.4.1 to elucidate the effect of optical illumination in our rectenna devices. As a review, absorption of incident light in the antenna produces an optically-induced a.c. signal, given in relation to the incident power through

$$V_A = \sqrt{8R_A P_{in}}\ . \tag{6.1}$$

V_A acts as an a.c. voltage source which establishes a corresponding a.c. voltage, V_ω, across the diode. Through PAT, electrons can gain or lose energy in quantized multiples of the incident photon energy, $V_{ph} = \hbar\omega/e$. This is reflected as corresponding shifts in the d.c. *I*–*V* response of the diode, $I_D(V)$. The net current produced through the diode as a result of photon-assisted transport is the sum of all possible photon modulations, weighed according to the probability of an electron having a shift of $n\hbar\omega$. The resulting PAT equation that describes the net illuminated current is then

$$I_L(V) = \sum_{n=-\infty}^{\infty} J_n^2(\alpha)\, I_D\big(V + nV_{ph}\big). \tag{6.2}$$

$\alpha = \frac{eV_\omega}{\hbar\omega} = \frac{V_\omega}{V_{ph}}$ is a measure of the a.c. field strength in relation to the photon energy. The key feature of the equation is that $I_L(V)$ can be calculated from the diode, $I_D(V)$. Since the *I*–*V* characteristics of our CNT diodes have already been measured, we can estimate the illuminated response. To use equation (6.2) the a.c. diode voltage has be calculated. V_ω is related to V_A according to the coupling between the antenna and diode components, described by the equivalent rectenna circuit (Section 2.1.1). For an ideal, piecewise linear diode, V_ω ranges from $\frac{1}{2}V_A$ to V_A [6, 74, 92].

There are several frequency dependent factors at play in this system, including the antenna performance, the diode a.c. characteristics and response time, and the general behavior of the metals and dielectrics at optical frequencies. As a consequence, we cannot outright predict V_A and V_ω for our system. Instead, any speculative frequency dependencies that may occur will be combined, and we will consider V_ω directly.

The frequency dependent optical properties of the diode materials can also cause a considerable deviation between the actual a.c. *I*–*V* characteristics of the diode with the measured d.c. characteristics. Belkadi *et al.* [93] pointed out that for the potential energy barrier of a multi-insulator MIIM structure is altered at high frequencies due to optical frequency dependent voltage division between the tunneling structure of both dielectric layers. This manifests as a pronouncedly different tunneling current for the diode under a.c. than for d.c. This is brought up in Section 6.3.2 whereupon we model the rectenna response at high bias. In general, since the real optical frequency a.c. diode characteristics cannot feasibly be measured, the PAT model must rely on the d.c. diode measurements.

6.2 Methods of Simulating Photon-Assisted Tunneling

The illuminated response of the CNT rectenna device is simulated by modeling PAT theory in MATLAB. The developed model is initially verified in relation to other reported PAT simulations using an ideal diode (Appendix C).

Since this chapter is focused on validating the PAT mechanism in the CNT rectenna and advancing our fundamental understanding of device operation, simulations are compared to the illuminated *I–V* curves from the rigorously measured 16 nm CI^{4}M device. Briefly, the dark *I–V* characteristics of the diode from Figure 5.4 are used to calculate the optical response while V_ω is determined by fitting the theory to measured optical scans.

Since our diode can only be measured up to ±3 V, extrapolation is required in order to use equation (6.2) to a high order of terms. For instance, at a photon energy of $V_{ph} = 3.5\,\mathrm{eV}$, taking the PAT summation out to the second order requires $I_D(V)$ extrapolated to a window of at least $nV_{ph} = \pm 7\,\mathrm{V}$. Indeed, we extrapolate our *I–V* characteristics by separately fitting the positive and negative currents to the Simmons tunneling equation for high bias regimes [45]. At low bias, the *I–V* curves are interpolated with a high order polynomial since the Simmons equation does not match our measurements over the entire bias window. Figure 6.1 shows the extrapolated $I_D(V)$ curve alongside the measured *I–V*. An analysis of the error associated with this extrapolation in relation to the truncation error from approximating the infinite sum was conducted. This is presented in Section 6.2.2 in order to verify the efficacy of the PAT model. We calculate $I_L(V)$ from equation (6.2) with the summation approximated to the highest order n that the extrapolated scan window permits based on photon energy (>2).

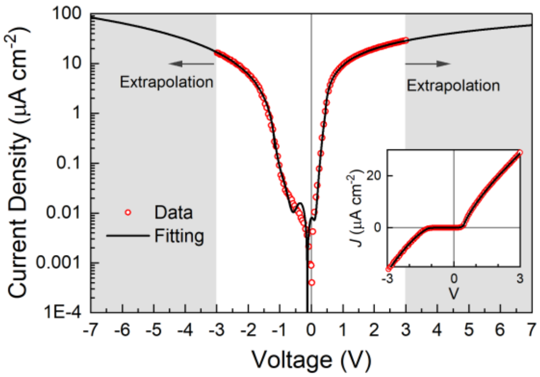

Figure 6.1. Extrapolation of the diode *I–V* to high bias to facilitate photon-assisted tunneling.

For the PAT simulations to accurately predict the response of our CNT rectenna devices, V_A has to be known to determine V_ω. However, we do not have a reliable estimate of the precise power that is absorbed in the antenna (transmission uncertainty, etc.), nor do we have direct measurements of the antenna resistance. Therefore, we will use our existing optical *I*–*V* measurements (Figure 5.5) to which the PAT model can be fit to determine V_ω at each wavelength of available scan data. Fitting of equation (6.2) to our measured scans of $I_L(V)$ is performed using the Levenberg-Marquardt algorithm for nonlinear least-squares fitting. We will see that this approach is useful in gathering evidence that helps us better understand the CNT nanoantenna operation in this rectenna, as well as the diode RC response time. Figure 6.2 shows a process flow diagram of the procedure used to estimate the unknown PAT parameters. The known diode $I_D(V)$ characteristics are inserted into the PAT equation along with an initial guess for V_ω to calculate $I_L(V)$. Then this estimated $I_L(V)$ is compared to measured scans of corresponding wavelength. The Levenberg-Marquardt algorithm calculates new parameter values and the process repeats until convergence is reached.

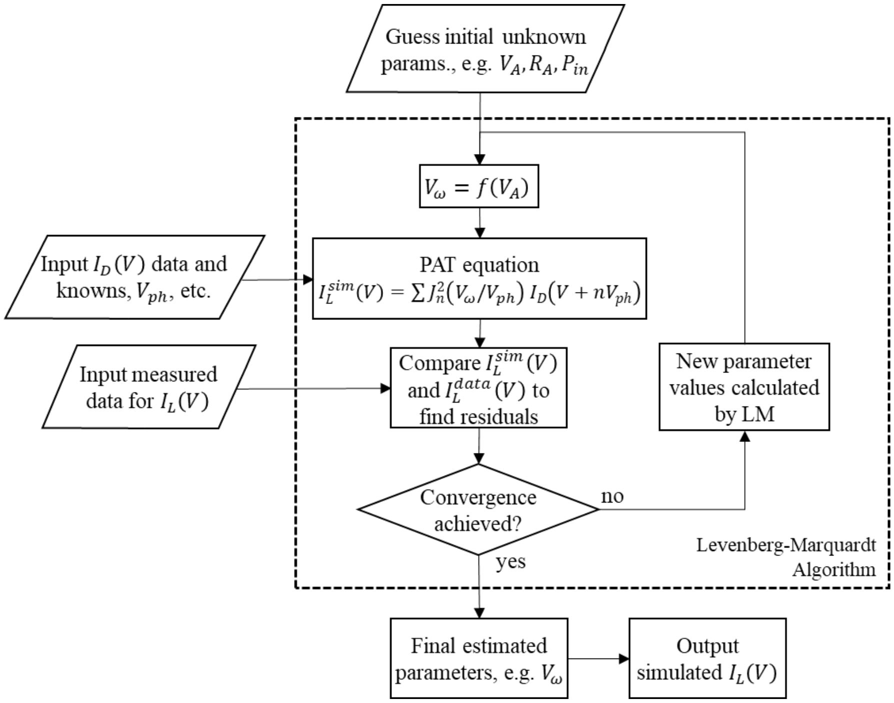

Figure 6.2. Flowchart of method used to determine the rectenna illuminated current, $I_L(V)$ using the Levenberg-Marquardt fitting algorithm.

It also must be pointed out that V_ω can vary with bias depending on whether the rectenna is assumed to have constant a.c. power delivered through the diode when the load is changed or whether the a.c. voltage is held fixed. In practical operation rectennas function under constant power mode since the power delivered by the incident light is fixed. In such a case the nonlinear resistance of the diode causes V_ω to change as a function of the applied bias. The equations and procedure that cover how to determine $V_\omega(V)$ is covered in Section 6.2.1.

For simplicity, first attempts at simulating the PAT behavior assume $V_\omega \approx V_A$ is a constant with respect to bias. However, we will see that more accurate correlation to the measured optical response is gained by actually assuming $V_\omega = V_\omega(V)$ via constant power operation. In this case, $V_\omega(V)$ is found through iteration based on the procedure outlined in Section 6.2.1.

6.2.1 *Constant a.c. Power Operation*

There are two conditions for PAT theory that must be considered when treating the equivalent circuit rectenna model. The first is for constant a.c. voltage operation, whereupon $V_\omega \propto V_A$ is a constant with respect to applied bias. The second, alternative condition is the assumption of constant a.c. power being provided to the diode. This latter mode is more practical to physical device operation. Under the assumption of constant a.c. power, the a.c. diode voltage is found from the rectenna equivalent circuit model through

$$V_\omega(V) = V_A - I_\omega(V)R_A \, . \tag{6.3}$$

I_ω is the higher order a.c. harmonics that are dropped during the derivation of PAT, calculated by

$$I_\omega(V) = \sum_{n=-\infty}^{\infty} J_n(\alpha)[J_{n+1}(\alpha) + J_{n-1}(\alpha)] \times I_D\big(V + nV_{ph}\big) \, . \tag{6.4}$$

To demonstrate the different results from these two modes of operation, we examine the simulated response by modeling PAT under both constant V_ω and constant P_{ac} conditions.

6.2.2 *Error Analysis*

First, we assess the error resulting from truncating the infinite sum of the PAT equation. Equation (2.27) implies that $I_L(V)$ is found from modulating the dark *I*–*V* by $\pm n$ multiples of V_{ph} then weighting successive contributions with the Bessel function of corresponding order. When the argument for the Bessel function is small ($\alpha < 1$)—as is the case for our devices tested at optical frequencies—then $J_n^2(\alpha)$ monotonically decreases. However, there is a tradeoff due to limited device bias range over which our devices are stable. For the device examined here that range is ±3 V before device breakdown; outside of that range, PAT simulation of high frequency light warrants diode extrapolation.

We are therefore interested in evaluating the effect of V_{ph} on the minimum number terms needed to maintain low truncation error and to determine how much extrapolating $I_D(V)$ (Figure 6.1) affects the predicted $I_L(V)$. Within the PAT model, relative error for the n^{th} term is calculated through

$$\epsilon(n) \equiv \left|\frac{I_{L,n} - I_{L,n-1}}{I_{L,n-1}}\right| = \left|\frac{J_n^2(\alpha)\,\left[I_D\left(nV_{ph}\right) + I_D\left(-nV_{ph}\right)\right]}{I_{L,n-1}}\right|. \qquad (6.5)$$

This expression counts contributions from both $+n$ and $-n$ for simplicity. The following analysis of error, ϵ is analyzed at 0 V bias for reference. $V_\omega(0V) = 90$ mV, is used, as determined by earlier fit to experimental illumination data.

Figure 6.3 shows that a summation up to 4th order terms is sufficient to guarantee relative error $\epsilon < 1$ % down to $V_{ph} = 0.1$ eV. This required number of terms drops at higher frequencies as the photon energy is more dominated by quantum regime of rectenna operation. Still, higher photon energy causes large shifts in the modulated diode current, this inevitably exceeds the range of measurable diode *I–V*. As depicted in the figure, for V_{ph} <1.5 eV an error under 1 % is guaranteed within the ±3 V device range. However, larger photon energy requires extrapolation of the *I–V* curves. At this point, it is necessary to balance the error introduced from truncating higher order terms with the uncertainty introduced from utilizing extrapolated *I–V* behavior. For instance, at $V_{ph} = 3.5$ eV, n >2 is needed to achieve minimal relative error below 1 %, hence requiring extrapolation to 7 V bias. If the real diode tunneling current significantly deviates from our extrapolated estimation at such high bias, then the error may be severalfold higher than 1 %. Until devices capable of stable measurement over a larger range are realized, the PAT model that uses real diode *I–V* characteristics should be used with appropriate caution. In this case, photon energies surpassing 1.5 eV should be taken with increasing scrutiny.

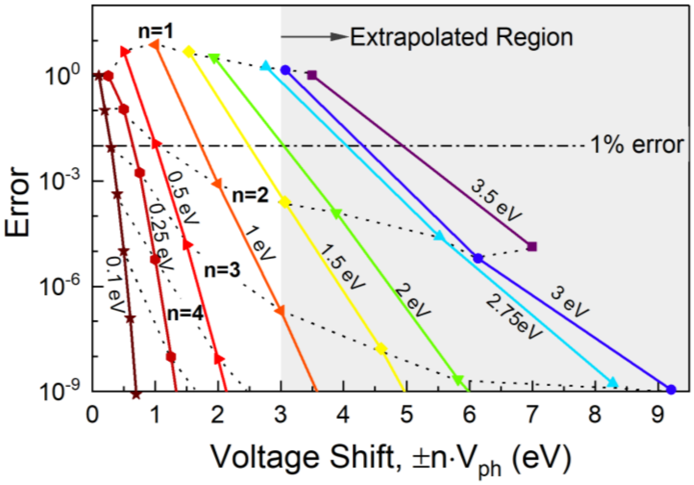

Figure 6.3. Relative error in $I_L(0V)$ from successive terms of the PAT equation, plotted as a function of the diode energy shift, nV_{ph}. The gray region marks when the diode modulation uses the extrapolated portion of the dark *I*–*V*.

6.3 Simulation Results and Comparison to Measurements

The simulated PAT response for 638 nm (1.94 eV) light is presented in Figure 6.4 in comparison with measured data. Fitting for the a.c. diode voltage—initially assumed to be a constant—gives V_ω = 68 mV (Figure 6.4(a)). It follows that $\alpha = 0.035$, which is the quantum regime. The simulated *I*–*V* curve exhibits the reduction in zero-bias resistance that is expected for a semiclassical rectenna [8]. Still, the model does not fit the slope of the measured data well, and this deviation becomes even more pronounced at higher bias.

By adjusting the model to operate on the principle of constant a.c. power instead of constant V_ω, and henceforth solving for bias dependent $V_\omega(V)$ through equations (6.3) and (6.4), we now see excellent agreement between illuminated *I*–*V* scans and the PAT prediction (Figure 6.4(b)). In the same case of $\lambda = 638$ nm, a.c. diode voltage varies steadily from $V_\omega(0V) = 81$ mV to $V_\omega(V_{oc}) = 58$ mV at the $V_{oc} = –96$ mV. This provides important evidence that our CNT rectennas operate under a constant power condition rather than constant V_ω, and highlights the importance of the impedance in designing to an intended operating point for optimal power transfer.

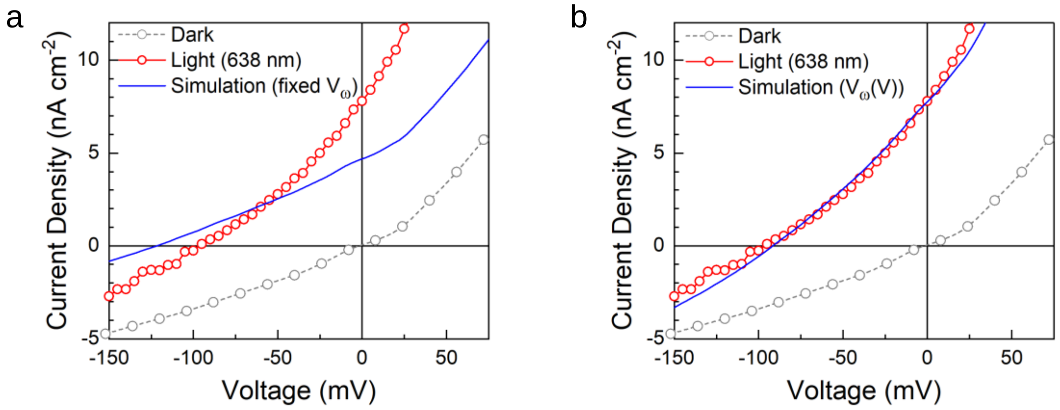

Figure 6.4. *I–V* curves for measured data (markers) at λ = 638 nm and P_{in} = 5 mW/cm^2 compared to PAT simulations for (a) constant a.c. voltage mode of operation and (b) constant a.c. power mode.

6.3.1 Frequency Dependence

Next, PAT is simulated over a range of frequencies to investigate how the photon energy and input power affect the optical response. First, $V_\omega(\omega)$ is determined by fitting the model individually to the *I–V* data of each available wavelength. Based on the implications from Figure 6.4, constant a.c. power operation was assumed.

Figure 6.5(a) shows the dependence of V_ω with frequency. From Figure 6.5(a), a linear trend of $V_\omega(V_{ph})$ is observed up until 2.2 V, decreasing thereafter. We suppose that this dependency is the result of antenna frequency dependence and diode cutoff. The initial increase can be understood from the standpoint of the CNT antenna array. Prior work assumed R_A~100 Ω for the CNT nanoantenna, consistent with the literature [8, 9, 16, 24, 94]. Unlike bowtie antennas [11, 23, 25, 95], the CNT geometry is likely to function as a dipole antenna such that R_A is affected by the frequency. As discussed in Section 2.2, the radiation resistance of a dipole is classically related to frequency by $R_A(\omega) \propto \omega^2$[41]. Our definition of V_A in equation (6.1) therein suggests that the optical dipole antenna voltage scales approximately linearly with frequency.

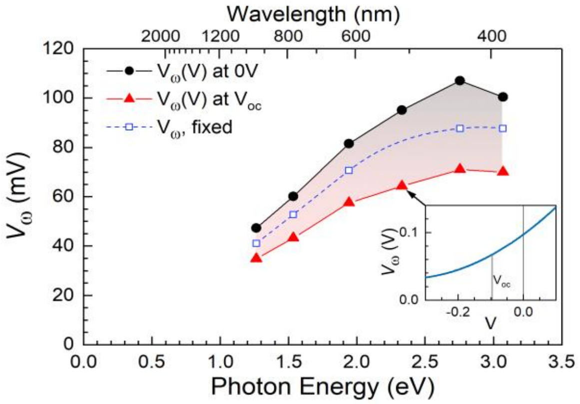

Figure 6.5. Frequency dependence of a.c. diode voltage, V_ω, determined by fitting the PAT model to optical *I*–*V* scans in either fixed V_ω (open markers) or V_ω(V) (closed markers). Inset represents $V_\omega(V)$ for 532 nm.

We also postulate that the diminishing V_ω at higher frequencies arises from antenna-diode coupling loss. As shown earlier in Chapter 2, there is coupling efficiency between the antenna and diode based on the impedance match and the RC response time of the diode. In this case we estimate $R_A \ll R_D$. It can then be shown that V_ω is related to V_A through

$$V_\omega(\omega) = \frac{V_A(\omega)}{(1 + (\omega R_A(\omega) C_D)^2)^{1/2}} = V_A(\omega) \cdot (\eta_{RC})^{1/2}. \tag{6.6}$$

Equation (6.6) conveys that $V_\omega(\omega) \sim V_A(\omega)$ for $\omega < \omega_c$, which means that the diode voltage is dominated by antenna behavior. It is noted that the frequency dependence attributed to the antenna also plays a role in η_{RC}. In the case of a dipole with $R_A(\omega) \propto \omega^2$, the cutoff frequency that shows up in η_{RC} is now $\omega_c(\omega) = \frac{1}{R_A(\omega) \cdot C_D}$. Now the frequency dependence can be extracted from R_A by introducing an equivalent cutoff frequency, ω_c^*, such that $\omega_c(\omega) = (\omega_c^\star)^3/\omega^2$. By expressing $\omega_c^\star$ this way, it retains the appropriate units and is necessarily independent of frequency. η_{RC} then becomes

$$\eta_{RC} = \frac{1}{\left(1 + \left(\frac{\omega}{\omega_c^\star}\right)^6\right)}. \tag{6.7}$$

This expression resembles the form of equation (2.12), giving $\eta_{RC}(\omega = \omega_c^\star) = \frac{1}{2}$ at the cutoff. The effect that the frequency dependent antenna has on η_{RC} is now clear via this equivalent cutoff frequency. The implication is that η_{RC}, and therefore V_ω, falls off much more sharply with frequency above the cutoff than would a constant antenna model.

Figure 6.6 shows equation (6.6) in relation to the values of $V_\omega(\omega)$ that were determined by earlier fitting of optical measurements. The model for V_ω matches well with data in the optical range. This provides convincing evidence of dipole behavior in the CNT nanoantennas. It is observed that at frequencies below 2 eV, V_ω is dominated by the frequency dependent antenna source voltage. The drop in V_ω afterwards marks the regime for RC roll off. From the data, we can infer an equivalent cutoff frequency of $\omega_c^\star$ = 785 THz (3.25 eV, 382 nm), denoting the point in which ½ of the power is delivered from the antenna to the diode.

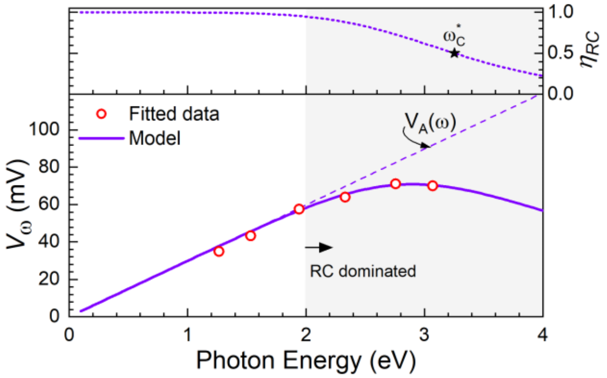

Figure 6.6. $V_\omega(V)$ is predicted using equation (6.6) in relation to values determined from the data. η_{RC} plays a role for V_{ph} > 2 eV. Cutoff frequency is estimated as $\omega_c^\star$ = 3.25 eV.

Now that we have a model of $V_\omega(\omega)$ across the entire optical range, we can simulate the PAT as a function of the photon energy using the curve from Figure 6.6. The resulting V_{oc} and I_{sc} are depicted in Figure 6.7. The PAT model has a maximum V_{oc} and I_{sc} occurring around 2.2 eV (563 nm). Because $V_\omega(\omega)$ was based upon actual illuminated tests, the simulated curve expectedly matches with the data points for V_{oc} and I_{sc}.

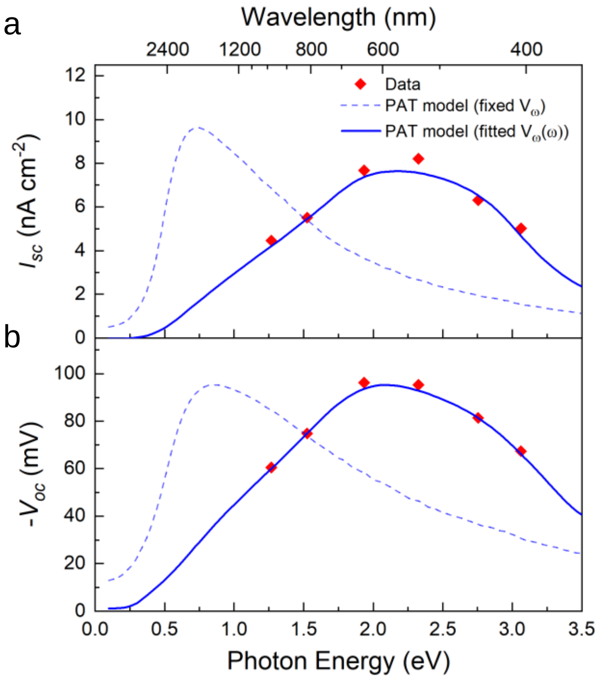

Figure 6.7. Comparison of PAT theory and measured (a) short-circuit current I_{sc} and (b) open-circuit voltage V_{oc}. The dashed line shows the PAT model with wavelength-independent V_ω (using the V_ω at 808 nm as an arbitrary reference).

It is also worth noting that the if the assumption for wavelength-dependent V_ω was not made, then PAT would instead predict a peak in the rectenna response occurring in the IR—around 0.8 eV (1550 nm)—with the photoresponse decreasing into the visible region. The CI^{4}M diode exhibits a secondary turn-on in the reverse bias direction which weakens the asymmetry, thereby reducing the net rectified photocurrent. The plot of $\mathcal{A}(V)$ from the dark *I*–*V* scans in Figure 5.4 reveals that the peak asymmetry occurs around ~0.8 V. Consequently, for incident light composed of photons with energy above 0.8 eV, photon-assisted electrons are rectified with diminishing efficiently. This observation underscores the importance of the diode *I*–*V* characteristics; in this case, a better rectenna can be realized by eliminating this unfavorable reverse bias current.

Because of the frequency dependence of V_ω, the photoresponse is shifted to higher photon energy. Indeed, the impact that $V_\omega(\omega)$ has on the system is apparent through the wavelength-dependent conversion efficiency shown in Figure 6.8. The peak predicted efficiency is $\eta = 3.2\times10^{-6}$ %, occurring at 2.2 eV ($\lambda = 564$ nm). This is fortunate for the potential use as a solar cell, as the majority of solar energy occurs falls below 800 nm.

As established earlier, the drop in efficiency at higher frequencies is due to the RC cutoff in the diode. η_{RC}, which was evaluated in Figure 6.6, is displayed atop the plot of η to illustrate this point—when the frequency of illumination exceeds $\omega_c^\star$ antenna-diode coupling efficiency deteriorates, leading to poor power transfer and an ultimate drop in the rectenna photoresponse. As such, the solution to improve the regime of efficient operation is striving to shift the cutoff frequency higher; this can be accomplished by lowering the diode capacitance. Further analysis and interpretation of the efficiency loss mechanism that have been prefaced here will be covered at the end of the chapter in Section 6.4.

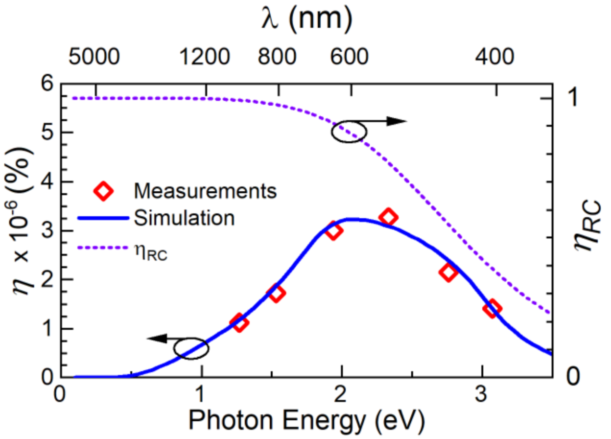

Figure 6.8. Conversion efficiency η versus incident photon energy. The RC cutoff efficiency η_{RC} is also shown to exemplify its effect on power conversion.

6.3.2 *Simulations of Optical Behavior at High Bias*

Here we explore the PAT simulated optical response at high bias (that is at biases approaching the measured limits). In Figure 6.9 the simulated *I*–*V* ($\lambda = 638$ nm) completely fails to match the measured optical response above $V \approx 0.2$ V. Considering the quantum regime approximation of PAT for $\alpha \ll 1$, the illuminated behavior far from zero bias approaches $I_L(V \gg 0) \approx J_0^2(\alpha) I_D(V)$ as $J_{|n|\geq 1}(\alpha \ll 1) \to 0$. Hence, the substantial increase in illuminated forward-bias current around 1 V is greatly underpredicted due to

$I_D(V)$. The PAT model thus fails to explain why such a significant enhancement in the forward current is observed under illumination.

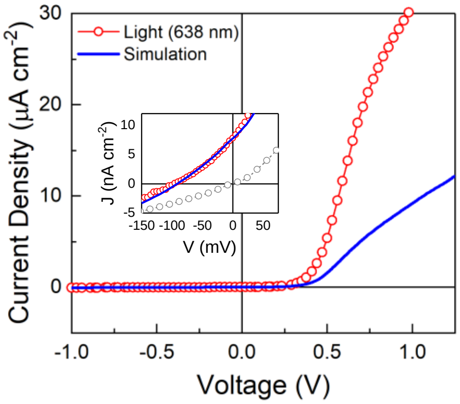

Figure 6.9. Simulated rectenna response over a large bias range of ±1 V (λ =638 nm). (Inset) second quadrant power generation. PAT drastically underpredicts the illuminated current ~1 V.

There are several hypotheses for the deviation from the model. First, this may be attributed to an erroneousness in the extrapolated section of the dark *I*–*V* at such high bias against the real diode curve (if, of course, this could be measured without reaching oxide breakdown).

Alternatively, it is very likely that the high-frequency properties of the diode (*i.e.* the dielectric layers) cause the real a.c. *I*–*V* ($I_D^{ac}(V)$) characteristics to deviate significantly from the measurable d.c. behavior $I_D^{dc}(V)$. The incorrect correspondence between d.c. and optical frequency rectifier characteristics was pointed out by Belkadi *et al*. [93]. They discussed that the potential drops across the tunneling barrier, specifically for a multi-insulator MIM, are governed by resistance voltage division at d.c. and capacitive voltage division at a.c. frequencies (Figure 6.10(a)). Hence, d.c. characteristics alone cannot be used to predict the optical frequency response. This finding is particularly critical for our CI^{4}M diode, suggesting that the PAT model is not suited for predicting the optical response at high bias when the deviation between $I_D^{dc}(V)$ and $I_D^{ac}(V)$ becomes significant.

In lieu of more rigorous treatment of the impedance-based voltage division that requires modeling the *I*–*V* tunneling characteristics from first principles, we estimate the effect of $I_D^{ac}(V)$ on PAT prediction by applying a simple scaling of $I_D^{dc}(V)$. The measured $I_D^{dc}(V)$ curve is scaled by a fixed value of γ such that $I_D^{ac}(V) = \gamma \cdot I_D^{dc}(V)$. This is a very rough, first order approximation analogous to the increased tunneling probability from that would result from changing the tunneling barrier. $I_D^{ac}(V)$ is then inserted into the PAT equation and using the same wavelength parameters as before, fitted to experimental $I_L(V)$ curves to determine γ. In the case of the data shown here, the best-fit value was $\gamma = 3.1$. Figure 6.10(b) shows that scaling the diode behavior, even simply scaling by a constant factor, significantly improved the agreement between the high-bias behavior of the PAT simulation and the measured optical response. It is worth emphasizing that this approximation is primarily to demonstrate one possible explanation as to the deviation in the PAT model at high bias. This initial agreement alludes to a discrepancy between the CI^{4}M measured d.c. characteristics and corresponding a.c. tunneling behavior that could primarily be based on optical frequency material properties. This is an interesting result that merits validation and further study.

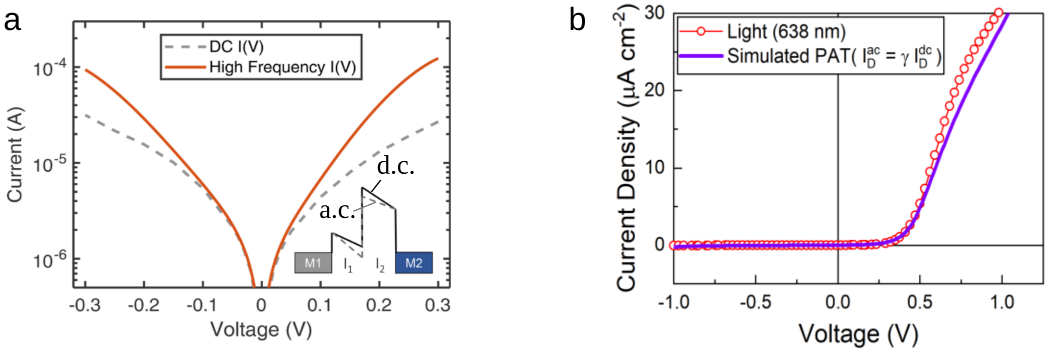

Figure 6.10. (a) Discrepancy between MIIM d.c. and a.c. *I*–*V* characteristics. Adapted with permission from [93]. (b) Simulated rectenna response assuming the high frequency diode current is scaled by a constant $\gamma = 3.1$.

6.3.3 Dependence on Illumination Power

Next, the effect of light intensity on rectenna response is investigated by simulating PAT through a range of incident laser powers according to equation (6.1). Fitting parameters that were determined earlier were implemented here for $\lambda = 638$ nm (1.94 eV). For estimating the PAT response over a range of incident powers, $V_\omega(V)$ was inserted into equation (6.1), taking advantage of the relation $V_\omega(V) \propto V_A \propto P_{in}^{1/2}$ and using a single fitted measurement as a baseline from which to scale the intensity.

Figure 6.11 shows I_{sc} and V_{oc} at 638 nm. There is excellent agreement between measurements and theory, even though only a single measurement was used to calibrate V_ω. Since the input power drives the optical voltage, greater laser intensity increases the rectified power generated in the second quadrant. The linear dependence between I_{sc} and incident power shown in Figure 6.11(a) further supports optical rectification, owing to the fact that rectified current should be proportional to power delivered to the diode [16]. This is also consistent with the enhanced photocurrent we observed in Figure 8.4(c) [20]. The short-circuit current response is 1.5 µA/W. V_{oc} approximately depends upon the square root of incident power. This V_{oc} relationship heuristically scales with the antenna voltage, $V_A \propto P_{in}^{1/2}$. In other words, higher light intensity results in increased field strength which drives an increased photovoltage.

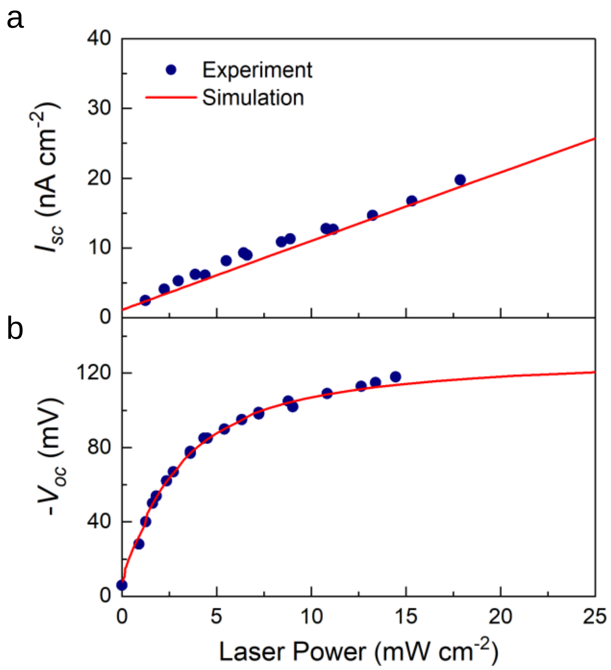

Figure 6.11. Laser power dependence on (a) I_{sc} and (b) V_{oc} for $\lambda = 638$ nm. Comparison of experimental data versus the PAT model.

For the simulated photoresponses depicted in Figure 6.11 the input power that is displayed is actually the P_{in} used for the PAT model but scaled up by a factor of 87 in order to coincide with the measured data. This is based on assuming $R_A = 100\ \Omega$. However, the fact that the model predicts the same optical response with a nearly two orders of magnitude lower input power than we experimentally measure suggests that the assumption for R_A could be incorrect. Otherwise, the deviation in simulated and experimental input powers can be explained through several loss mechanisms that are not accounted for in the present model. In other words, we may infer that a significant portion of the measured laser power is being in the various components of the device before contributing to PAT.

First, imperfect transmission through the top Al electrode could significantly lower the actual power that is available for absorption by the CNT nanoantennas, as explored in Section 5.3.2.2. The transmittance of 50 nm planar Al is $T_\lambda \sim 6$ % with slight wavelength dependence (Figure 5.9). This does not fully account for the estimated power loss. It might also be misleading to portray transmission losses from a planar metal layer to our metal-coated CNT forest. The metal layer on top of the array creates a metal mesh that likely allows light to be reflected off metal-coated CNT and deeper into the forest. In this scenario the actual effective transmittance to the CNTs could be much greater than 6 %.

Second, inefficiencies could be present in the antenna component. Losses could incur from antenna radiation efficiency, antenna propagation loss, or the coherence of the light. These loss mechanisms are difficult to quantify here, but could have extensively adverse effects on the device performance.

Based on PAT, efficiency can be improved by optimizing the diode voltage under constant a.c. power. This requires tuning the dark *I*–*V* to affect the semiclassical resistance. Engineering the diode *I*–*V* is perhaps the most direct route to better rectenna efficiency. Maximizing the diode conductivity generally leads to better response across the board. However, thinning the tunneling barrier to reduce diode resistance similarly increases leakage current [86]. Additionally, the effect of thinner insulator on capacitance and therefore the cutoff frequency cannot be neglected. Instead, implementing a multi-insulator laminate is a route to achieve high asymmetry with low turn-on voltage [96]. Suppressing the reverse bias current is important to minimize loss at high photon energy, whereas low turn-on enables efficient operation at lower photon energy, particularly when incident intensity is low enough to maintain quantum operation. Choosing electrodes that are more transparent yet conductive remains essential to mitigate optical and ohmic power losses. Lastly, better understanding of the CNT array as antenna elements is needed to optimize the optical voltage through antenna efficiency and radiation resistance.

6.4 Analysis of Efficiency Limitations

The total rectenna power conversion efficiency, η, is determined by several discrete factors affecting the system. We identify four primary loss mechanisms that impact η, be represented below as the product of these factors:

$$\eta = T_\lambda \, \eta_A \, \eta_{AD} \, \eta_{rect} \tag{6.8}$$

- T_λ is the wavelength-dependent transmission of the light through the upper material layers and into the CNT antenna array for absorption.

- η_A is the efficiency of the antenna. For simplicity, η_A includes the radiation collection efficiency of coupling the incident light to the antenna as well as the propagation of the received power to the antenna junction. The former is governed by the radiative properties of the antenna, such as bandwidth, as well as the coherence of the light source. The latter is affected by losses in the antenna, especially at high frequencies. This radiation efficiency from an imperfect conductor is $\eta_{rad} = \frac{R_{rad}}{R_{rad}+R_{loss}}$.

- η_{AD} is the coupling efficiency of a.c. power transferred from the antenna to the diode. This takes into account the impedances between the components as well as the response time of the diode to the particular a.c. frequency.

- η_{rect} is the efficiency of the diode in rectifying the a.c. signal into d.c. power. η_{rect} is related to the current responsivity of the diode, $\beta = \frac{1}{2} I''/I'$, which also describes the ratio between the d.c. current produced by the diode and the a.c. power into the diode. Accordingly, the efficiency of the diode is proportional to β by $\eta_{rect} \propto (\beta\, V_{bias})$. Importantly, the responsivity of the diode during optical rectification is governed by the semiclassical value, β^{sc}, when operating in the quantum regime. This involves calculating β^{sc} by finite difference differentiation and applying photon-assisted tunneling theory [35].

Presented in Section 2.1.1, the small-signal equivalent circuit for the rectenna shows that η_{AD}, the coupling efficiency between the antenna and diode elements, can be separated into two terms that describe the antenna-diode impedance matching and the cutoff frequency of the diode:

$$\eta_{imp} = \frac{4R_A\, R_D}{(R_A + R_D)^2} \tag{6.9}$$

$$\eta_{RC} = \frac{1}{1 + \left(\frac{\omega}{\omega_c}\right)^2}. \tag{6.10}$$

As mentioned in Section Chapter 6, there is an additional frequency dependence to equation (6.10) on behalf of the antenna, which manifests through $\omega_c(\omega) = \frac{1}{R_A(\omega)\cdot C_D}$. The implication is that the η_{RC} falls off at a steeper rate once the frequency of operation reaches the cutoff regime. It can be inferred from equation (6.8) that the actual power received by the diode is that which remains after the incident radiation experiences losses from transmission into the antenna array, antenna radiation effects, and the coupling from the antenna to the diode: $P_{in,diode} = T_\lambda\, \eta_A\, \eta_{AD} \times P_{incident}$.

In this section, the efficiency limits of the CNT rectenna is explored. The model of PAT developed earlier is assessed with hypothetical adjustments to the diode in order to guide future CNT rectenna device improvements.

6.4.1 Impact of Nonideal Diode I–V Characteristics

Here we examine the effects of diode ideality on power conversion. PAT simulations are generated using the same parameters for $V_\omega(V,\omega)$ as determined in Section Chapter 6. The $I_D(V)$ that are inserted into equation (6.3) are based upon the original CI^{4}M *I–V* scan, but systematically modified to study the effect of (1) reverse bias leakage and (2) diode conductivity on power conversion.

The 16 nm CI^{4}M diode exhibits a reverse bias turn-on around –0.8 V. This leakage current—and the associated reduction in tunneling asymmetry—manifests as progressively weaker rectifying ability for incident photons having energy above this turn-on voltage. As observed in Figure 6.12, there is a distinct improvement in rectified power as a result of suppressing this reverse bias current. The photon energy at which peak efficiency occurs is shifted slightly from 2.3 to 2.5 eV. Hence, efficiency can be doubled to 6×10^{-6} % by appropriate engineering of the tunneling barrier so as to reduce the leakage current.

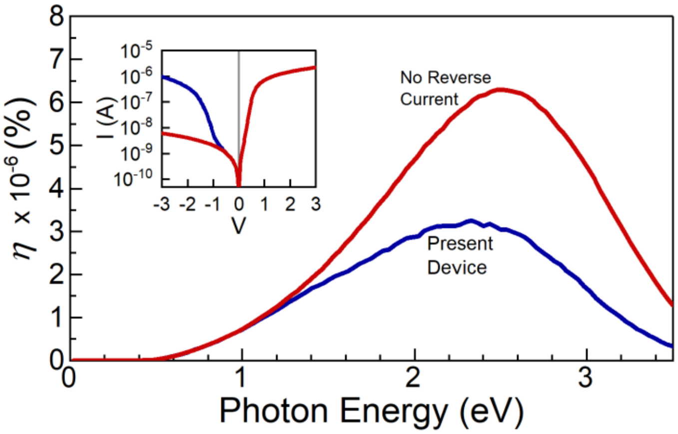

Figure 6.12. Effect of diode reverse bias. Inset shows dark *I–V* scans used for PAT simulations for present device and diode with suppressed reverse bias leakage current.

Next, the relationship between diode conductivity and rectification is assessed. PAT is modeled using the idealized diode (having negligible leakage current) and systematically scaling each $I_D(V)$ to higher currents. Figure 6.13 shows conversion efficiency as a function of diode conductivity (via 1 V current) for $\lambda = 532$ nm (2.3 eV). We find that η increases by about 10× for every corresponding 10-fold reduction in diode resistance. This rise in η can be attributed to increasing photocurrent responsivity, as I_{sc} is observed to be proportional to the diode conductivity. The implication is that drastic improvements in η can be attained by mitigating the diode resistance. This underscores the importance of a thin tunneling barrier on enhancing impedance match. Practical levels of rectified power can be attained with proper development of the CI^{4}M diode.

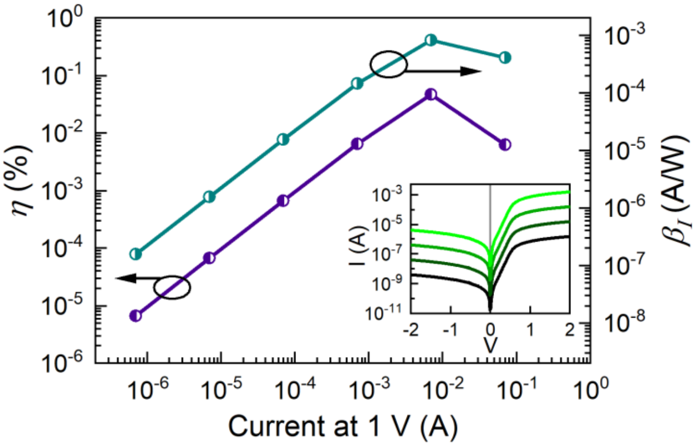

Figure 6.13. Effect of diode conductivity on conversion efficiency and photoresponsivity ($\lambda = 532$ nm). Inset displays the dark *I*–*V* scans used to simulate the PAT with progressively scaled conductivity.

6.4.2 *Impact of Cutoff Frequency*

Lastly, we analyze the impact of the rectifier response time on power conversion. Frequency-dependent rectification is simulated using the expression for $V_\omega(V, \omega)$ established in Section 6.3.1, while incorporating a variable cutoff frequency. As expected, η increases monotonically with $\omega_c^\star$ (Figure 6.14). In the case of the measured diode *I*–*V*, efficiency gradually tapers off with higher cutoff frequency, whereas the relationship is linear for a diode with no reverse current. The frequency at which maximum efficiency occurs is also proportional to $\omega_c^\star$, which is an expected result so long as we are able to maintain the assumption that the frequency response of the antenna is unchanged. Additional testing is needed to better understand the limits to the high frequency CNT nanoantenna behavior. If we desire the rectenna to operate in the visible region (down to ~400 nm) then visible-spectrum conversion efficiency of 8.2×10^{-6} % is predicted for $\omega_c^\star > 1$ PHz (4 eV).

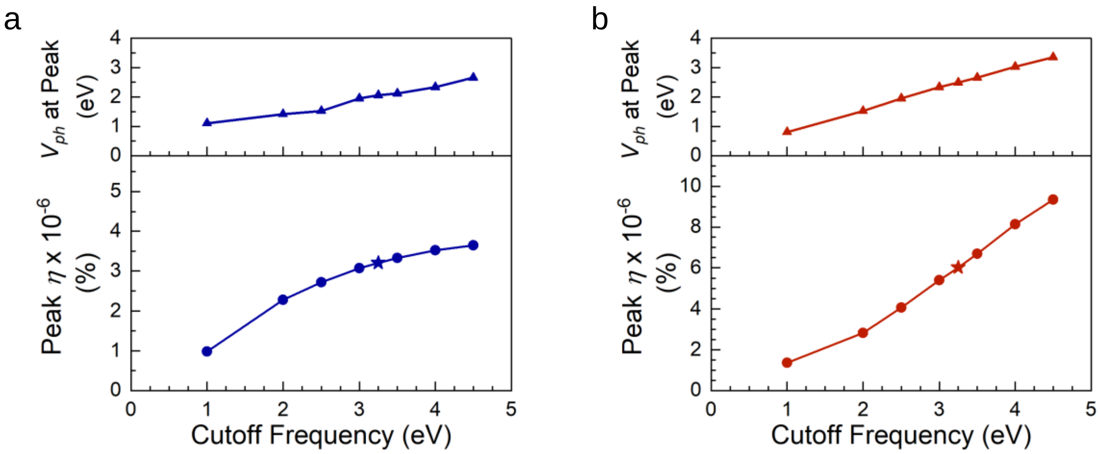

Figure 6.14. Peak simulated conversion efficiency as a function of diode cutoff frequency for (a) nonideal dark *I*–*V* scan and (b) idealized diode with suppressed leakage current, from Figure 6.12. The upper panels show the photon energy at which the peak occurs. Stars indicate existing estimated cutoff frequency $\hbar\omega_c^\star = 3.25$ eV.

6.4.3 Implications

The analysis of efficiency limitations arising from the CNT diode and in light of PAT theory indicates that rectenna conversion can be enhanced through various modifications of the diode. Under the right circumstances—a good diode with excellent asymmetry, a low turn-on voltage, and high conductivity matched to the antenna—we find that η can reach 0.1 %. Since this analysis does not explore improvements to other aspects of the rectenna such as maximizing electrode transparency and CNT light absorption, antenna radiation efficiency, and residual ohmic losses incurred throughout the device, even further efficiency could be possible.

The greatest progression of efficiency comes from increasing diode current. This can be achieved by engineering the diode structure with thinner barrier layers to leverage the exponential relationship with tunneling resistance. Attaining high efficiency will still be a challenge on account of conflicting properties. For instance, lowering diode resistance to enhance the impedance match will eventually have a deleterious effect via the cutoff frequency since $C_D \propto d^{-1}$. Fabrication challenges also arise when the insulator is made too thin, as has been discussed throughout Chapter 3. It has been observed that capacitance plays a more subdued role on efficiency than diode resistance. Therefore, some increase in capacitance is permissible especially if the application does not call for a high cutoff point.

6.5 Summary

In light of illumination measurements, a model of PAT theory has been developed to elucidate the rectification mechanism in a robust and high performance CI^{4}M diode. The simulated *I–V* curves are in excellent agreement with optical measurements. Simulated behavior across the full optical spectrum underscores frequency-dependent mechanisms that are proposed as artifacts of spectral antenna dependence or limited device bandwidth associated with an optical cutoff frequency. In the case of cutoff frequency we estimate $\omega_c \sim 780\,\mathrm{THz}\ (3.25\,\mathrm{eV},\ 381\,\mathrm{nm})$. We use the model to assess efficiency limits and prioritize areas of improvement for future generations of devices: lowering device resistance directly translates to efficiency, while lowering capacitance through the dielectric thickness and ε will shift the operating regime to higher frequencies.

Questions still remain after these optical rectification results. Further refinement of the rectenna model is needed to understand and accurately depict operation of the CNT antenna at optical frequencies and any frequency dependence therein. Addition evidence proving the CNT optical antenna behavior is merited. This includes substantiating the antenna length effect, which is difficult to accurately control due to fabrication limitations that create significant nonuniformity in the CNT lengths over large arrays. Additional new materials should also be explored in order to achieve the enhanced device properties suggested during the PAT efficiency analysis. Special interest is directed to exploring better top electrode materials which could offer improved optical transparency and conductivity. Several of these issues are being addressed presently through a modification of the CNT device construction—a planar structure that offers potential for better control of the CNT array dimensions, and allows for more diverse materials incorporation. This novel concept is presented in Chapter 8.

CHAPTER 7. BROADBAND OPTICAL RECTIFICATION

7.1 Motivation

Researchers have theorized that rectenna power conversion efficiency for monochromatic light can approach nearly 100 %, while for multispectral solar conversion 44 % is possible at terrestrial intensity [5]. The present optical conversion efficiency of the CNT rectenna still remains low at around 10^{-5} % for monochromatic frequencies [86]. Moreover, for broadband solar and thermal applications a rectenna should be capable of efficiently rectifying multispectral radiation. Thus, this chapter seeks to progress our understanding of the broadband optical conversion mechanism in CNT rectennas by exploring dichromatic photoresponse. The response of the CNT rectenna is examined under dual-wavelength illumination and modeled using dichromatic PAT theory.

7.2 Dual-Wavelength Rectification

7.2.1 Dichromatic Photon Assisted Tunneling Theory

To further understand the rectification mechanism of the solar spectrum, we consider the photon-assisted transport of electrons simultaneously illuminated by two frequencies, ω_1 and ω_2. The time-dependent voltage across the diode junction is expanded from the earlier monochromatic model to include the two discrete a.c. voltage terms: $v_D(t) = V + V_{\omega_1}\cos(\omega_1 t) + V_{\omega_2}\cos(\omega_2 t)$. Based on the Tien Gordon approach and the description by Tucker [73, 78], equation (6.2) can be extended to model PAT of dichromatic illumination by [5]

$$I_L = \sum_{m=-\infty}^{\infty} \sum_{n=-\infty}^{\infty} J_n^2\left(\frac{eV_{\omega_1}}{\hbar\omega_1}\right) J_m^2\left(\frac{eV_{\omega_2}}{\hbar\omega_2}\right) \times I_D\left(V + n\frac{\hbar\omega_1}{e} + m\frac{\hbar\omega_2}{e}\right) \tag{7.1}$$

$$= \sum_{m=-\infty}^{\infty} \sum_{n=-\infty}^{\infty} J_n^2(\alpha_1)\, J_m^2(\alpha_2) \times I_D\left(V + nV_{ph_1} + mV_{ph_2}\right).$$

In equation (7.1) the current is now subjected to simultaneous emission and absorption of photons at both energies, $\hbar\omega_1$ and $\hbar\omega_2$. Interestingly, this gives rise to potential frequency mixing. Under dichromatic illumination we can get current contributions that are shifted by either the sum or difference in energy states: e.g. $\hbar(\omega_1 \pm \omega_2)$, rather than sole integer multiples as the case for monochromatic light.

The other implication of the expanded dichromatic PAT equation is the introduction of a second a.c. voltage. Now both V_{ω_1} and V_{ω_2} must be found. In this dichromatic analysis, we will determine V_{ω_1} and V_{ω_2} separately from fitting of monochromatic measurements, and then combine them in equation (7.1) to model the dichromatic behavior.

7.2.2 Methods

This study of dichromatic rectenna response will include illumination measurements in combination with the model for PAT theory. The device is the same quad-insulator structure studied in Chapter 5: CNT/Al_2O_3-ZrO_2-Al_2O_3-ZrO_2 (4/4/4/4 nm)/Al. Dark *I–V* scans are depicted in Figure 7.1(a). Devices exhibit repeatable *I–V* scans (Keithley 2450) and exhibit good nonlinearity, $\mathcal{A} > 100$, and low turn-on voltage ~0.3 V.

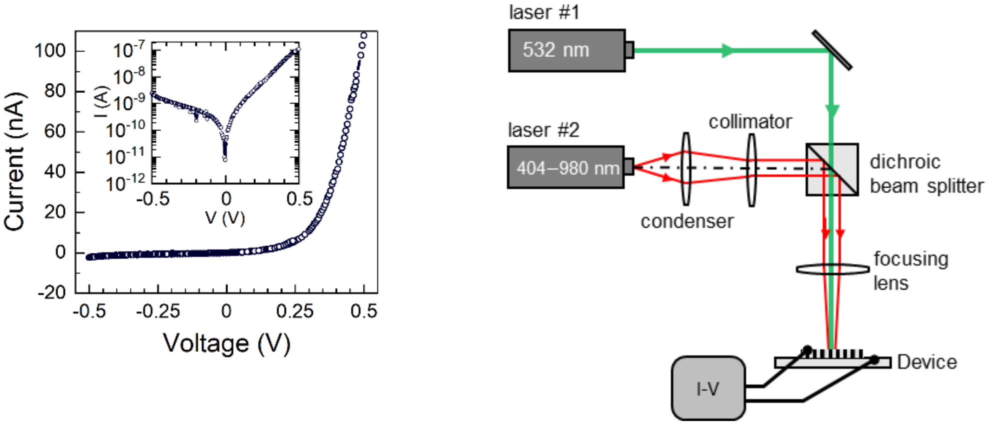

Figure 7.1. (a) Dark *I–V* curve of the diode. (b) Schematic of the experimental setup. The sample is irradiated with one of three interchangeable, variable power diode lasers (404 nm, 638 nm, 980 nm) along with a 532 nm laser.

The experimental setup for optical testing is depicted in Figure 7.1(b). Dual-wavelength measurements are performed with a Scorpius 532 nm laser (laser #1) along with one of three interchangeable diode lasers (laser #2: 404 nm, 638 nm, or 980 nm). Preliminary monochromatic *I*–*V* measurements were taken by each laser as a function of incident power. Dichromatic experiments were conducted by combining both lasers #1 and #2 through a wavelength-suitable dichroic beam splitter (Thorlabs DMLP567 for long-pass filtering or DMSP505 for short-pass filtering). In a typical dichromatic measurement, the power of laser #2 was varied (Thorlabs LDC24C controller) while the power of the 532 nm laser remained fixed.

In simulating the dichromatic PAT behavior, we first determine the value of V_ω for each wavelength, as conducted in Chapter 5. The monochromatic PAT model was fit to illumination *I*–*V* scans by feeding in the measured dark *I*–*V* characteristics. V_ω was determined for each tested wavelength and as a function of laser power. A comparison of the fitted model to experimental monochromatic data is shown in Figure 7.2. At laser intensity of 5 mW/cm^2, the values of V_ω that were inferred from fitting are 107 mV, 93 mV, 69 mV, and 33 mV for lasers with $\lambda = 404$ nm, 532 nm, 638 nm, and 980 nm, respectively. Finally, the dichromatic behavior was simulated with equation (7.1) by feeding in V_{ω_1} and V_{ω_2} for the desired wavelengths and scaling to laser power.

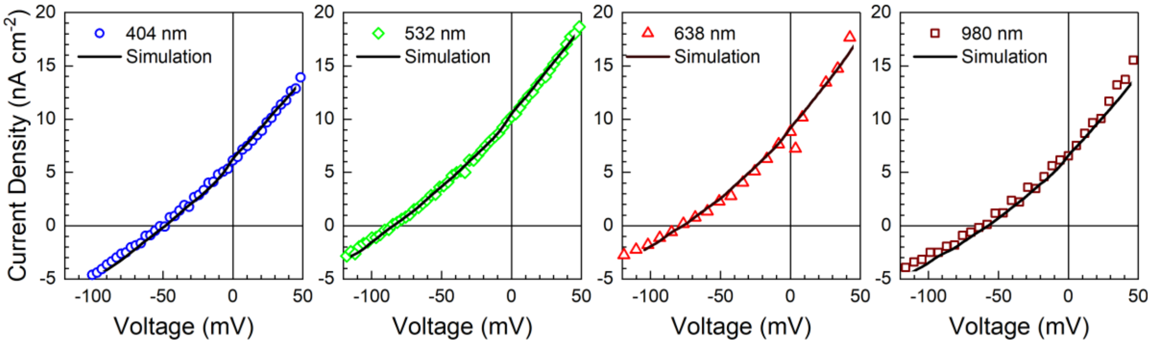

Figure 7.2. Simulated *I*–*V* curves fit to monochromatic data to determine $V_\omega(\lambda)$. Incident power is 5 mW/cm^2.

7.2.3 *Results*

A comparison of the two-frequency illuminated *I*–*V* scans with PAT theory are presented in Figure 7.3. These simulated PAT responses are in excellent agreement with measured dual-wavelength results. Simulations are also robust for multiple frequencies, therefore enabling estimation of the dichromatic rectenna response through calibration to the individual monochromatic responses. The first observation from Figure 6.2 is that the dual-wavelength response is not a superposition of the single-wavelength curves. This result is an artifact of the dichromatic PAT mechanism. For the 404/532 nm and 980/532 nm tests, the dichromatic *I*–*V* curves have a somewhat shallower slope than the individual single-wavelength scans. This is interesting—the reduction in slope for comparable powers has previously been suspected to be a result of multispectral frequency mixing. Meanwhile, the 638/532 nm test showed an increased slope. This could be because the frequencies of the two beams are similar enough ($\Delta\hbar\omega \sim 0.38$ eV) that mixing effects are weak, and thus the response is the approximate result of monochromatic PAT occurring at the total cumulative power. The implications of this wavelength-dependent dichromatic response will be further explored.

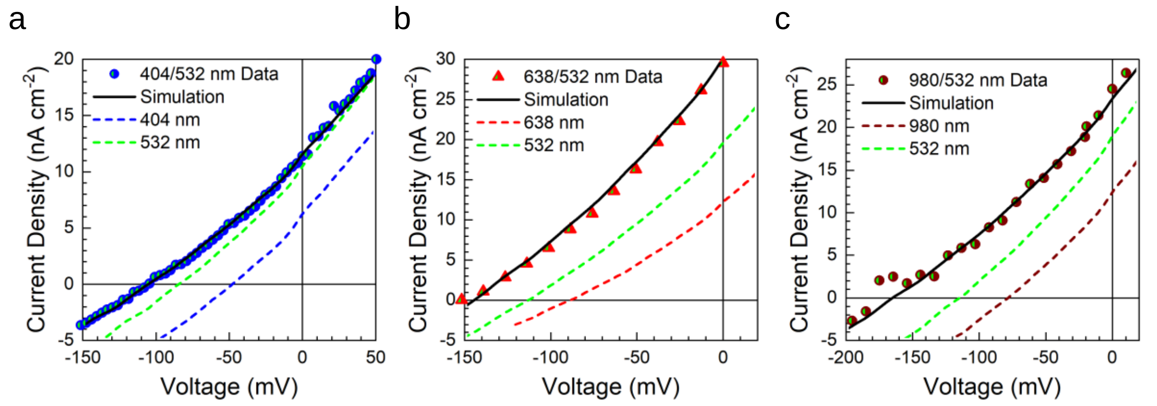

Figure 7.3. Comparison of dual-wavelength *I*–*V* and dichromatic model: (a) 404/532 nm each at 5 mW/cm^2, (b) 638/532 nm each at 8 mW/cm^2, (c) 980/532 nm each at 10 mW/cm^2.

Dual-wavelength optical rectification is investigated with measurements of photocurrent versus incident laser power. In Figure 7.4 we see the expected increase of I_{sc} with P_{in}. Comparing calculations of dichromatic PAT theory to measurements shows that both results superimpose each other with excellent agreement over all three combinations of wavelengths. The highlight of these findings is the accuracy with which dichromatic PAT theory agrees with measurements based only on the knowledge of monochromatic responses.

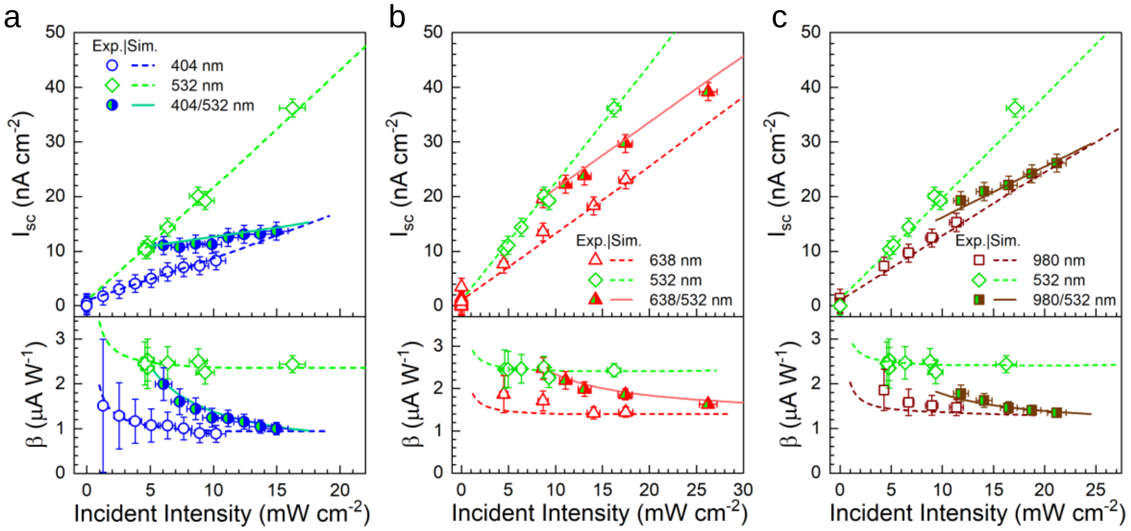

Figure 7.4. Short-circuit photocurrent I_{sc} and photoresponsivity β plotted as a function of total incident laser power $(P_1 + P_2)$ for single and dual-wavelength illumination: (a) 532 and 404 nm, (b) 532 and 638 nm, (c) 532 and 980 nm. In dual-wavelength measurements the 532 nm laser power is kept constant while the other laser power is varied. Curves show PAT simulations, exhibiting excellent agreement to experimental data.

The photoresponsivity, β, for each single-wavelength test is 0.96, 2.4, 1.4, and 1.3 µA/W for 404, 532, 638, and 980 nm, respectively. For dual-wavelength illumination I_{sc} is in between the values of I_{sc} for each single-wavelength case, as could be expected. Interestingly, the slope of I_{sc} is lower than for either single-wavelength response. In other words, the dichromatic behavior is not a superposition of each monochromatic response

For two lasers the total photoresponsivity $\beta = \frac{I_{sc}}{P_{in}} = \frac{I_{sc}}{P_1+P_2}$ is based on the total incident power of the 532 nm laser #1 plus laser #2. As P_2 is increased outward from zero, β is seen to gradually shift from the photoresponsivity of 532 nm down to that of the second laser once P_2 becomes severalfold higher than P_1. It is suspected that the reduction in the responsivity is due to frequency mixing, where the dichromatic PAT model introduces

$\hbar(\omega_1 \pm \omega_2)$ terms that cause the overall optical rectification process to transcend the simpler combination of individual single-wavelength responses. This is evident in the reduced slope of I_{sc} with respect to total incident power. The agreement between the measurements and simulated PAT behavior supports this notion. If we scrutinize equation (7.1) and assume operation approximately in the quantum regime ($\alpha_1, \alpha_2 < 1$), then the resulting optical response can be expanded to the first several terms:

$$\begin{aligned} I_L(V) \approx J_0^2(\alpha_1)J_0^2(\alpha_2) \cdot \left[I_{0,0}\right] + J_1^2(\alpha_1)J_0^2(\alpha_2) \cdot \left[I_{1,0} + I_{-1,0}\right] \\ +J_0^2(\alpha_1)J_1^2(\alpha_2) \cdot \left[I_{0,1} + I_{0,-1}\right] + J_1^2(\alpha_1)J_1^2(\alpha_2) \cdot \left[I_{1,1} + I_{1,-1} + I_{-1,1} + I_{-1,-1}\right] \\ +J_2^2(\alpha_1)J_0^2(\alpha_2) \cdot \left[I_{2,0} + I_{-2,0}\right] + J_0^2(\alpha_1)J_2^2(\alpha_2) \cdot \left[I_{0,2} + I_{0,-2}\right] \end{aligned} \tag{7.2}$$

where the concise indexed notation $I_{n,m} = I_D\left(V + nV_{ph,1} + mV_{ph,2}\right)$ is used to represent the shifted diode curves. Assuming α_1 and α_2 are on the same order, it can be shown that the $J_0^2\, J_{\pm 2}^2$ Bessel function terms fall off much more rapidly than the terms for $J_{\pm 1}^2\, J_{\pm 1}^2$. In other words, the first order mixing terms for $\hbar(\omega_1 \pm \omega_2)$ dominate the second order single-frequency terms. Second, if we want to look at the very first $(n, m) = (0,0), (\pm 1,0), (0, \pm 1)$ terms, we could consider the case if photon energy is high enough ($\alpha_1, \alpha_2 \ll 1$) such that all higher order terms are negligible. With this approximation the $\hbar(\omega_1 \pm \omega_2)$ mixing terms are removed. Evaluating the photoresponse at short-circuit, where $I_{0,0}(0V)$ drops out, leads to the simplified expression

$$\begin{aligned} I_{sc} = I_L(0) = J_0^2(\alpha_2)\left\{J_1^2(\alpha_1)\left[I_{1,0} + I_{-1,0}\right]\right\} \\ +J_0^2(\alpha_1)\left\{J_1^2(\alpha_2)\left[I_{0,1} + I_{0,-1}\right]\right\}. \end{aligned} \tag{7.3}$$

It should be noticed that the terms within the curly brackets are identical to the monochromatic photocurrents for the quantum regime. Therefore, equation (7.3) makes it clear that the quantum-regime approximation for dichromatic rectification at zero bias is equivalent to the sum of each monochromatic photocurrent scaled by a $J_o^2(\alpha)$ belonging to the other frequency. This insight helps qualitatively illuminate the reduced responsivity that was observed.

In conclusion, we find that the dichromatic experiments with CNT optical rectennas are in agreement with PAT theory. The predictive model can robustly predict the multispectral behavior based on inferred monochromatic response. It is apparent that simultaneous illumination by two frequencies of light has a weaker total photoresponse than a simple superposition of single wavelength behavior due with evidence pointing to frequency mixing effects. The implication of this finding is that polychromatic responsivity can be improved through spectral splitting into isolated rectenna devices. In the case of 404/532 nm with 1:1 intensity, the net responsivity from spectral splitting could be improved from 1.3 to 1.7 µA/W, marking ~30 % increase.

7.3 Broadband Solar Rectification

Joshi and Moddel applied PAT to calculate the efficiency limits of broadband solar rectenna to show that due to finite spatial coherence of sunlight the power conversion efficiency solar rectenna is limited to the Trivich-Flinn limit of 44 % for quantum processes [97]. Rectenna can, however, exceed this limit if they operate in the classical regime. Simulations by Joshi and Moddel for an ideal diode impedance matched to a 100 Ω antenna showed peak broadband efficiency could increase to 60 % as the optical response was shifted from the quantum regime to classical regime of operation [6].

About 60 % of solar energy falls within wavelengths <800 nm. The current CNT rectenna design are especially suited for solar conversion as they exhibit peak spectral efficiency that falls within this region of prime solar intensity. We are therefore interested in exploring the solar spectrum harvesting capabilities of this CNT rectenna. In this section, air stable devices are tested outside under direct sunlight and real-world conditions to demonstrate solar conversion capability.

7.3.1 Methods

Figure 7.5 shows the experimental setup for the CNT rectenna solar cell tested under sunlight. The CNT rectenna cell that was tested was a CNT/Al_2O_3-ZrO_2-Al_2O_3-ZrO_2/Al structure. The sample was mounted to a fixed plate with electrical connections leading to a Keithley 2450 d.c. source meter. A power meter was used to record the real-time solar intensity over the course of several hours. The solar intensity varied between 10 and 80 mW/cm^2 over time with relatively uniform mild cloud coverage. Several dark *I*–*V* scans were recorded throughout testing to confirm consistent diode behavior. This was conducted by shielding the sample from the sunlight with an opaque box.

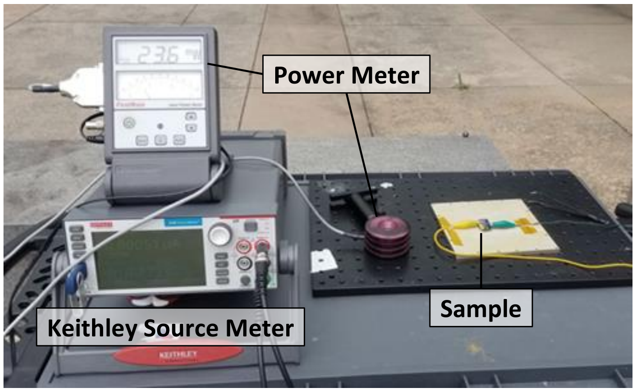

Figure 7.5. Experimental setup for direct conversion of sunlight.

7.3.2 Results

Figure 7.6(a) shows the illuminated *I–V* scans of the device under sunlight. At solar intensity of 20 mW/cm^2 $V_{oc} = -94$ mV and $I_{sc} = 1.6$ nA. Solar power conversion efficiency at maximum power point is η = 2×10^{-6} %. Furthermore, I_{sc} measurements taken over time with varied incident solar intensity show an average photocurrent responsivity of $\beta_I = 0.65$ µA/W (Figure 7.6(b)). To the best of our knowledge, this is the first report of rectification of sunlight in air. These results are encouraging as they mark another step towards implementing CNT optical rectennas in real-world technologies.

The solar conversion efficiency is severalfold lower than the conversion efficiency measured for monochromatic light. Most of the disparity arises from diminished β_I and not the β_V, which is similar to the monochromatic voltage responsivity shown in Figure 6.11 for the specified power. A similar result was made by Sharma *et al.*, in which they observed a V_{oc} that was comparable to monochromatic measurements while the solar spectrum photocurrent was substantially lower despite similar incident power. They initially attributed this to frequency mixing and broadband PAT effects. Now, the simulations of dichromatic rectification described in Section 7.2, along with the solar measurements, bolster this notion.

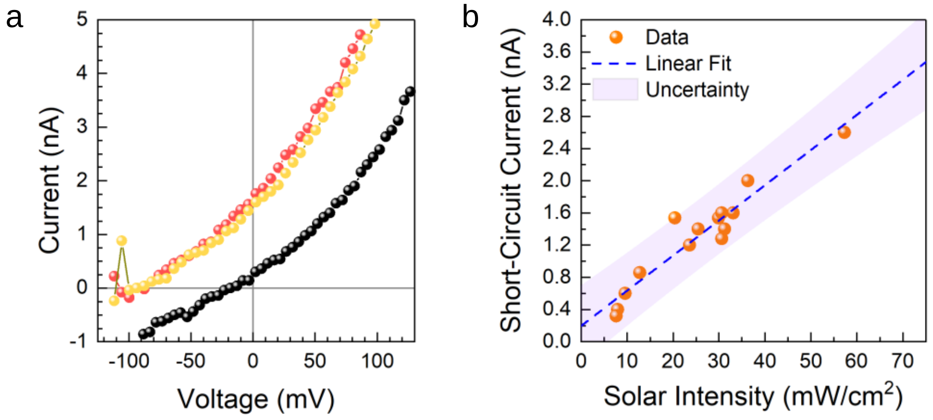

Figure 7.6. Solar rectification measurements. (a) *I*–*V* characteristics under 20 mW/cm^2 power and (b) short-circuit photocurrent function of intensity.

Solar photocurrent responsivity is even lower than that described in the dichromatic experiments, suggesting that an appreciable portion of the solar spectrum is being inefficiently converted. The likelihood that spectral mixing effects diminish the overall power conversion is a challenge for improving efficiency. For solar rectennas, it has been proposed that efficiency can be improved through the use of spectral splitting to isolate the different spectrums while operating each rectenna cell at a different voltage to capture the ideal, wavelength-dependent maximum power point [12]. Furthermore, as discussed in Section 6.4, the majority of the efficiency loss in this structure arises from high diode resistance causing poor impedance matching. Although this CI^{4}M structure is robust enough to demonstrate robust solar conversion in air, the 16 nm dielectric structure is too thick to give practical currents. Further optimization of the diode structure to maximize diode figures of merit and device reliability is needed. Even though efficiency is currently low, the high solar voltage responsivity gives these CNT rectenna devices potential as a broadband photodetector. Specific detectivity is calculated by recalling equations (5.1) and (5.2). Around zero bias, solar detectivity is $D^{\star} \sim 2\times10^{7}$ cm Hz$^{1/2}$/W.

Much more work remains to improve these CNT rectennas for efficiency solar conversion, including developing low-cost and large-scale fabrication methods to accelerate commercial application of this technology.

CHAPTER 8. PLANARIZED DIODE ARRAYS BASED ON INFILTRATED CNT FORESTS

8.1 Motivation

This chapter discusses polymer infiltrated forests to produce a novel planarized CNT tunneling diode for optical rectification. Incorporating polymer infiltration is motivated by two aims: *performance improvement* and *commercialization potential*. There are several specific objectives that are sought for these aims: planarization, isolation, and scalability.

The issue arising from using a bare CNT array is that metal electrodes deposited on the surface do not form a uniform, planar layer, but a mesh of metal-coated CNTs. This means the diode is not the idealized planar structure that is often depicted, leading to debate as to whether the diode is precisely determined by the CNT tip area, or whether any portion of the CNT length affects the diode conduction and capacitance. Embedding the CNTs with a medium is desirable to isolate the tips from the bulk forest, such that better control of the diode junctions can be realized.

Encapsulating the CNTs with an insulating medium also reveals more fabrication processes and enhances our materials selection. Insulating the CNT bulk enables solution-processable materials to be used without encountering problems with a free array, such as electrical shorting through the base electrode or CNT capillary bundling. Novel, solution-processable electrode materials such as the conductive and transparent PEDOT:PSS (Poly(3,4-ethylenedioxythiophene):poly(4-styrenesulfonate), or Ag nanowires, are attractive. Not only could these materials offer performance improvements, they lend themselves to scalability. For instance, these materials can be deposited by inkjet printing atop a planarized CNT surface.

For practical application of the CNT rectenna to compete with existing PV and photodetection technologies, devices need to leverage other advantageous features, such as inexpensive materials and low weight. The CNT forest is already an incredibly light weight material on its own. There is need to develop CNT rectennas that move past the use of expensive and bulky, silicon substrates so as maximize sample cost and power-to-weight ratio. A polymer substrate or encapsulation medium is one route to bypass silicon.

A commercial advantage of a polymer–CNT composite is mechanical flexibility, which is can be useful for novel applications that desire a device that can conform to an atypically surface geometry. CNTs are typically grown on rigid substrates using high temperature (>500 °C) processes that are incompatible with most flexible substrate materials. There are several methods of transferring as-grown CNTs from rigid wafers onto a more flexible substrate. A simple alternative method is to infiltrate the CNT forest with a medium that can be processed in solution and is flexible when cured, such that the infiltrated forest can be peeled off the growth substrate.

This chapter discussed a highly scalable approach to planarizing VACNT arrays using polymer infiltration and lift-off. Several alternative attempts were made to planarize the CNT arrays that included infiltrating the array with thick ALD insulator coating; and dip coating, drop casting or wicking polymers. These are mentioned in Appendix D.

8.2 Polymer-Based Carbon Nanotube Rectenna

Contemporary optoelectronic technologies are leaning on low-cost and high-performance solutions to cover a broad range of high frequency applications [2, 4, 11, 14, 22, 98–104]. Polymer-based MIM diodes are of particular interest for novel optoelectronic applications, promising advantages such as flexibility, light weight, transparency in the visible range, and low cost and scalable processing techniques [105–107]. Despite the progress that has been made lately on MIM diodes [53, 56, 63, 65, 81, 108, 109], few reports incorporate either polymer materials or fabrication on flexible substrates. Though some groups that have demonstrated the potential of flexible tunneling diodes used structures including Ti-TiO_2-Pd or Ni-NiO-Mo fabricated on polyether ether ketone [110], and Ti/OTS/Pt on polyimide [111].

For flexible optoelectronics, CNTs can be easily integrated with a number of polymers to produce composites with multifunctional and unique mechanical, electrical, and optical properties [105, 112, 113]. Embedding aligned carbon nanotubes with polymers is a facile way of producing highly oriented nanocomposites. In this section, a flexible polymer–VACNT composite is developed on which CNT–insulator–metal diode arrays are fabricated [8, 86], depicted in Figure 8.1. VACNT arrays are infiltrated with PDMS or epoxy media to planarize the surface of the CNT forest and isolate CNT tips from the bulk lengths. We then fabricate the tunneling diodes at the CNT tips on top of the planarized surface. This infiltration approach allows use of solution based PEDOT:PSS as an optically transparent electrode. Diodes are fabricated using insulator combinations of Al_2O_3 and HfO_2 and tested to optimize the diode electrical performance, device production yield, and stability. Through illumination testing, we show that these devices can rectify visible light, which demonstrates their potential as a flexible photodetector.

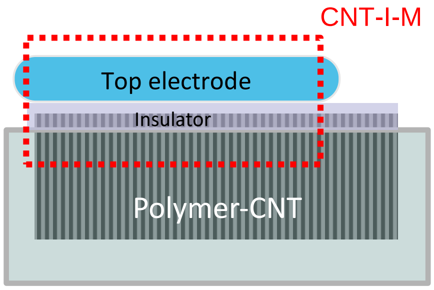

Figure 8.1. Depiction of a planar CIM diode array formed at the surface of polymer infiltrated CNT composite.

8.2.1 *Materials Selection*

This novel CNT device structure requires specific properties of the infiltration medium in addition to the top electrode. The properties desired for each component of the structure are outlined below:

Infiltration Medium: To create a planar array that isolates the CNT tips from the underlying forest, the medium must be an good electrical insulator. The material must also be solution processable to ensure good embedding within the array, as well as lending itself to facile fabrication and commercialization potential. Application-specific transparency is expected to assist with the absorption of light deep into the CNT array. Lastly, a flexible material is also desirable, and would open up the structure to more robust applications.

Top Electrode: The upper electrode material must be highly conductive as well as transparent to transmit light into the CNT array. Air stability is desirable to maintain testable devices in atmospheric conditions. Since this the electrode needs to be deposited on top of a planarized surface, patterning the device is possible. A solution-based material is desirable for ease of fabrication.

In this work, electrically insulating polymers have been investigated as the infiltration media. Polydimethylsiloxane (PDMS) is commonly used for embedding nanostructures because of its transparency, flexibility, and ease of processing [113, 114]. It is also chemical stable, inexpensive, and light weight, which is an advantage for large-scale device manufacturing. Epoxy resin is another common thermosetting polymer that has been used in a variety of applications—including VACNT composites— owing to its stability, chemical resistance, high adhesion, high strength, and minimal shrinkage upon cure. Most epoxies have low viscosity that fosters VACNT infiltration [112, 115]. Since both epoxy and PDMS can be solution cast, they are favorable materials for ease of processing that is desired for this study. As these materials are intended for rectenna applications, the optical transparency of the polymers was confirmed by measuring the transmission spectrum using UV-vis spectroscopy (Thermo Scientific Evolution 220). Samples of PDMS and epoxy, both 3 mm thick, were created using the methods described in the next section. Figure 8.2(a) confirms that PDMS is 70–75 % transparent down to 300 nm while the epoxy sample was nearly 80–90 % transparent above 450 nm. These results confirm the use of the polymers as CNT infiltration media to ensure transmission of light into the embedded forest.

Several choices of electrodes were considered, including ITO, PEDOT:PSS, and evaporated Ag (50 nm). Each material is electrically conductive. The optical transmission of each material deposited on a glass slide is shown in Figure 8.2(b). 50 nm of Ag has expectedly poor transparency in the visible and NIR, though has a spike in transmission in around <450 nm, which makes it a candidate for potential UV detection. ITO and drop cast PEDOT:PSS both exhibit excellent transparency in the range of 400–1100 nm. Because of the ease of processing in solution, PEDOT:PSS will be the top electrode material of focus in this work.

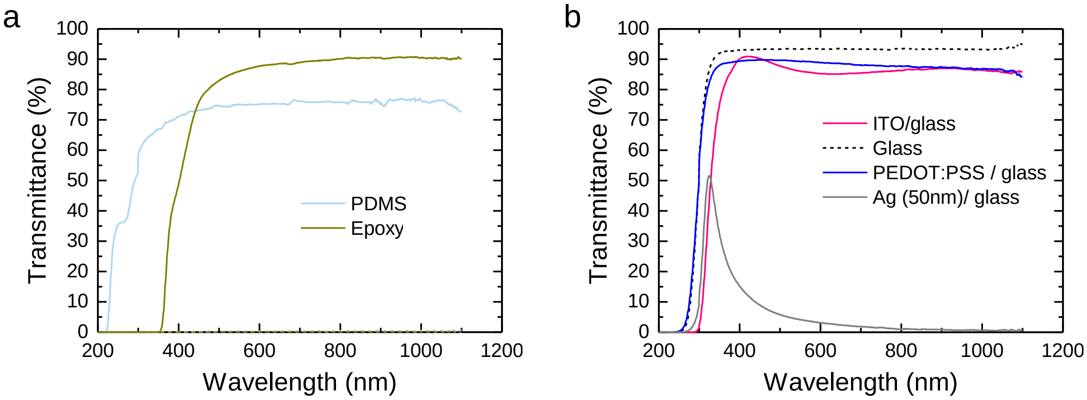

Figure 8.2. Spectral transmissivity of (a) PDMS and epoxy polymer media and (b) various electrode materials deposited on glass.

8.3 Methods

The fabrication of polymer-based VACNT tunneling diodes involves the following steps: (i) infiltration of a VACNT forest with polymer, (ii) removal of the embedded array from the substrate, (iii) preparation of the surface and exposed CNT tips, (iv) deposition of the oxide layer, and (v) deposition of the top electrode. We used CNTs grown on metal foil to demonstrate the capabilities of this approach for large scale manufacturing. The schematic in Figure 8.3 illustrates these steps, which are detailed in the following sections.

8.3.1 Sample Infiltration and Nanocomposite Formation

Multiwall VACNT forests on metal foil were obtained from Carbice Corporation (~20 nm diameter, 10 µm length). The multiwall CNTs were metallic and well-aligned. Two different polymer materials, PDMS or epoxy, were explored as infiltration media, with their methods of polymer preparation and VACNT infiltration described herein.

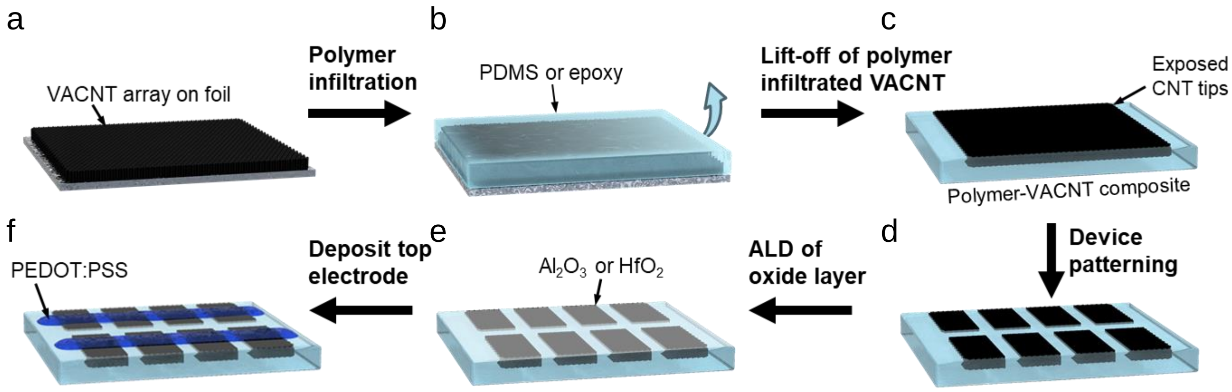

Figure 8.3. Schematic of infiltration approach and diode fabrication. (a) VACNT array on foil. (b) VACNT infiltrated with PDMS or epoxy. (c) Polymer infiltrated VACNT removed from foil and (d) patterned. (e) Atomic layer deposition of dielectric insulator. (f) Drop casting of PEDOT:PSS top electrode.

For PDMS embedding, silicone elastomer base and curing agent (Sylgard 184, Dow Corning) were mixed in a standard 10:1 weight ratio then degassed to remove air bubbles. To infiltrate the VACNT array, PDMS was poured directly onto the VACNT forest and remaining air bubbles trapped in the array were removed under vacuum. The sample was then cured at 125°C for 1 hr.

Alternatively, for epoxy infiltration, EMbed 812 (Electron Microscopy Sciences) was prepared according to manufacturer's directions. Epoxy resin base, dodecenyl succinic anhydride (DDSA), methyl-5-norbornene-2,3-dicarboxylic anhydride (NMA), and 2,4,6-tris(dimethylaminomethyl)-phenol (DMP-30) accelerant were combined in a volumetric ratio of 20:22:5:1. The resin and anhydrides were warmed to 50 °C prior to mixing to reduce viscosity. The mixture was then poured onto the VACNT array and samples were cured in a vacuum oven at 60 °C for 24 hr [112].

After infiltration and curing, the foil substrate was peeled from the polymer embedded VACNT array to obtain a flexible VACNT composite with CNT tips protruding from the planarized surface. A grid of individual devices was patterned by etching away CNTs with a CO_2 laser-cutter to an etch depth ~10 µm. Samples were sonicated in isopropyl alcohol to clean and prepare the composite surface before diode fabrication.

8.3.2 Diode Fabrication

CNT tunneling diodes were fabricated on the surface of the polymer–VACNT composite. The CNT tips protruding from the surface govern the discrete diode junctions; diodes are electrically connected through CNT-CNT interconnections within the composite bulk. Initial attempts at improving the diode-to-diode conductivity incorporated an evaporated bottom electrode layer. This layer was deposited on the VANCT forest prior to polymer infiltration in order to connect the CNT tips that would later become the embedded lower electrodes. This approach, however, did not noticeably increase the conductivity of the polymer–VACNT composite above the bare CNT-CNT interconnections; therefore, this bottom metal electrode layer was abandoned in subsequent device iterations.

Diodes were fabricated with multiple insulator combinations using a deposition process similar to Chapter 3 and Chapter 4. The surface of the infiltrated array was conformally coated by ALD at 150 ºC to accommodate the polymer material. Prior to deposition, 300 s oxygen plasma was used to promote nucleation and conformal deposition on the composite surface. The diode tunneling structure involves 1–4 layers alternating Al_2O_3 and HfO_2. Al_2O_3 layers were formed by cycling precursors of trimethylaluminum and H_2O vapors; HfO_2 layers were formed by cycling tetrakis(dimethylamide) hafnium and H_2O. Deposition rates were approximately 1 Å/cycle. Purge times of at least 30 s were used to ensure quality film deposition at this lower temperature.

After oxide deposition, the top contact electrode was deposited by drop-casting highly conductive PEDOT:PSS (Clevios PH 1000). PEDOT:PSS was prepared with 5 vol% ethylene glycol at 80 °C and sonicated at room temperature. The PEDOT:PSS was drop cast on the polymer CNT composite surface to form 1–2 mm^2 devices. To prepare devices for electrical characterization, conductive silver paint was applied to the top electrode over an off-area to form external electrical contacts away from devices.

8.4 Results

8.4.1 Surface Characterization of Polymer Infiltrated VACNT Composites

Cross section SEM images in Figure 8.4(a) reveals the structure of the VACNT array before and after polymer infiltration and subsequent lift-off from the growth substrate. In addition to showing thorough infiltration of both PDMS and epoxy, the polymer–VACNT composites also preserved good CNT alignment. This is advantageous over other methods that involve randomly dispersing CNTs into polymer, hereby demonstrating a feasible approach to harvest large-area CNT forests while maintaining orientation.

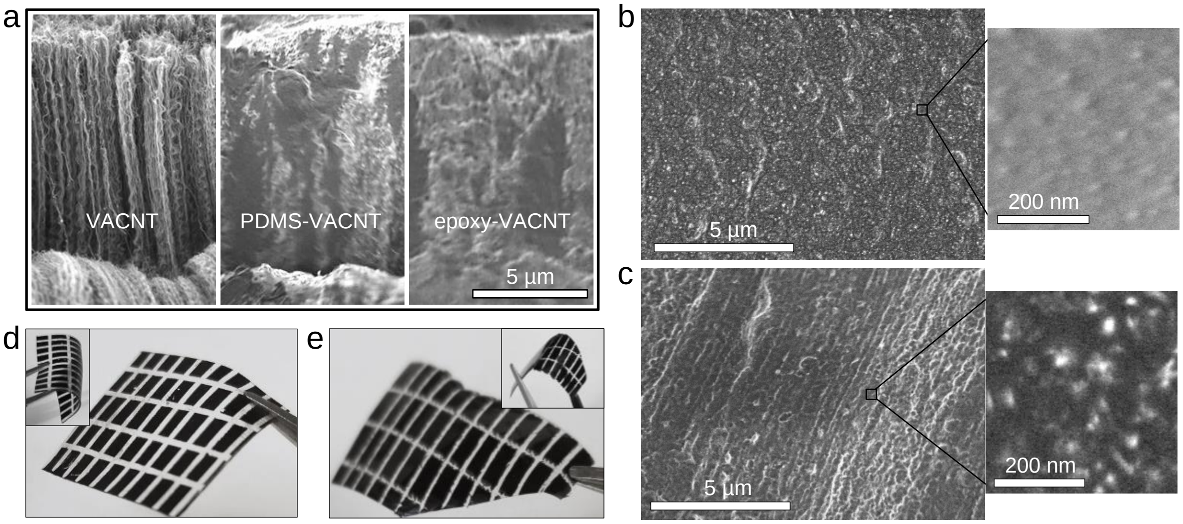

Figure 8.4. (a) Cross section SEM images of (from left to right) VACNT forest on foil, PDMS infiltrated VACNT, and epoxy infiltrated VACNT. (b-c) Top down SEM images of PDMS-VACNT and epoxy-VACNT composites, respectively. Insets are magnified images showing the tips of CNTs jutting from the surface. Photographs of (d) PDMS and (e) epoxy VACNT devices after infiltration, lift-off, and patterning. Insets show samples under bending.

The ultimate goal of the polymer embedding is to planarize the VACNT array surface in order to electrically isolate CNT tips from the remaining length for better CNT diode junction control. With the voids between CNTs filled with polymer medium, we now realize a planar diode methodology that entertains solution processed electrode materials.

Indeed, both polymer composites manifest highly planar surfaces after infiltration and lift-off, as seen in SEM images (Figure 8.4(a-c)). It is notable that the PDMS and epoxy composite surfaces differ with the epoxy displaying a much rougher surface. The epoxy exhibits striations which matches the surface roughness of the foil growth substrate—we expect the low viscosity of the epoxy and negligible shrinkage during cure to facilitate infiltration that conforms intimately with the foil surface, thereby creating such a rough pattern. We will find this to have an effect on the uniformity of dielectric layering once diodes are fabricated, and this will create challenges with diode reliability.

The surfaces are predominantly smooth at the sub-micron scale, while high magnification images (Figure 8.4(b-c) insets)) provide evidence of CNT tips protruding slightly above the polymer surface. We speculate that the polymer-coated CNT bumps seen in the magnified SEM images arise either from capillary action during polymer infiltration, or minor shrinkage of the bulk polymer upon cure.

The number density of exposed CNT tips was estimated from the SEM images of polymer–VACNT surfaces—sample images are shown in Figure 8.5(a-b). Using ImageJ software, exposed CNTs were counted at various locations of approximately 500 nm×500 nm (Figure 8.5(c-d)). The CNT number density was found to be $3.5–4.0\times10^{10}$ cm^{-2} for PDMS–VACNT and $2.6–3.7\times10^{10}$ cm^{-2} for epoxy–VACNT . These values are consistent with estimates for the bare, non-infiltrated VACNT forests ($\sim10^{10}$ cm^{-2}), indicating that the majority of the CNTs are, in fact, revealed at the polymer surface. The significance of this observation is that the exposed CNT ends will inevitably determine the nanoscale MIM junction area. Whereas in our prior works we speculated that several microns of CNT length could contribute to the diode area [87], here, the embedding confines the diode fabrication to the CNT tip. This also mitigates any potential anisotropic diode tunneling through the CNT sidewalls. With PDMS–VACNT, for instance, the inset of Figure 8.4(b) reveals that at most 20 nm of CNT tip protrudes above the surface. In this structure, controlling the length of exposed CNT may affect the diode current density by adding additional cylindrical area. The effect of CNT tip length would depend on the anisotropic conduction of electrons through the CNT and their inclination to tunnel through the sidewall area of the diode versus the tip. We point out that the strength of this infiltration and lift-off approach lies in exposing the CNT tips without the need for etching, further highlighting the processing advantage of this method.

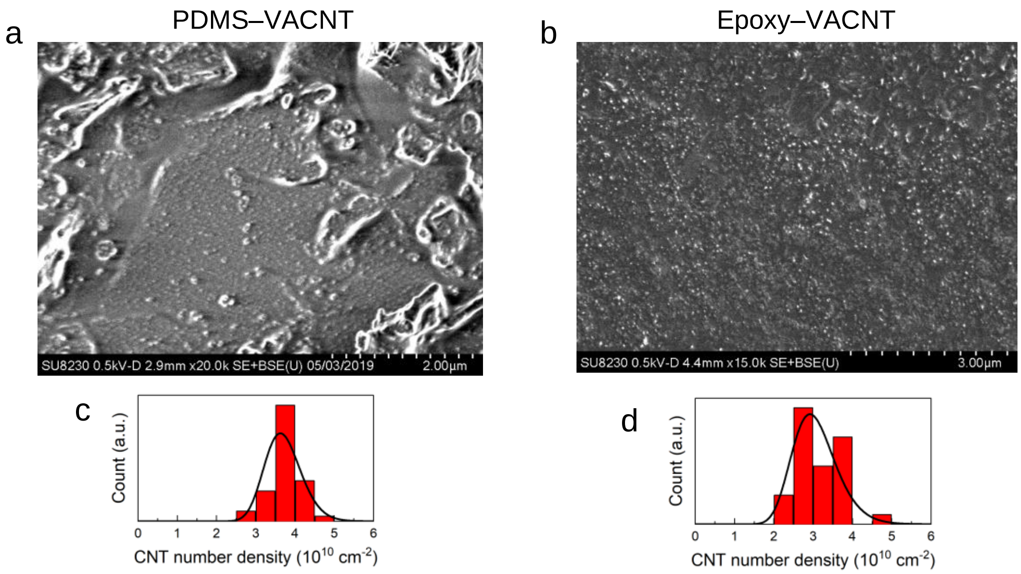

Figure 8.5. (a-b) Representative SEM images from which CNT number density was determined. (c-d) Histograms featuring the CNT number density. Black lines are fitted log-normal distributions.

Lastly, we find that the fabricated composites are flexible and electrically conductive. Figure 8.4(d-e) presents images of the PDMS or epoxy infiltrated VACNT illustrating the flexibility of the composite. Sheet resistance is 2.2 ± 0.7 kΩ/sq for PDMS–VACNT and 3.2 ± 1.5 kΩ/sq for epoxy–VACNT, which is predictably much higher than bare VACNT forests (~400 Ω/sq). The conductivity nonetheless confirms that the CNT protrusions depicted in Figure 8.4(b-c) are indeed exposed at the surface. These composites are suitable as flexible electrodes for nanoscale components. Now that we have established planar VACNT composites that can accommodate solution-processed layers, these samples will be used to develop VACNT-based MIM diode arrays in the following section.

8.4.2 Diode Characterization

Tunneling diodes are fabricated atop the polymer–VACNT composite and then the d.c. *I*–*V* characteristics are measured. Diodes composed of varying multilayers of Al_2O_3

and HfO_2 are investigated in light of these planarized PDMS or epoxy embedded VACNTs in relation to prior work in tuning the electrical characteristics through enhanced electron tunneling [55, 63, 65]. PEDOT:PSS is used as the top electrode, as it is a conductive and optically transparent polymer material that can be processed in solution [116].

Figure 8.6 shows measured *I*–*V* curves comparing diodes made on PDMS or epoxy composite with either one, two, or four layers of dielectric (6 nm total thickness). Diodes with 6 nm Al_2O_3 exhibit similar *I*–*V* characteristics on both epoxy and PDMS. Nonlinearity is good, which we found becomes more pronounced as the thickness of the dielectric is increased. Single-insulator diodes (polymer–VACNT/Al_2O_3/PEDOT:PSS) have nearly symmetric *I*–*V* characteristics ($\mathcal{A} < 1.4$). This is expected given that there is minimal work function difference between the multiwalled CNTs and PEDOT:PSS ($\Phi \sim 4.9$ eV, Table A.1) electrodes [107]. This limits the asymmetric electron tunneling that can occur. This nonlinearity observed in these Al_2O_3 diodes can be accredited to direct tunneling after approximately fitting the Simmons tunneling equation [117].

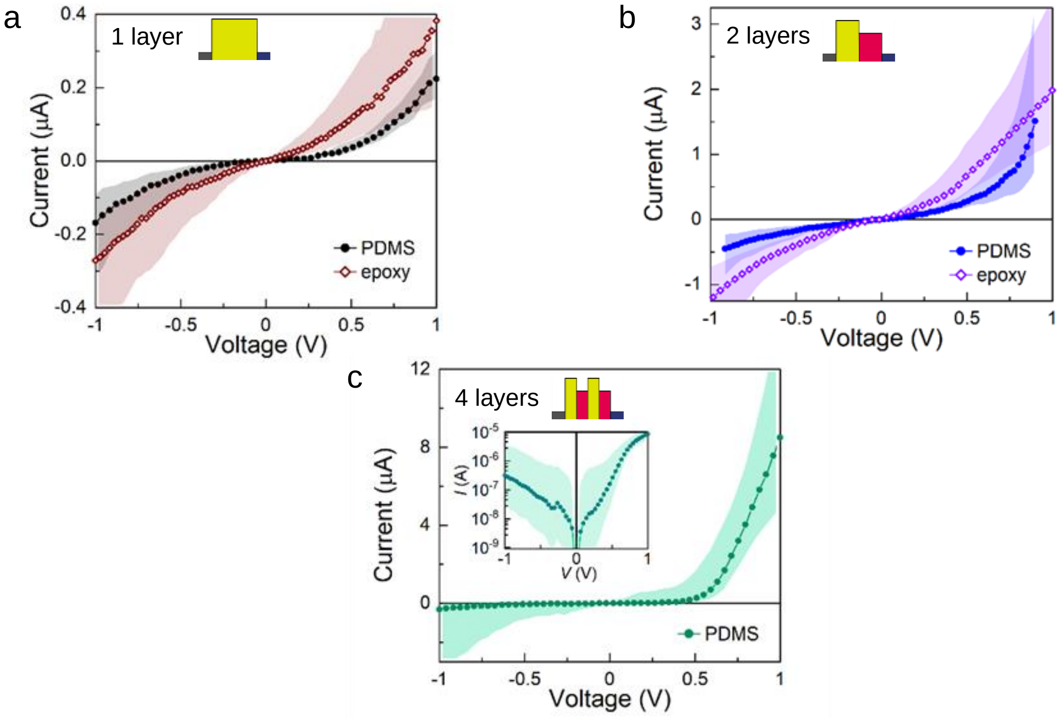

Figure 8.6. *I*–*V* characteristics for polymer–VACNT/insulator/PEDOT:PSS diodes using PDMS or epoxy infiltration media. Total insulator thickness is 6 nm, composed of (a)

Al_2O_3, (b) Al_2O_3-HfO_2, and (c) Al_2O_3-HfO_2-Al_2O_3-HfO_2. Error regimes capture device variability of up to 20 devices. Insets show the corresponding energy barriers.

Our aforementioned attempts at making two- or four-layer laminates have resulted in a pronounced improvement of rectification ability within CNT diodes arrays [86, 87, 96]. This idea is explored further here, as applied to the planar polymer–VACNT composites, to make diodes with two (Al_2O_3-HfO_2) and four (Al_2O_3-HfO_2-Al_2O_3-HfO_2) insulators. These dielectric combinations form a cascading energy barrier between the CNT and PEDOT:PSS electrodes that enhances the electron tunneling to manifest as highly nonlinear and asymmetric *I–V* curves. This notion is confirmed in Figure 8.6 for Al_2O_3-HfO_2 (3/3 nm) and Al_2O_3-HfO_2-Al_2O_3-HfO_2 (1.5/1.5/1.5/1.5 nm). Indeed, the asymmetry that is observed for a double-insulator structure is boosted to 2.9 and 2.2 for PDMS and epoxy composites, respectively. Even further enhancement is realized for the four-layer structure, with excellent nonlinearity and asymmetry up to 18. Generally, these devices exhibited good scan-to-scan stability. The reproducibility was lower overall for the epoxy composites. Since tunneling diodes are highly sensitive to the dielectric layer, one explanation for this result may be attributed to the large-scale surface roughness pointed out in Figure 8.4(c), which could be causing nonuniform dielectric thickness. There could also be problems with the dielectric laminate adhering to the epoxy surface. We note additionally that, at this time, we have not realized a measurably stable four-layer diode using epoxy composite. These issues should be explored in the future by examining the ALD process, its effect on the epoxy, and the impact of surface roughness.

More evidence pointing to the advantage of the multi-insulator tunneling diodes is seen in Figure 8.7. Asymmetry can be enhanced by an average factor of ~2× for double-layer and ~5× for four-layer devices, relative to a single Al_2O_3 diode with comparable thickness. This implies that better rectifying ability is achieved in multi-insulator structures without the accompanying reduction in current. The best device we produced—12 nm Al_2O_3-HfO_2-Al_2O_3-HfO_2 (3/3/3/3 nm)—yielded asymmetry above 250 with a median device consistently exceeding 92. However, with tunneling resistance scaling exponentially to dielectric thickness, 12 nm devices are too high resistance (~0.1–1.0 MΩ cm^2 at zero bias) to meet the needs of a practical device. The other drawback to multi-insulator diodes is much more deviation between *I*–*V* characteristics—with asymmetry varying by up to an order of magnitude. Ordinarily, minor random variations in the dielectric layer cause large fluctuations in current. For devices with multiple oxide layers, these deviations compound, resulting in even more drastic variability amongst similar devices.

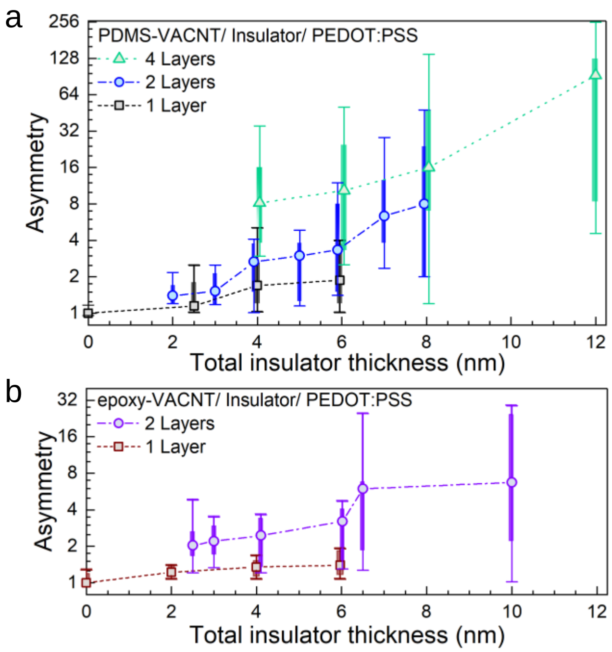

Figure 8.7. Diode asymmetry as a function of total dielectric insulator thickness for (a) PDMS–VACNT and (b) epoxy–VACNT samples. Box plots denote statistics for up to 20 devices of various batches: boxes indicate first and third quartiles and error bars denote 95 % confidence bounds.

Lastly, device yield and stability must also be addressed for large scale production. We observed that the asymmetry and sample production yield are largely dependent on the oxide thickness and choice of polymer embedding medium. Figure 8.8(a) summarizes the device yield as a function of polymer composite, dielectric thickness, and multi-insulator composition. For this analysis, diode yield is specifically defined as the fraction of all devices for a given experimental condition that gave measurable, replicable, and nonlinear *I*–*V* curves that are indicative of a diode (though not necessarily of high asymmetry). Examples of non-yielding devices include (1) current that was too low to measure; (2) linear *I*–*V* scans, which often have high current that implies a short-circuited device; (3)

scans that rapidly degrade to ohmic, either due to sudden irreversible breakdown or degradation through several scans; and (4) highly erratic or unstable *I–V* scans. In general, each experimental condition had 1–5 samples produced and 10–20 devices per sample. For yielding devices, histograms of the distribution of asymmetry is captured in Figure 8.8(b-c). In each case shown, the total dielectric is 6 nm.

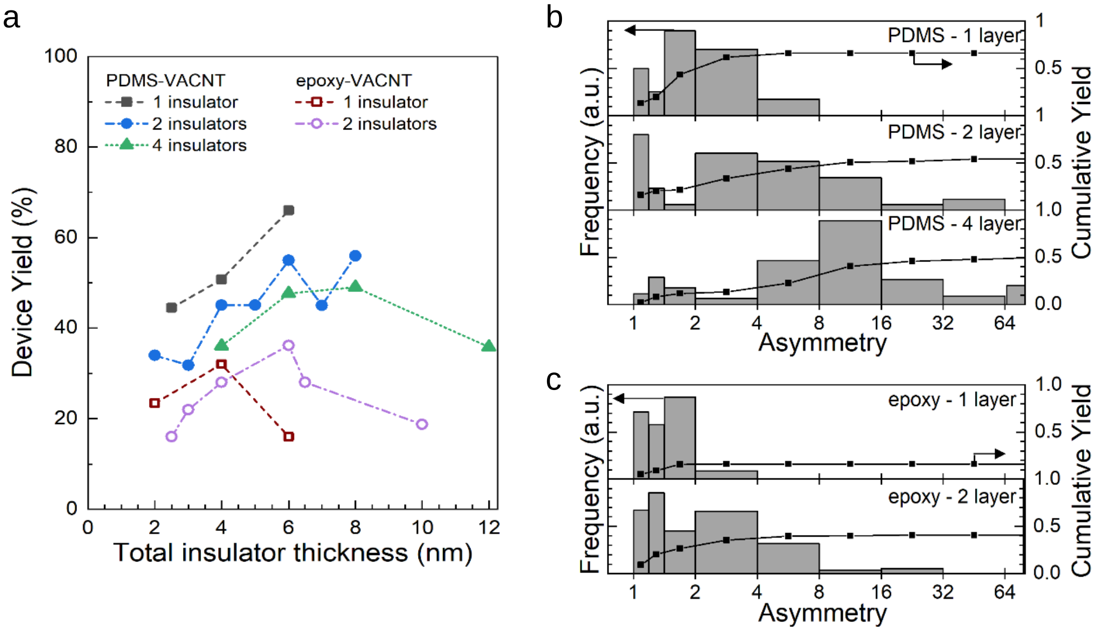

Figure 8.8. (a) Summary of device yield. (b-c) Histograms showing the distribution of asymmetry for yielding devices comprising (b) PDMS and (c) epoxy composites. Lines show the cumulative frequency, which peaks at the overall device yield (rather than 100 %).

Even though we showed that diodes could be produced with qualitatively similar *I–V* characteristics using either PDMS–VACNT or epoxy–VACNT, the experimental yield is substantially lower with epoxy: only ~25 % of devices fabricated on epoxy–VACNT composite exhibited non-ohmic and diode-like *I–V* characteristics, in contrast to 40–60 % of PDMS–VACNT samples (this is further detailed in Figure 8.10). Oxide thickness also affects device yield. The most reliable diodes usually occur around 6 nm. We found that a thin insulator tends to produce short-circuited devices with greater frequency as pinholes and defects dominate in the oxide layer and dielectric breakdown is more likely to occur. On the other hand, when the insulator is too thick then the tunneling resistance becomes too high for smooth and resolvable I–V measurements. We also speculate that the oxide layer becomes increasingly brittle and susceptible to cracking when too thick. This is evidenced by the escalating regularity of short-circuited devices we observed above 6 nm, despite the notion that thicker barriers are more resilient to dielectric breakdown. Adapting the ALD process to further accommodate oxide deposition along polymer composites—or even considering an annealing step afterwards—may remedy these issues.

In summary, this demonstrated technique for producing arrays of nanoscale tunneling diodes with polymer–VACNT composite substrates unlocks new avenues for flexible electronic and optoelectronic applications. Our use of PEDOT:PSS to make electrodes shows the adaptability of this structure to a new set of solution-processed materials. The next steps to improve these diodes will be to investigate alternative embedding media, such as high-temperature ceramic, and explore novel transparent electrodes like silver nanowires, graphene, or other conductive materials that can be processed in solution.

8.5 Demonstration of Optical Rectification

To show the potential application as a flexible rectenna for solar energy conversion, we test the polymer–VACNT diodes under 638 nm illumination (Figure 8.9). We examine the behavior of a device consisting of Al_2O_3-HfO_2-Al_2O_3-HfO_2 (1/1/1/1 nm). The PEDOT:PSS top electrode has ~80 % transmittance measured at 638 nm. The I–V characteristics for this optically tested device are shown in Figure 8.9(b-c). The device is notably stable for multiple scans throughout optical testing, exhibiting a peak $\mathcal{A} = 12 \pm 2$. This asymmetry is more modest than the highest values obtained from a thicker oxide layer, but the device stability makes it favorable for performing laser testing.

Under 5 mW incident power we observe an increase in forward-bias current, as well as $I_{sc} = 3.0 \pm 0.5$ nA and $V_{oc} = -32 \pm 5$ µV (Figure 8.9(b-d)). The second-quadrant power generation signifies the mechanism of rectification and not photovoltaic behavior. It was also observed that higher laser intensity was more likely to cause eventual device failure. We speculate this is due to thermal expansion of the composite that cracks the oxide layer, ultimately causing devices to short-circuit. This means heat dissipation is of concern for polymer–VACNT composites due to the high absorptivity of CNTs alongside poor polymer thermal conductivity.

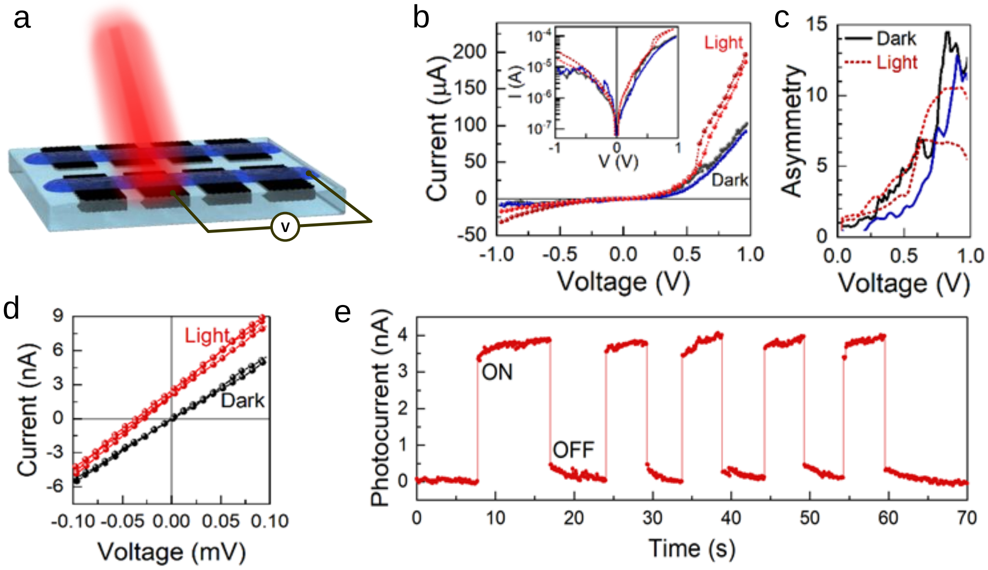

Figure 8.9. (a) Device under optical testing. (b) *I*–*V* scans of the PDMS-VACNT/Al_2O_3-HfO_2-Al_2O_3-HfO_2 (1/1/1/1 nm)/PEDOT:PSS diode. (c) Asymmetry as a function of bias. (d) High resolution *I*–*V* scans showing power generation from 638 nm at 5 mW. (e) Photocurrent monitored over time.

The photocurrent responsivity of $\beta_I \sim 0.65$ μA/W is between 2.3 and 100 times lower than the prior, non-infiltrated CNT rectennas [8, 86, 87]. This is even despite the novel incorporation of transparent PEDOT:PSS electrodes to boost power into the nanoantennas. The obvious explanation is the high composite resistance compared to pristine VACNTs on metal-coated Si wafer. Since the conductivity of the composites is governed by intertube sidewall contact. It follows that photoresponse may be improved through the bulk conductivity, such as by increasing VACNT length or density to enhance CNT-CNT interconnections, doping the CNTs to improve conductivity, or adding a bottom metal electrode layer to connect together the lower polymer-filled CNT ends. We also believe these samples leave room for improvement in the oxide layer, such as making the tunneling barrier thinner through finer control of the ALD process.

The time-dependence of the short-circuit photocurrent is presented in Figure 8.9(e). Indeed, the photocurrent responds rapidly to the laser, further evidence pointing to rectification. There also appears to be minor transient behavior on top of the initial photoresponse that was not observed in non-infiltrated CNT rectennas. Throughout 10 s illumination the I_{sc} steadily increases from 3.5 nA to 4.0 nA. This residual drift is presumed to be a thermoelectric response due to the sample heating up under the laser. This is investigated further in the following section.

8.5.1 Photoresponse Due to Laser Heating

This section seeks investigates potential thermal effects that may arise due to heating of the polymer-based samples. Here, an ohmic device without an oxide tunneling barrier is tested. The device (PDMS–VACNT/PEDOT:PSS) exhibits linear *I–V* characteristics with $R = 10$ kΩ. The device was illuminated with a 638 nm laser with incident power of 5 and 50 mW. The laser spot size is approximately the same as the device area (~2 mm^2). Sample surface temperature is monitored with an infrared thermal imaging camera (FLIR A35sc) to assess any transient behavior.

Figure 8.10 shows the device responding to the laser, producing a photocurrent that is clearly time-dependent. $I_{sc}{\sim}0.1$ nA corresponds approximately to the minor transient rise in rectenna photoresponse observed in Figure 8.9. Device temperature also gradually rises by 4 °C after 10 s laser exposure, with time-dependence that precisely matches the photocurrent. Under 50 mW incident laser power the response is even more pronounced, with $I_{sc}{\sim}1$ nA and a significant temperature rise of $\Delta T{\sim}$ 30 °C. Since the photocurrent clearly follows the transient temperature rise of the sample, this may be a thermoelectric response due to thermal gradients being developed across the sample. Further evidence of this was seen when we used a diffuser to evenly distribute the illumination across the sample: a negligible temperature gradient was observed, and no measurable photocurrent was produced in this ohmic device.

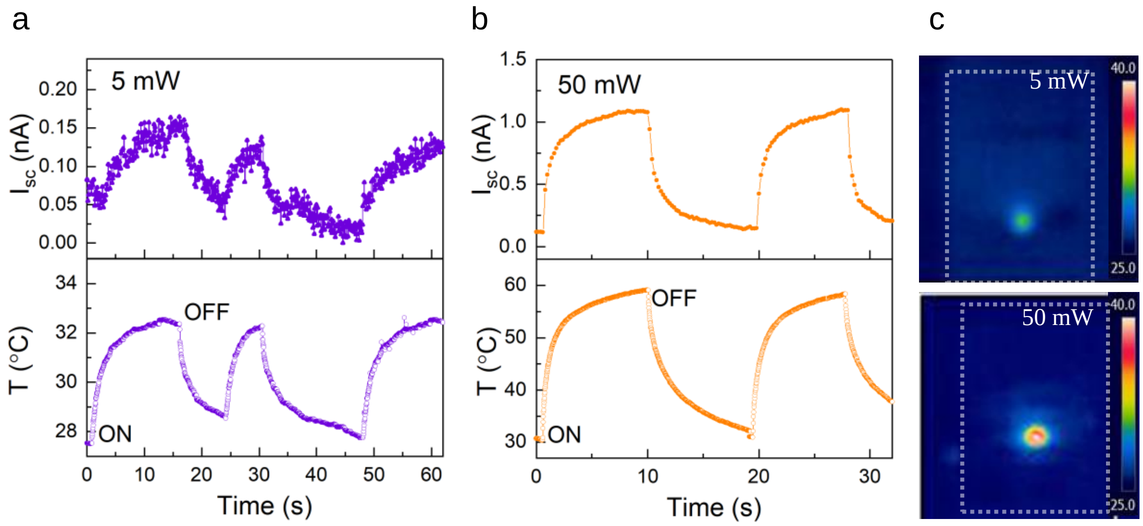

Figure 8.10. Photoresponse due to sample heating under 638 nm incident laser. Short-circuit current (I_{sc}) and sample temperature (T) recorded over time under (a) 5 mW and (b) 50 mW laser power. (c) The spatial temperature gradient across the surface after 10 s laser exposure is ΔT~4 °C under 5 mW and ΔT~30 °C under 50 mW.

Based on this investigation, it is reasonable to conclude that the minor transient current observed in conjunction with the rapid ON/OFF produced in our diode from Figure 8.9 is a result of thermal behavior acting on top of the primary optical rectification mechanism. Even though this photothermal current is small, it could affect long-term device stability and output current, especially from thermal expansion. The coefficient of thermal expansion for PDMS is 9.6×10^{-5} K^{-1}. In contrast, the thin dielectric has a thermal expansion two orders smaller (~5×10^{-6} K^{-1}), which means that 30 °C temperature rise from a high intensity laser can put significant strain on the oxide layer that may cause cracking. This could explain the issues with device yield and the tendency of these PDMS–VACNT samples to short through prolonged laser testing. Heat dissipation is, therefore, of great concern in these polymer-VACNT composites: the high absorption of CNTs coupled with poor thermal conductivity in polymers causes the large temperature rises we observed. Moving forward, it is imperative to further design the composite structure to mitigate device heating for robust implementation in solar and infrared applications.

8.6 Summary and Future Work

This chapter explores a facile method for embedding VACNT forests with flexible polymer on which are fabricated planar CNT-based tunneling diode arrays that have applications in high frequency electronics such as solar and infrared detectors. Infiltration and peel off is an easy and highly scalable technique for processing polymer–VACNT composites that works robustly with a variety of polymers. The overall fabrication of the composite-based diode is cost-effective and large-area compatible. Characterization of the VACNT diode structures reveals trade-offs between electrical performance, sample yield, and device stability. Results show four-layer tunneling barriers (Al_2O_3-HfO_2-Al_2O_3-HfO_2) produce stable devices with median asymmetry above 92. Particularly, 4 nm dielectric gives a good balance of resistance (~350 Ω cm^2) and asymmetry (>8).

Optical rectification tests have demonstrated the capabilities of this polymer–VACNT device for novel solar energy applications. Devices exhibit $\beta_I = 0.65$ ±0.50 µA/W under 638 nm light, which is lower than prior generations of CNT rectennas. The photoresponse is hindered by high resistance and is also somewhat influenced by sample heating due to the highly absorbing and insulating nature of the polymer composite. These factors should be addressed in future efforts to improve performance.

Recommended and future work to improve devices includes further tailoring the oxide structure and investigating additional electrode materials, since the initial success of PEDOT:PSS as a transparent electrode hints that other conductive polymers may work. The demonstration of solution-processible materials has unlocked new potential fabrication methods—such as slot-die coating or inkjet printing—that are worth exploring. The planar structure now allows robust patterning of the electrode layer. For instance, an IR transparent grid pattern could facilitate testing of the IR detection capabilities of this device by solving previous issues with top metal IR transparency.

These flexible samples may be practical for a variety of applications, but an assessment of their mechanical properties is still needed. For instance, deploying a rectenna as a flexible, portable electronics charger would need to meet different mechanical stresses compared to a solar converter mounted on a roof. Testing the performance of devices under bending and stretching would also be beneficial to demonstrate the potential to be applied to non-flat surfaces. Ultimately, this approach is envisioned to be desirable for a variety of flexible electronic and optoelectronic applications.

CHAPTER 9. BROADER APPLICATIONS

This chapter is devoted to discussing the broader applications for the CNT rectenna developed throughout this dissertation. Aside from solar power generation, there are several other interesting technologies to which the CNT rectenna may be applicable or potentially better suited. The goal here is to bring attention to some of these broader applications and incite further research that could accelerate the practical implementation of the CNT rectenna.

9.1 Optical Photodetection

Existing PV solar cells are well-established and commercially available; therefore, optical rectennas are unlikely to replace semiconductor solar cells in the near term. Instead, implementation of a solar rectenna for photodetection is a real possibility. Semiconductor-based photodetectors often have limitations arising from band gap-governed temperature dependence. A typical rectenna based upon tunneling rectification is relatively insensitive to temperature, making the rectenna a possible alternative photodetector.

Performance metrics used to characterize photodetectors include the responsivity and response time. Detectivity is another metric usually used in comparing the performance of detectors as it reflects the sensitivity to differentiate a signal from background noise [118]. The specific requirements that are emphasized for photodetectors varies depending on the field of application. For instance, response speed is emphasized for optical communications, whereas detectivity is valued in astronomical applications [88]. Photodiode clocking frequency is limited by the charge transfer speed. The response time of a p–n photodiode is usually ~1 μs, whereas for an optical rectenna the response time is necessarily ultrafast based on the electronic tunneling of the device.

The 16 nm CI^{4}M rectenna device demonstrated throughout Chapter 5 and Chapter 6 currently offers specific optical detectivity on the order of $D^{\star}{\sim}10^{7}$ cm Hz$^{1/2}$/W. This value is based upon the passive photoresponse near zero bias. However, we have seen the device exhibit significantly higher photocurrent generation at higher ~1 V bias. Detection capabilities are then greatly enhanced if the rectenna is operated under bias. Accounting for both shot noise and Johnson noise, the biased detectivity improves to more than $D^{\star}(1\text{V}) \sim 10^{10}$ cm $\text{Hz}^{1/2}$/W (Figure 5.7(b)). As demonstrated in Chapter 5, more responsive CNT rectennas are possible with the right tunneling structure if device fabrication can be refined. For instance, the thinner 12 nm CI^4M (Table 5.1) has a detectivity that is about another order of magnitude improved due to the better photoresponsivity. It should also be emphasized that empirical observations have indicated that CNT rectenna performance improves when devices are fabricated over smaller areas, likely a relationship between the overall defects throughout the array. We posit that the realistic implementation of CNT rectennas could see greater detector performance if fabricated in small CNT bundles using advanced fabrication processes with precise control.

The use of CNT rectennas as the detector for optical interconnects is examined next. Further discussion of the photodetection capabilities in IR regions is presented in Section 9.2.3.

9.1.1 Optical Interconnects

In the pursuit of faster data transfer speeds in computing and communication systems, conventional metal wiring is a limiting factor to rapidly transmitting information. Metal wires have high resistance and capacitance which limits the response time and increases power dissipation over long distances or when scaled to small dimensions. Researchers have advocated optical interconnection as a faster and more efficiency way of quickly transferring large quantities of information [119–122]. The CNT rectennas is especially suited to address the latency concerns via optical interconnects.

Optical interconnects transmit signals between integrated circuit components using light. They are motivated by their high latency and low power consumption against conventional metal connections. Some additional benefits of using optical interconnects include reduced heat dissipation, possible non-contact geometries and other architectural advantages, and longer distance transmission without performance degradation. In optical interconnects, the energy required to transmit a pulse of information is related to the energy needed to charge the photodetector capacitance, C_d, and the required signal voltage, V_{signal}, which is usually less than 100 mV. It is given by the expression [119]

$$E_p \geq C_d V_{signal} \frac{\hbar\omega}{e} \,. \tag{9.1}$$

The use of optical interconnects is useful when the distance is long or the detector capacitance is small relative to the wire line capacitance that would be alternatively be used. This means C_d should be less than 1 fF for a common configurations involving signal transfers over ~100 µm distance.

For a fast photodetection response time and low capacitance, optical rectennas have been discussed as a potential component [123]. Based on the typical values discussed in equation (9.1), a reasonably efficient photodetector with low capacitance and good integration can be satisfied with an optical rectenna.

The CNT rectenna is especially suited as the photodetector component needed for ultrafast information transfer. The ultralow capacitance of the single CNT diode junction shows that high latency and low optical energy is possible. Bearing in mind the CNT junction capacitance of ~aF, a CNT detector array would need to be roughly 1µm × 1µm to maintain an equivalent device capacitance below 1 fF. At present, the CNT rectenna fabrication process would need to be refined to use more accurate patterning or lithography steps to grow the CNTs on chip in such small areas. In general this is still a reasonable endeavor. The other issue will be boosting the CNT detector array current responsivity to register an appreciable signal at this small of device area. Again, more sophisticated fabrication methods would be expected to yield higher devices with fewer defects throughout the array that diminish the response. In summary, utilizing optical rectennas in detectors can potentially tackle the main issues of creating dense, low-power, and low latency interconnections. Further development of the CNT rectenna could mark an exciting paradigm for ultrafast electronics communication.

9.2 Infrared Applications

The primary focus of this dissertation has been on rectification of solar and near-IR (NIR, 0.7–3 µm) frequencies. However, there exists widespread interest in implementing rectennas for applications spanning the mid-IR (MIR) spectrum (3–50 µm according to ISO 20473 scheme). Outside of solar energy conversion, high performance CNT rectennas could be valuable for IR harvesting and detection. One reason the IR rectenna may be valuable over visible wavelength rectification is the lower frequency of operation that loosens the burden imposed on the device cutoff.

This section will summarize the predicted IR response of the presently investigated CNT rectenna structure. Then, potential IR detection and power generation applications will be introduced. These applications will be discussed in light of the CNT rectenna IR performance in order to provide context for which technologies this device may be most easily applied.

9.2.1 *Predicted Infrared Performance of CI^{4}M Rectenna*

The IR rectification response is estimated for the CNT/Al_2O_3-ZrO_2-Al_2O_3-ZrO_2 (16 nm)/Al rectenna structure using the PAT model developed in Chapter 6. IR conversion efficiency is illustrated in Figure 9.1. η increases gradually with intensity since higher concentration of the light into a finite antenna area enhances the optical field voltage. This could be useful for generating output power from high intensity thermal sources. As explained earlier, the NIR response increases with photon energy. However, efficiency in the MIR range is less than 10^{-6} %, even when intensity is as high as 500 mW/cm^2, and response drops off exponentially at wavelengths above 3 µm.

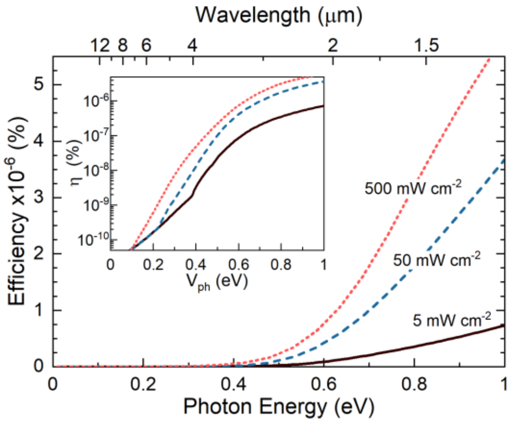

Figure 9.1. Predicted efficiency in the IR regime for 5–500 mW/cm^2 source intensity.

There are several expected reasons for this poor IR response:

- Nonzero turn-on voltage. Even through the CIM tunneling diode meets the speed requirement for IR rectification, the poor asymmetry for $V < 0.3$ V means that there is not an appreciable photon assisted power generation at photon energies below ~0.3 eV (~4.1 µm). Hence, improved IR response could be obtained by increasing the operating voltage such that the diode exhibits asymmetry at ~100 mV.

- Antenna effects: It is likely that the CNT lengths are tailored more towards visible frequencies rather than MIR. Further study of the CNT rectenna should explore increasing the CNT array height to leverage the antenna length effect and hopefully shift the region of operation closer into MIR.

- Electrode transmission. A significant research challenge involved with IR rectification involves engineering the top electrode to permit transmission of radiation into the CNT array. Owing to the high frequency behavior of thin metal films, the top electrode is expected to block almost all incident IR radiation. As was mentioned in Section 5.3.2.2, it was speculated that visible light transmission could be artificially enhanced due to a metal-mesh forming throughout the metal-coated CNT array. On the other hand, MIR wavelengths are larger than the average CNT-CNT spacing, and so we could predict that

> MIR radiation is shielded from being passed into to the CNT nanoantennas. One potential solution would be to explore alternative conductive materials that are more transmissive to MIR. Another method is to pattern the metal in a grated architecture that could allow IR light to pass through. The nonuniformity of a freestanding CNT forest does not permit metal patterning at the needed resolution for this approach. However, the novel polymer infiltrated CNT forest discussed in Chapter 8 has a planar surface that can accommodate high resolution metal patterning.

Next, nascent applications of IR rectennas are presented for sensing and power generating technologies. Discussion of application-specific parameters is included to add context to the fields for which the CNT rectenna may have the best change for near-term practical implementation.

9.2.2 Infrared Harvesting

Waste heat harvesting is a burgeoning field for the rectenna that is currently without good existing solutions—as opposed to harvesting visible light where cost-effective solar technologies are already implemented. The difficulty in converting waste heat, such as from industrial thermal sources, stems from the low temperature (<300 ºC). Heat engines cannot effectively convert this low-utility heat and the low energy photons are not able to produce photocurrent through the bandgap of most semiconductors. Thermoelectric devices are one attractive solution, but still run into challenges related to efficiency, fabrication, and contact issues [124, 125]. Rectennas, instead, have the potential to meet this technology void for recovering low-utility thermal energy. A MIR rectenna should be capable of utilizing ubiquitous thermal sources emitting in the range of 3–30 µm [126]. The system cutoff frequency in this range only 10–100 THz, which is much less demanding than for visible light rectification.

Geothermal energy harvesting is a specific application for a CNT rectenna designed to operate in IR. Geothermal energy, which is primarily in the 3–6 µm range, is a large and relatively untapped source of renewable energy, though it is mainly low utility and therefore challenging to convert using ordinary means [124]. There is a lot of interest to find a solid state device for converting geothermal energy without needing to first convert to mechanical energy (such a thermodynamic heat engine cycle). Thermoelectrics are being considered but suffer from low power production and significant thermal contact issues. Rectennas, on the other hand, are naturally non-contact energy converters.

The CNT rectenna in this dissertation has not been yet been measured around 3–6 μm, but the simulated rectenna response suggests that small power generation is possible in at least a portion of this range. Higher efficiency can be obtained if the intensity of the thermal source is increased such that multiphoton tunneling manifests. For a blackbody source at ~725 K (peak wavelength $\lambda \sim 4$ μm), the Stefan-Boltzmann law estimates radiation intensity around 1.5 W/cm^2. Based on order of magnitude estimations around the simulated MIR response, geothermal conversion efficiency at this intensity could reach nearly 0.1 % if we could bolster the diode current to 1000 mA/cm^2. Higher efficiency could also be realized if the rectenna was tailored to respond to the entire geothermal region. This efficiency is still not comparable to a heat engine, but the advantage of the CNT rectenna is that it is a solid state device and also does not require direct physical contact with the source.

Rectennas are also being investigated heavily for wireless power transmission. The concept of space-to-Earth power transmission proposes having solar energy converted by ultra-high efficiency solar panels mounted on satellite arrays in orbit [126, 127]. Then the energy can be beamed back to Earth where it is collected by terrestrial rectennas. An atmospheric window exists from 8–13 μm, which permits radiation to pass through the atmosphere with minimal absorption and scattering [85]. If an efficient IR rectenna could be implemented in this wavelength region, then this solution has real potential to make a useful concept for increasing solar power production. It also would bypass other rectenna harvesting challenges because the beamed energy could be made of coherent, monochromatic, and polarized to optimize rectenna conversion [22, 126, 128].

Another, more straightforward, space application is the direction conversion of terrestrial radiation. There is 100 W/m^2 of available thermal radiation emitted from the Earth in the MIR atmospheric window [129]. Satellites might utilize IR rectennas to harvest up to 25 W/m^2 of the energy from Earth (based on the Carnot efficiency for a rectenna mounted to a satellite at -50 ^{o}C). The advantage of the CNT structure with respect to in-space applications is their light weight, since CNTs are inherently low density and the rectennas could conceivably be made just 10's of microns in thickness according to the CNT array thickness.

9.2.3 Infrared Detection

IR detectors operator either from thermal detection or photon detection. Thermal detection mechanisms utilize material properties affected by temperature changes from the absorption of radiation. The limitation here is the response time; bolometers, for instance, have ~ms slow response times. IR photon detection generates photocurrent due to charge carriers in a semiconductor material. Response time is fast, but the low energy of IR photons requires cryogenic cooling to minimize noise. Therefore, operating temperature is an important factor.

There are many discrete applications of IR detectors [89]. Detectivity, responsivity, and response time are common figures of merit used to characterize IR detector performance [118]. The response time of an optical rectenna is necessarily ultrafast, which makes them unrivaled in comparison to bolometers. The IR detectivity of the CNT rectenna could be as high as 10^9 cm Hz$^{1/2}$/W under bias if the antenna and diode behavior were adjusted to fit the desired IR spectrum. In contrast, other researched MIR photodetectors have obtained detectivity on the order of at least 10^{10}–10^{12} cm Hz$^{1/2}$/W [88]. HgCdTe are widely used MIR detectors, showing $D^{\star} \sim 10^{10}$ cm Hz$^{1/2}$/W at 77 K. $D^{\star}$decays with temperature to 10^7 cm Hz$^{1/2}$/W at room temperature. Active cooling is not always a practical approach if the detector needs to be portable, light weight, or low form factor, such as night vision equipment. The relative temperature insensitivity of tunneling-based rectennas is an advantage over semiconductor detectors.

Some new concepts of IR detectors that are being investigated include graphene geometric diode detectors [130] and traveling-wave MIM-based rectennas [131]. These devices have achieved room temperature detectivities of 10^6–10^7 cm Hz$^{1/2}$/W, with projected improvements to 10^8–10^9 cm Hz$^{1/2}$/W. The CNT rectenna concept has already demonstrated room temperature operation. The IR detector capabilities at the low end of the MIR spectrum is expected to be at least 10^5–10^6 cm Hz$^{1/2}$/W without further adjustment. Modifying the diode structure, the antenna frequency bounds, and incorporating IR-capable electrodes, could realistically increase the MIR response by several orders of magnitude to be on par with existing thermal detectors. The advantages of the CNT rectenna remain the incredible response time, polarization dependence, room temperature operation with temperature stability, and fabrication using inexpensive materials and scalable processes.

In spite of the great potential offered by the CNT rectenna in terms of IR detection, a lot of challenges remain before practical implementation can be realized. Electrical performance is the first hindrance. The tunneling diode of the representative Al_2O_3-ZrO_2-Al_2O_3-ZrO_2 structure needs to be greatly improved, namely increasing forward tunneling to boost photoresponsivity while simultaneously suppressing dark reverse current. Minimizing noise and electrical variability is also critical to making this device suitable for application. The polymer embedded CNT rectenna offers many promising routes to increasing optical and IR detector performance. This polymer–VACNT structure is still in the early stage of research. The primary bottleneck to implementing this structure lies within the considerable variability and noise in response. Also, as previously discussed the polymer–VACNT rectenna exhibits a transient response due to sample heating that must be mitigated with more thermally conductive material choices.

Lastly, even though this work is focused on CNT rectenna arrays, other nanomaterials could be used that leverage similar 3-dimensional array architecture. For instance, an array of highly doped aligned Si nanowires could be used in place of CNTs. The micron-sized diameter of typical Si nanowires prevents optical-frequency rectification, but this material could be highly advantageous as a MIR rectenna were the diode capacitance would be less restrictive [114].

Despite current limitations, the efforts presented in this dissertation point to the realistic prospect of fully optimizing the CNT rectenna for real-world IR detection and harvesting applications.

CHAPTER 10. CONCLUSIONS AND RECOMMENDATIONS

In this dissertation, optical rectennas based upon vertical arrays of CNTs were studied. Devices were fabricated to characterize CNT diode junctions in order to better understand the role of the dielectric layer on the electrical properties. Principle results provided verification of the qualitative agreement to traditional fabricated MIM tunneling diodes. Fabrication of CNT diodes featuring multiple dielectric layers in combination enabled enhanced electrical properties. The overall culmination of diode investigations led to optical rectification demonstrations with improved conversion efficiency and device stability. A model of the photon-assisted tunneling was developed and combined with optical measurements to provide affirmation of the rectification mechanism and further elucidated the contributions of the diode and CNT nanoantenna. Finally, a novel concept of polymer infiltrated samples was introduced that facilitates commercial development with alternative, polymer-based electrode materials.

This chapter will summarize the findings presented throughout this body of work and provide recommendations for future research that build upon this dissertation.

10.1 Summary of Key Findings

Studying the effect of the tunneling barrier geometry—height and width—provided important incremental advances in the tunneling characteristics of the CNT diode. The exponential effect of barrier size on tunneling resistance is important for creating higher performance devices. Overall, results were qualitatively consistent with traditional planar fabricated MIM diodes. There are also contributions from resistance losses due to defect-induced shorting which dampen the exponential strength of these characteristics. Device fabrication is thus found to be limited to about 4 nm oxide thickness before defects and large-area fabrication variability becomes unmanageable.

Examination of CNT diodes that feature multiple dielectric layers shows that electronic conduction can be tuned to produce diodes with enhanced properties. The key implication of this finding is that the use of multiple insulator layers introduces more freedom to manipulate the tunneling barrier, taking the functional requirements off of the electrodes. Multi-insulator CNT diodes demonstrate excellent diode-like response even with minimal electrode work function asymmetry. Therefore, these novel multi-insulator CNT diodes can use air-stable materials.

Measuring the response of these multi-insulator CNT devices under illumination shows a correlation between enhanced diode figures of merit and power conversion ability. Photocurrent scales with diode conductance whereas the photovoltage scales with asymmetry as well as how soon the diode current turns on. Asymmetry ~2 is not adequate enough to produce any measurable rectenna behavior, while there are diminishing returns for asymmetry past several dozen-fold. Peak rectenna efficiency of 1.9×10^{-5} % has been achieved in a high asymmetry CI^{4}M (CNT/Al_2O_3-ZrO_2-Al_2O_3-ZrO_2 (12 nm)/Al) device. The 20-fold improvement relative to prior devices is a result of the several times increase in asymmetry and current density. Optical measurements of a highly stable 16 nm CI^{4}M rectenna demonstrate wavelength-dependent rectenna response over the visible and NIR spectrum.

Comparing optical measurements to PAT theory broadens our understanding of the fundamental rectification processes of the CNT rectenna in ways that were unattainable through experiments alone. The agreement between measurements and theory marks important evidence of the rectenna mechanism. Results suggest that the CNT rectenna operates under constant a.c. power mode. Wavelength-dependent response is also inferred as due to a combination of antenna wavelength-dependent effects and diode RC cutoff. The cutoff frequency is estimated to be 780 THz.

The model of PAT is analyzed with respect to hypothetical CNT device improvements. The largest boost in conversion efficiency comes from a comparable reduction in diode resistance. Meanwhile, the model suggests much room remains for gradually increasing efficiency by designing diodes to improve asymmetry, minimize leakage current, and shift the cutoff frequency to allow for higher operating regime. With the appropriate advancements in the CNT diode, an efficiency in excess of 0.1 % could be achieved.

Dichromatic rectification measurements are also found to match theoretical predictions. This agreement marks a great advancement of our comprehension of the CNT rectenna operation. However, dual-wavelength response is diminished versus monochromatic illumination, which analysis of the theory suggests is due to frequency mixing. The rectenna also demonstrates a response to full broadband solar radiation that delivers efficiency of 2×10^{-6} %. Solar measurements suggest that spectral splitting could improve this efficiency.

A facile and robust method for embedding the aligned CNT forest in polymer is explored to develop planar CNT tunneling diodes. This infiltration method is a key to producing scalable devices that greatly advances the near-term applicability of the CNT rectenna. Polymer infiltrated CNT diodes with transparent PEDOT:PSS electrodes demonstrate optical power rectification reaching responsivity of 0.65 µA/W. The polymer embedded samples also exhibit a transient photothermal response due to heat trapping in the insulating polymer medium. The polymer infiltrated CNT device is an important advancement towards realizing a flexible optical rectenna.

10.2 Recommendations

These studies have identified several avenues for future work on CNT rectennas. A summary of recommended opportunities for research is provided below.

- Alternative electrode materials: From the onset, the top electrode has been a bottleneck to the CNT rectenna performance. This work's bypassing of the reactive Ca electrode marked a boon for demonstrating the rectenna in air. Still, the Al and Ag metals used in this structure are not ideal: materials with lower work function, higher conductivity, and better transparency would have a commensurate effect on improving the efficiency. Several novel materials have been suggested, including graphene, ITO, and conductive polymers. The use of PEDOT:PSS here was a great step towards realizing these novel-electrode rectennas. Zhou *et al*. reported a universal method to lower the work function of common organic electrode materials [107]. A 10 nm thin film of PEIE modifies the electrode surface to facilitate work function reduction. They showed a decrease in work function of metals like Ag by 0.9 eV and also lowered the work function of PEDOT:PSS substantially from 4.9 to 3.3 eV. In the CNT rectenna, this would give a huge, much needed boost to the diode properties. These work function surface modifiers are also processible from solution in air, making this approach an attractive alternative to more reactive but naturally low work function materials. It can also easily be implemented in the facile processing of our polymer–VACNT composite rectenna.

- Doping CNTs to enhance conductivity: It is well known that doping alters the electronic properties of CNTs. A simple, straightforward way to improve electrical properties is to dope the CNTs to increase conductivity. A related concept is doping to enhance the availability of electrons in the CNT material (which is relatively low compared to metal electrodes). It has been postulated that boosting the electron density may remedy the charge imbalance between the CNT and upper metal electrodes, which could assist forward bias tunneling. Insofar as the diode properties, Berdiyorov and Hamoudi simulated the effect of chemical doping on the same CNT–insulator–metal structure presented in this body of work [84]. They found drastic enhancement in rectification by fluorinating the outer surface of CNTs due to voltage-dependent charge localization. Given the direct correlation to this work, this study presents an exciting framework to experimentally pursue doping to enhance the CNT diode transport. Lastly, controlling the antenna properties of CNTs can be accomplished through substitutional doping (e.g. N or B) [36]. For instance, researchers have shown a blue shift in the resonance frequency of doped CNT bundles. This may be a route to favorably control the optical properties of CNTs to tailor or enhance optical or IR spectrum antenna absorption.

- Additional investigation and testing of the CNT nanoantenna: Because of several loss mechanisms in the early stages of power transmission to the CNT array, the actual antenna radiation efficiency and spectral behavior has remained elusive. Further experiments. As introduced in Chapter 2, aligned

CNT arrays exhibit classical antenna effects: polarization and length dependencies. However, more robust experimental quantification of these antenna effects is warranted in our specific rectenna architecture. The effect of CNT length on antenna properties is particularly important to understanding whether these CNT rectennas can be tuned to desired wavelength regimes. The question of note is whether the entire CNT length is utilized in the absorption, or if a shorter rectenna could be more suitable for the extraction of freely propagating waves into an alternating current within the antenna. The current methods of fabricating these CNT rectenna structures still introduces too much variability in the CNT array height for controlled experiments to be conducted. The polymer–VACNT composite, featuring an encapsulated CNT structure, is promising for these cases: it could accommodate etching to systematically remove CNT material in order finely control the CNT array height. This is the most promising route to controlling the antenna.

- Multiwall CNT diameter: Since the nanoscale CNT tip facilitates the attofarad junction capacitance, changing the multiwall CNT diameter should shift the frequency regime of operation. I recommend a systematic test of the rectenna response to illumination through samples with varied CNT diameters to verify that the diode capacitance is indeed follows the area of the CNT tip. The cutoff frequency could be improved by implementing thinner multiwall CNTs. If instead the rectenna is desired to operate in IR, then an optical cutoff frequency is unnecessary. A larger CNT tip area should improve junction conductivity.

- Study energy harvesting in single CNT rectenna junction: Since this large-area CNT rectenna is based upon the cumulative response of a parallel array of antenna-coupled diodes, the sample is subject to significant losses from defect junctions. This has been made evident in the earlier diode characterization, in which it was inferred that pinholes, defects, and general variability across individual tunneling junctions dilutes the net diode behavior. Therefore, it would be a useful endeavor to test the optical response of a single or small bundle of CNT rectenna junctions. The current density and asymmetry of a single, ideal CIM diode is predicted to be enormously better than the cumulative array observed here. The optical rectification that could result from illuminating a single junction is intriguing and would be beneficial to further understanding the limits of rectenna operation.

- Perform mechanical testing of the polymer–VACNT rectenna devices to assess performance under repeated bending and stretching. The flexibility of the composite is evident, but the mechanical and electrical robustness of the diode layers are still a limiting factor that need to be improved for flexible rectenna applications. Additionally, it would be valuable to explore applications in which the flexibility and light weight of the polymer–VACNT rectenna could be an asset or meet a hitherto unfulfilled market need.
- Test rectification in the MIR regime: There are several alternative applications throughout the IR spectrum in which the CNT optical rectenna may find easy implementation. As discussed in Chapter 9, some of these include harvesting or detection technologies ranging from 3 µm past 10 µm. Experiments testing the CNT rectenna response in the MIR could validate the devices in relation to other researched technologies for detection and conversion. The challenge is ensuring the device materials are optimized for MIR wavelengths. Preliminary attempts at measuring 10.6 µm response did not produce a resolvable signal. We also note that the top metal electrode layer is not transmissive to 10.6 µm. Estimations based on PAT suggest that the present CNT rectenna structure is not optimized for MIR testing. Instead, it is recommended that the CNT rectenna be redesigned and optimized for MIR testing—namely, incorporating IR-transparent electrode materials or patterning and confirming or adjusting the CNT array dimensions to suit efficient MIR antenna operation. The planarized polymer–VACNT structure can ideally permit electrode patterning to facilitate MIR testing, and the embedded array can accommodate novel IR materials that may require solution-processing.
- Detailed simulation of the broadband photon-assisted tunneling and testing of different broadband ranges: Computation of the broadband solar rectification

I–V curves is warranted in light of the measured photoresponse under sunlight. The equation and procedure for calculating broadband rectification is detailed in [5] based upon the generalized formulism by Tucker *et al.* [76]. Additionally, broadband measurements and simulations are recommended across a range of blackbody temperatures. This would allow an exploration of potential alternative applications for the CNT rectenna besides sunlight harvesting. At radiation source temperatures below that of the sun, the peak wavelength will shift to lower frequencies that would mitigate high frequency losses beyond the cutoff frequency, though the CNT array might have to be better optimized in such a case so as to improve lower-frequency antenna response.

- Investigate alternative nanostructures for rectification: Even though this work has focused on CNT optical rectenna development, there exists other nanomaterials that can be suitable as a substitute for the CNT array. Si nanowires could be a promising alternative. Si nanowires can be grown in highly aligned and uniform arrays, and if highly doped, could mimic the nanoantenna functionality of the CNTs used here. Furthermore, Si nanowire arrays have been demonstrated with polymer embedding using methods similar to the polymer infiltration approach developed in Chapter 8 [114]. However, the typical diameter of Si nanowires grown in aligned arrays is several microns. If MIM tunneling diodes were fabricated on the array tips as usual, the large diameter would create a prohibitively larger diode capacitance that would be expected to render the RC cutoff frequency far too large for optical rectification. Instead, the Si nanowire arrays could be a boon for MIR energy conversion, where a lower cutoff is permissible.

10.3 Contributions

- Designed CNT-insulator-metal diodes with stable materials to facilitate the first demonstration of optical power rectification in air.
- Fabricated and characterized multi-barrier tunneling diodes to enhance the electrical properties of the diode and ultimately realize an improvement in rectenna optical conversion efficiency of nearly two orders of magnitude.
- Created a model of PAT to simulate the fundamental operation of CNT rectenna devices. Provided substantial evidence of the rectenna mechanism and the role of CNT antenna effects, cutoff frequency, and impedance matching.
- Demonstrated solar power rectification under real sunlight and environmental conditions.
- Established a novel, facile, and robust method of infiltrating VACNT arrays with polymers to produce planar and flexible CNT tunneling diodes.
- Produced flexible CNT diode arrays that incorporate solution processed PEDOT:PSS as an optically transparent and conductive polymer electrode.
- Demonstrated optical rectification using these polymer infiltrated CNT diodes.

10.4 Publications and Presentations Resulting from This Work

Journal Papers

- E. C. Anderson, T. L. Bougher, and B. A. Cola, "High performance multiwall carbon nanotube–insulator–metal tunnel diode arrays for optical rectification," Adv. Electron. Mater., 4 (3), 2018.
- E. C. Anderson and B. A. Cola, "Photon-assisted tunneling in carbon nanotube optical rectennas: characterization and modeling," ACS Appl. Electron. Mater., Apr. 2019.

- E. C. Anderson, A. P. Patel, J. J. Preston, and B. A. Cola, “Tunneling Diodes Based on Polymer Infiltrated Vertically Aligned Carbon Nanotube Forests,” Nanotechnology, Jun. 2020.

Conference Papers

- E. C. Anderson, T. L. Bougher, and B. A. Cola, “High performance multi-insulator carbon nanotube tunnel diode arrays,” *Proc. 16th Intl. Heat Transfer Conf.*, Beijing, China, Aug. **2018**.

Presentations

- E. C. Anderson, “High performance optical rectenna arrays using multiwall carbon nanotube-insulator-metal tunneling diodes,” 233rd Electrochemical Society Meeting, Seattle, WA, May 2018.

- E. C. Anderson, “Flexible carbon nanotube rectenna for solar energy harvesting,” Career Research and Innovation Development Conference, Georgia Institute of Technology, GA, Feb. 2019.

- E. C. Anderson, “Next generation of carbon nanotube optical rectenna for energy harvesting,” Gordon Research Conference, Ventura, CA, Feb. 2019.

- E. C. Anderson, “Carbon nanotube rectenna for solar energy harvesting,” Department of Physics, Bradley University, Peoria, IL, Mar. 2019. (Invited).

- E. C. Anderson, “Optical rectenna arrays using carbon nanotubes: from fundamental understanding to next generation devices,” *236th Electrochemical Society Meeting*, Atlanta, GA, Oct. 2019.

APPENDIX A. MATERIALS REFERENCES

A.1 Electronic properties of materials used in this work

Table A.1. Work functions of electrode materials used in this work.

Material	WF (eV)	Reference
Ag	4.3	[86]
Al	4.3	[86]
Ca	2.9	[8, 107]
Multiwall CNT	~5	[8]
PEDOT:PSS	4.9	[107]

Table A.2. Electron affinity, χ, and dielectric constant, ε_r, values of dielectrics used within this work. Values are reported from references that used similar thickness and deposition methods.

Material	χ (eV)	ε_r	Reference
Al_2O_3	1.4	7.6	[53, 55]
HfO_2	2.25	18–25	[53, 55, 132]
TiO_2	3.9	83–100	[64, 133, 134]
ZnO	4.3	8.6	[66, 135, 136]
ZrO_2	2.75	22	[55, 83, 137]

APPENDIX B. ELECTRICAL CHARACTERISTICS OF CNT-INSULATOR-METAL DIODES

B.1 Conduction Mechanisms

Electron conduction is explored in CIM tunneling diodes to determine the role of dielectric insulating material on dominant conduction mechanisms. Direct tunneling occurs when electrons tunnel through the trapezoidal barrier formed between asymmetric MIM structures. At sufficiently large applied bias, Fowler-Nordheim tunneling (FNT) occurs as the barrier is lowered such that electrons only need to tunnel through the upper triangular region of the barrier. The tunneling current density for FNT is related to the applied bias, V, by $I_{FNT} \sim V^2 \exp\left[-\frac{1}{V}\right]$. Therefore, plotting $\ln(I/V^2)$ vs. V^{-1} produces a straight line during dominant FNT (Figure B.1(left)). Electron affinity, χ, influences the onset voltage for FNT. Large χ lowers the barrier height, thereby forming a triangular tunneling barrier at lower bias. The small electron affinity of Al_2O_3 ($\chi = 1.4$ eV) requires a large forward bias around 2.9 V to initiate FNT in our CNT-I-Ag diodes. *I–V* measurements using Al_2O_3 are preferably conducted below that bias range to avoid oxide breakdown. We see that Al_2O_3 is primarily governed by direct tunneling. Though the emergence of FNT is seen just before 2.9 V, as expected.

For higher χ materials FNT is observed at lower voltages. The linear trends in the Fowler-Nordheim plots of HfO_2 and ZrO_2 demonstrate clear FNT mechanism. The onset voltage in each plot agrees with expectations based on the estimated values of electron affinity for both materials. TiO_2 and ZnO, which have $\chi \geq 3.9$ eV, should display FNT at significantly lower voltages. However, Fowler-Nordheim plots do not reveal FNT. Dominant conduction in these dielectrics involve bulk-limited mechanisms. The presence of traps (e.g. oxygen vacancies) in the bulk dielectric encourages conduction by enabling electrons to tunnel to, from, or in between traps [138]. This form of conduction is called trap-assisted tunneling (TAT). At sufficiently high bias, electrons can tunnel from a trap through a triangular barrier in a manner similar to FNT [139]. This form of TAT predicts current density of the form $I_{TAT} \sim \exp\left[-\frac{1}{V}\right]$ [140]. Alternatively, after tunneling to a trap, electrons can then be thermally emitted from the trap to the conduction band in the form of Poole-Frenkel emission (PFE). The thermal excitation of electrons in PFE is similar to Schottky emission, and is thus highly temperature dependent [82]. Consequently, device temperature sensitivity can be affected when PFE dominates conduction. In PFE, current depends on bias by $I \sim V \exp\left[\sqrt{V}\right]$ [80, 82, 141]. Therefore, the influence of PFE on conduction is revealed by linearity in a plot of $\ln(I/V)$ vs. $V^{\frac{1}{2}}$.

PFE and TAT mechanisms are dictated by trap depth and trap density, as well as the dielectric insulator barrier height. Poole-Frenkel emission and trap-assisted tunneling plots (Figure B.1(center, right)) elucidate the dominance of these mechanisms with high electron affinity materials. Bulk conduction mechanisms are first observed in HfO_2, and the bias under which these mechanisms manifest decreases as χ is increased. Lowering the energy barrier enables more tunneling to traps closer to the Fermi level and also makes for easier electron emission over the barrier; this is why we see the dominant conduction mechanism shift from direct tunneling and FNT to bulk-limited PFE and TAT mechanisms. Because of competing mechanisms, diode figures of merit are not strictly predisposed to tunneling barrier geometry.

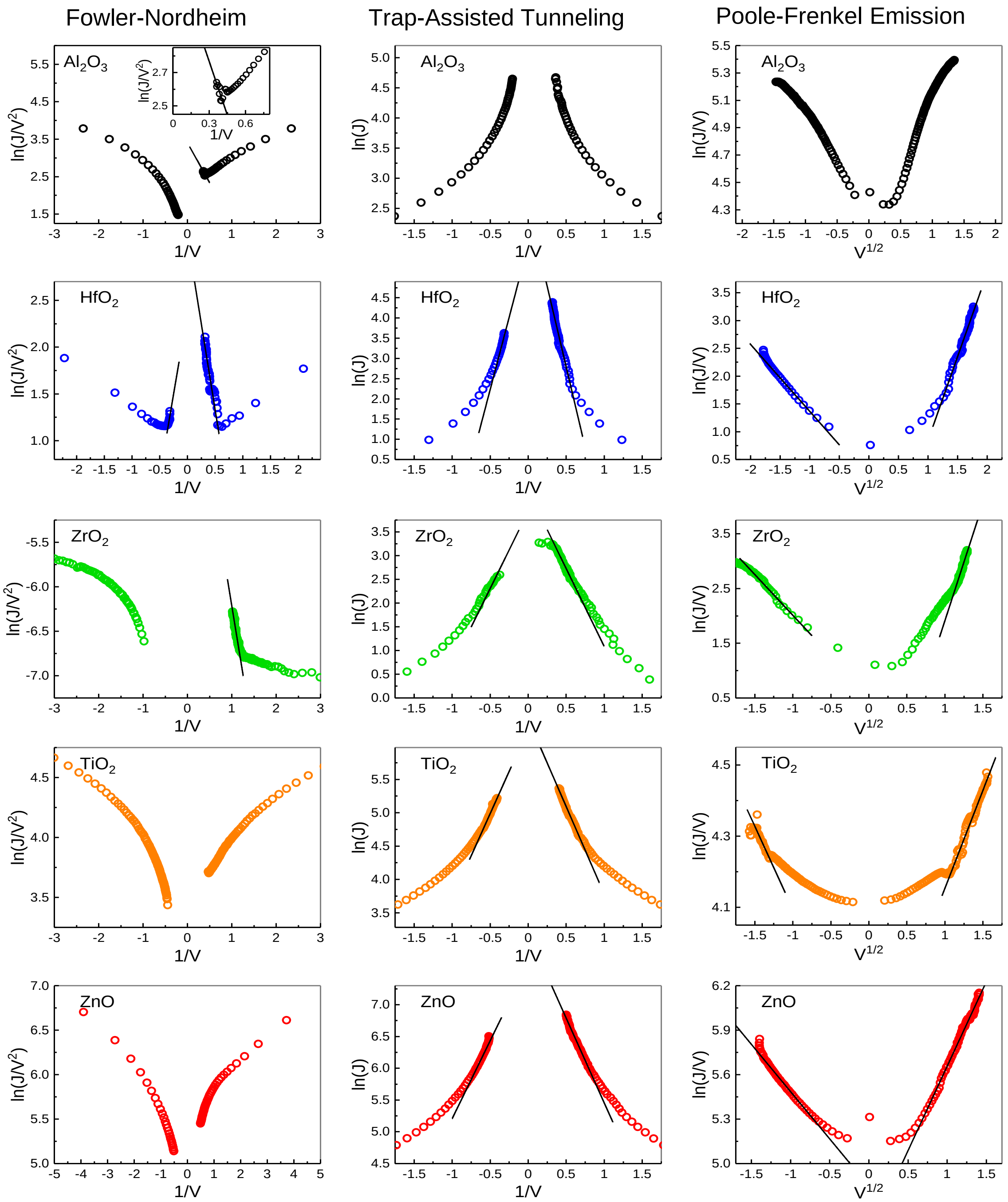

Figure B.1. Fowler-Nordheim tunneling (left), trap-assisted tunneling (center), and Poole-Frenkel emission (right) plots are shown for devices with various 6 nm oxides to illustrate conduction mechanism dependency. Solid black lines denote dominant conduction mechanisms determined by linear regression.

B.2 CI^{2}M Asymmetry–Voltage Curves

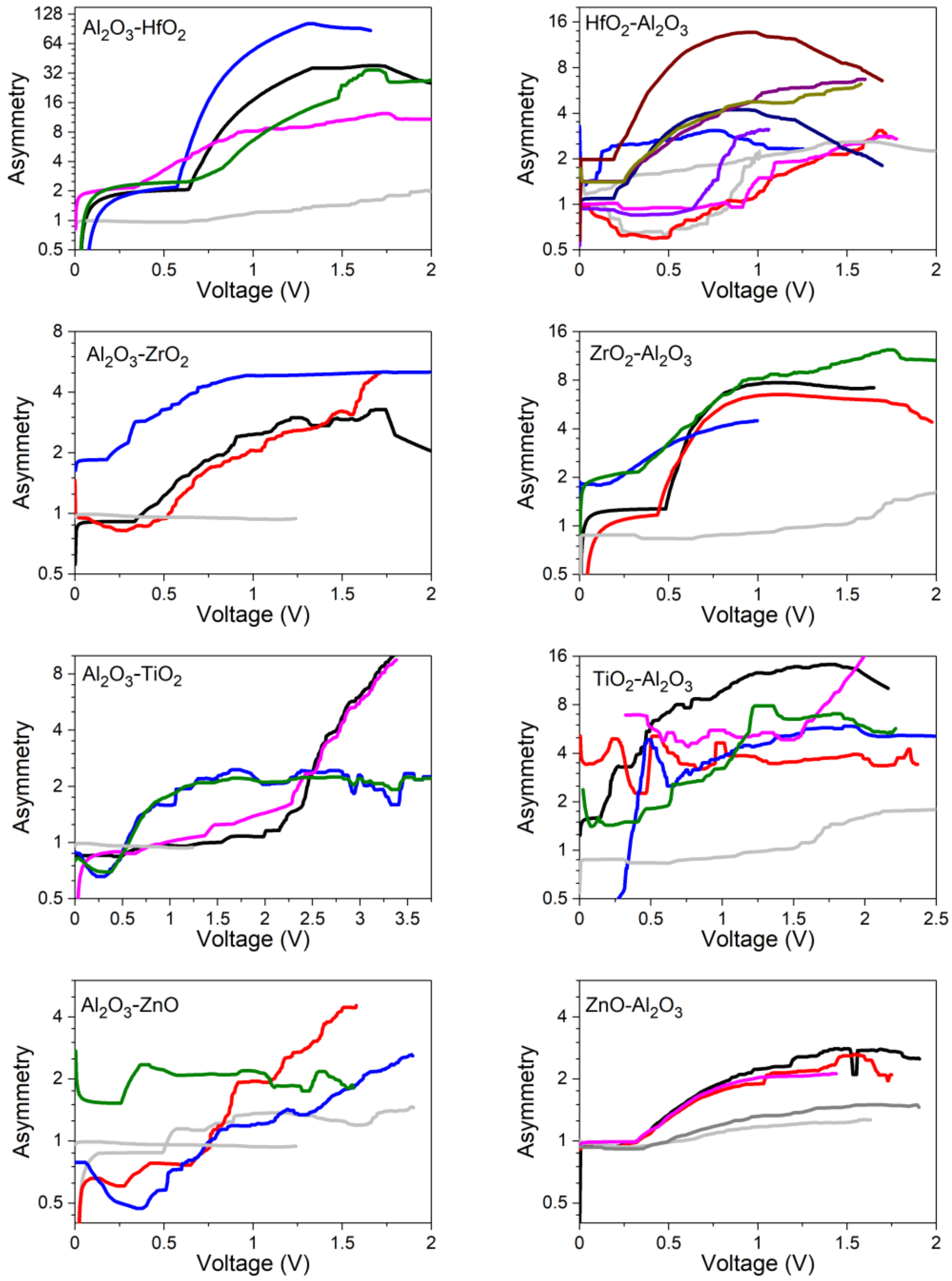

Figure B.2. Asymmetry, $\mathcal{A}(V)$, for various double-barrier CNT/I-I (4/4 nm)/Ag devices. Each plot shows measurements from different devices along a single sample to illustrate reproducibility and yield of good diodes. Gray lines represent non-yielding devices.

APPENDIX C. VERIFICATION OF PHOTON-ASSISTED TUNNELING MODEL

The validity of the developed PAT model is assessed by following the results reported in references [74, 92]. First, consider the case of an ideal, piecewise linear diode with zero reverse bias current and a linear forward bias current having a resistance of 50 Ω. Antenna resistance is assumed to be 100 Ω. With low photon energy of 4 meV and power of 200 µW we get classical operation ($V_\omega \gg V_{ph}$). The model gives classical behavior in Figure C.1(a) that matches reported PAT analyses [92]. Not only does the piecewise linear diode shift into the second quadrant, there is a distinct nonlinearity that is induced by the response of the low energy light.

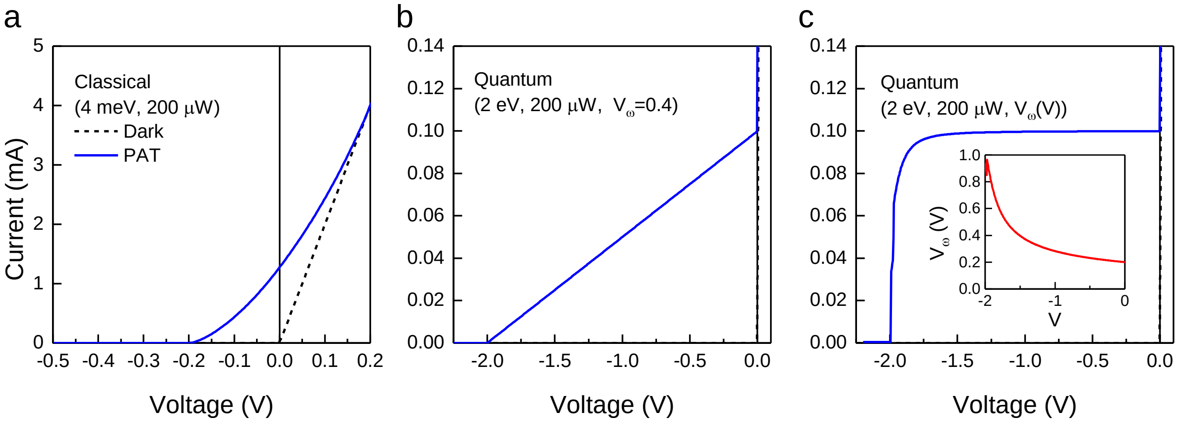

Figure C.1. PAT Model verification using an ideal piecewise linear diode with 50 Ω forward resistance. (a) Classical operation at 4 meV and 200 µW ($\alpha = 50$). (b-c) Quantum operation at 2 eV and 200 µW ($\alpha = 0.1$). (b) Operation under fixed a.c. diode voltage, $V_\omega = V_A/2 = 0.2$ V yields a linear region of second quadrant power generation. (c) Solving for $V_\omega(V)$ (inset) results in convex behavior in the second quadrant and more efficient energy harvesting.

For quantum regime operation through 2 eV and 200 µW, and also assuming fixed a.c. diode voltage mode, a triangle is formed in the second quadrant, intercepting at $-V_{oc} = V_{ph}$ (Figure C.1(b)). However, for rectenna operation under fixed incident power, rather than fixed a.c. voltage, there should be a quantum hump forming a convex *I*–*V* behavior in the second quadrant. For this model to accurately match prior calculations of rectenna response [74, 92], bias dependent $V_\omega(V)$ is calculated. The harmonic of a.c. rectified current, I_ω, is solved and fed into the relation $V_\omega = V_A - I_\omega R_A$. Results led to the approximately rectangular behavior (Figure C.1(c)), with slight curvature based on the chosen convergence criteria. The predicted a.c. voltage also matches expectations, depicted in the inset of Figure C.1(c), as V_ω increases rapidly as bias approaches $-V_{ph}$.

APPENDIX D. ALTERNATIVE PLANARIZATION ATTEMPTS

D.1 Infiltration with Thick Conformal ALD Coating

In an effort to encapsulate the CNT forest and planarize the array, this section will explore infiltration using ALD to make conformal coatings. Samples of aligned CNT forests, grown on Al foil, were used. The CNT forest was ~50 µm tall, with CNT diameters ~ 20 nm. The spacing between CNTs is expected to be around 40 nm, so in order to encapsulate the array, 40 nm of Al_2O_3 was deposited by ALD at 250 °C, using a similar process as discussed earlier. An initial treatment of 300 s O_2 plasma was used to functionalize the CNTs and facilitate conformal coating. The TMA and water vapor precursors were cycled with 30 s purge times between cycles with the goal of letting the precursors fully penetrate into the array. The deposition rate was ~ 1 Å/s.

<u>Results</u>

In Figure 8.4, SEM images of the Al_2O_3-coated CNT forest reveal that the oxide coating did not fully infiltrate the array. The 40 nm Al_2O_3 is localized at the uppermost ~ 3 µm of the total array. Top-down images indicate a nearly uniform surface is realized, but there are still miniscule gaps in the oxide coating. Electrically testing the samples confirmed that the CNT tips are completely insulated by the Al_2O_3. But since the Al_2O_3 does not fill the array, too much pressure applied by the electrical probe tips causes them to poke through the layer. The reason for the poor penetration and infiltration of the Al_2O_3 is clear. The average intertube spacing of CNTs in the arrays is ~40 nm. As a thin layer of Al_2O_3 starts to conformally deposit on the CNT walls, it will start to constrict the available space and make it harder for the ALD precursors to penetrate all the way into the array. This will inevitably form a dense enough layer so as to block further deposition of the oxide deeper in the array.

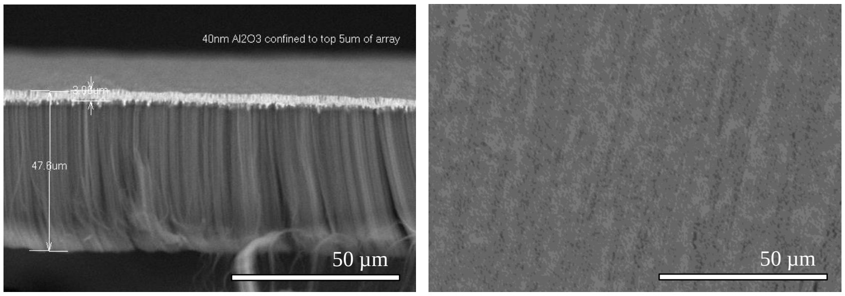

Figure D.1. (left) Side view and (right) top view SEM images of a CNT forest coated in 40 nm Al_2O_3 via ALD.

Recommendations

Longer purge times between ALD precursor cycles may be able to increase penetration of ALD within the array. Though this may assist the coating depth, even with the 30 s extended purge times used here, it is unlikely that extended purge times alone will be enough to fully encapsulate the array. Other researchers have attempted similar ALD infiltration with oxides and ceramics, and have had more success with pre-treating the CNTs, such as with O_2 plasma[142]. The 300 s O_2 plasma step our processes uses prior to the introduction of precursors was still not suitable for full Al_2O_3 infiltration. Another suggestion would be to introduce a plasma treatment between every few cycles to boost the functionalization of the CNTs.

Despite the downfalls of this method, still remain some potential for these samples to be used for planar infiltrated CNT electronics. It would be worthwhile to explore RIE as a method to etch away the upper portion of the Al_2O_3 coating in order to reveal the CNTs. The challenge lies with the precision and uniformity of an RIE process, which risks over-etching the oxide and create holes in the infiltrating oxide layer.

To conclude this attempt, since ALD-infiltration did not produce convincing results—and given the significant time and cost of such an extended ALD process—this work will move on to more commercially viable methods of encapsulating CNT arrays.

D.2 Polymer Dip Coating

The next attempt at planarizing CNT arrays involves infiltrating with polyimide (PI) in solution. PI is an insulating polymer material that is often used in optoelectronics, usually as the substrate. The goal here is to apply solution-processed PI to the CNT array.

PI was obtained from (Sigma Aldrich) and dissolved in dimethylformamide at 50 °C (concentration: 50 mg/mL). CNT arrays on Al foil were dip-coated in PI solution and suspended to remove excess polymer. They were then cured on a hotplate at 100 °C for 1 hr.

Results

The as-prepared PI-coated CNT samples were entirely electrically insulating. Therefore, to expose the CNTs beneath, samples were etched using RIE. Initially, 80 W O_2 plasma was used, but after as much as 10 min etch time, there was no quantifiable change in the PI-coated surface when observed under SEM. A more aggressive recipe was used to etch the PI using either 5:50 or 50:5 flow rate of CF_4:O_2 and between 5–20 min etching. The etching was too nonuniform, such that large swaths of CNTs were etched away and other regions were left entirely coated by PI. In part, the nonuniformity of the PI coating and the precision needed to etch down to the 10–100 µm array height, makes this method impractical.

REFERENCES

[1] W. Shockley and H. J. Queisser, “Detailed balance limit of efficiency of p-n junction solar cells,” *J. Appl. Phys.*, vol. 32, no. 3, pp. 510–519, 1961, doi: 10.1063/1.1736034.

[2] E. Donchev *et al.*, “The rectenna device: From theory to practice (a review),” *MRS Energy Sustain.*, vol. 1, p. E1, Jul. 2014, doi: 10.1557/mre.2014.6.

[3] R. Corkish, M. A. Green, and T. Puzzer, “Solar energy collection by antennas,” *Sol. Energy*, vol. 73, no. 6, pp. 395–401, Dec. 2002, doi: 10.1016/S0038-092X(03)00033-1.

[4] R. L. Bailey, “A Proposed New Concept for a Solar-Energy Converter,” *J. Eng. Power*, vol. 94, no. 2, p. 73, Apr. 1972, doi: 10.1115/1.3445660.

[5] S. Joshi and G. Moddel, “Efficiency limits of rectenna solar cells: Theory of broadband photon-assisted tunneling,” *Appl. Phys. Lett.*, vol. 102, no. 8, pp. 1–5, Feb. 2013, doi: 10.1063/1.4793425.

[6] S. Joshi and G. Moddel, “Optical rectenna operation: Where Maxwell meets Einstein,” *J. Phys. D. Appl. Phys.*, vol. 49, no. 26, p. 265602, 2016, doi: 10.1088/0022-3727/49/26/265602.

[7] E. Briones, J. Alda, and F. J. González, “Conversion efficiency of broad-band rectennas for solar energy harvesting applications,” *Opt. Express*, vol. 21, no. S3, p. A412, May 2013, doi: 10.1364/OE.21.00A412.

[8] A. Sharma, V. Singh, T. L. Bougher, and B. A. Cola, “A carbon nanotube optical rectenna,” *Nat. Nanotechnol.*, vol. 10, no. 12, pp. 1027–1032, 2015, doi: 10.1038/nnano.2015.220.

[9] S. Grover, O. Dmitriyeva, M. J. Estes, and G. Moddel, “Traveling-wave metal/insulator/metal diodes for improved infrared bandwidth and efficiency of antenna-coupled rectifiers,” *IEEE Trans. Nanotechnol.*, vol. 9, no. 6, pp. 716–722, Nov. 2010, doi: 10.1109/TNANO.2010.2051334.

[10] S. Grover and G. Moddel, “Applicability of Metal/Insulator/Metal (MIM) diodes to solar rectennas,” *IEEE J. Photovoltaics*, vol. 1, no. 1, pp. 78–83, 2011, doi: 10.1109/JPHOTOV.2011.2160489.

[11] M. N. Gadalla, M. Abdel-Rahman, and A. Shamim, “Design, Optimization and Fabrication of a 28.3 THz Nano-Rectenna for Infrared Detection and Rectification,” *Sci. Rep.*, vol. 4, no. 4270, pp. 1–9, 2014, doi: 10.1038/srep04270.

[12] G. Moddel and S. Grover, *Rectenna solar cells*, vol. 9781461437. 2013.

[13] G. Jayaswal, A. Belkadi, A. Meredov, B. Pelz, G. Moddel, and A. Shamim, “A Zero-Bias, Completely Passive 28 THz Rectenna for Energy Harvesting from Infrared (Waste Heat),” in *IEEE MTT-S International Microwave Symposium Digest*, 2018, pp. 355–358, doi: 10.1109/MWSYM.2018.8439447.

[14] J. Shank *et al.*, “Power Generation from a Radiative Thermal Source Using a Large-Area Infrared Rectenna,” *Phys. Rev. Appl.*, vol. 9, no. 5, p. 54040, 2018, doi: 10.1103/PhysRevApplied.9.054040.

[15] P. C. D. Hobbs, R. B. Laibowitz, F. R. Libsch, N. C. LaBianca, and P. P. Chiniwalla, “Efficient waveguide-integrated tunnel junction detectors at 1.6 µm,” *Opt. Express*, vol. 15, no. 25, p. 16376, Dec. 2007, doi: 10.1364/OE.15.016376.

[16] A. Sanchez, C. F. Davis, K. C. Liu, and A. Javan, “The MOM tunneling diode: Theoretical estimate of its performance at microwave and infrared frequencies,” *J. Appl. Phys.*, vol. 49, no. 10, pp. 5270–5277, Oct. 1978, doi: 10.1063/1.324426.

[17] J. Alda, J. M. Rico-García, J. M. López-Alonso, and G. Boreman, “Optical antennas for nano-photonic applications,” *Nanotechnology*, vol. 16, no. 5, pp. S230–S234, 2005, doi: 10.1088/0957-4484/16/5/017.

[18] P. Bharadwaj, B. Deutsch, and L. Novotny, “Optical Antennas,” *Adv. Opt. Photonics*, vol. 1, no. 3, pp. 438–483, 2009, doi: 10.1364/AOP.1.000438.

[19] L. Novotny and N. Van Hulst, “Antennas for light,” *Nat. Photonics*, vol. 5, no. 2, pp. 83–90, Feb. 2011, doi: 10.1038/nphoton.2010.237.

[20] D. R. Ward, F. HÜser, F. Pauly, J. C. Cuevas, and D. Natelson, “Optical rectification and field enhancement in a plasmonic nanogap,” *Nat. Nanotechnol.*, vol. 5, no. 10, pp. 732–736, 2010, doi: 10.1038/nnano.2010.176.

[21] E. A. Kadlec, R. L. Jarecki, A. Starbuck, D. W. Peters, and P. S. Davids, “Photon-Phonon-Enhanced Infrared Rectification in a Two-Dimensional Nanoantenna-Coupled Tunnel Diode,” *Phys. Rev. Appl.*, vol. 6, no. 6, Dec. 2016, doi: 10.1103/PhysRevApplied.6.064019.

[22] P. S. Davids *et al.*, “Infrared rectification in a nanoantenna-coupled metal-oxide-semiconductor tunnel diode,” *Nat. Nanotechnol.*, vol. 10, no. 12, pp. 1033–1038, 2015, doi: 10.1038/nnano.2015.216.

[23] Z. Zhu, S. Joshi, S. Grover, and G. Moddel, “Graphene geometric diodes for terahertz rectennas,” *J. Phys. D. Appl. Phys.*, vol. 46, no. 18, 2013, doi: 10.1088/0022-3727/46/18/185101.

[24] Z. Zhu, S. Joshi, S. Grover, and G. Moddel, “Geometric Diodes for Optical Rectennas,” in *Rectenna Solar Cells*, vol. 9781461437, New York, NY: Springer New York, 2013, pp. 209–227.

[25] S. Joshi, Z. Zhu, S. Grover, and G. Moddel, “Infrared optical response of geometric diode rectenna solar cells,” in *Conference Record of the IEEE Photovoltaic Specialists Conference*, 2012, no. V, pp. 2976–2978, doi: 10.1109/PVSC.2012.6318209.

[26] S. Iijima, “Helical microtubules of graphitic carbon,” *Nature*, vol. 354, no. 6348, pp. 56–58, 1991, doi: 10.1038/354056a0.

[27] Á. Kukovecz, G. Kozma, and Z. Kónya, “Multi-Walled Carbon Nanotubes,” in *Springer Handbook of Nanostructured Materials*, Springer-Verlag Berlin Heidelberg, 2013, p. 164.

[28] I.-Y. Jeon, D. W. Chang, N. Kumar, and J.-B. Baek, “Functionalization of Carbon Nanotubes,” *Carbon Nanotub. - Polym. Nanocomposites*, p. 450, 2011, doi: 10.5772/18396.

[29] S. Shahidi and B. Moazzenchi, “Carbon nanotube and its applications in textile industry – A review,” *J. Text. Inst.*, vol. 5000, pp. 1–14, 2018, doi: 10.1080/00405000.2018.1437114.

[30] K. Kempa *et al.*, “Carbon nanotubes as optical antennae,” *Adv. Mater.*, vol. 19, no. 3, pp. 421–426, Feb. 2007, doi: 10.1002/adma.200601187.

[31] G. W. Hanson, “Radiation efficiency of nano-radius dipole antennas in the microwave and far-infrared regimes,” *IEEE Antennas Propag. Mag.*, vol. 50, no. 3, pp. 66–77, Jun. 2008, doi: 10.1109/MAP.2008.4563565.

[32] G. W. Hanson, “Fundamental transmitting properties of carbon nanotube antennas,” *IEEE Trans. Antennas Propag.*, vol. 53, no. 11, pp. 3426–3435, Nov. 2005, doi: 10.1109/TAP.2005.858865.

[33] P. Mukherjee and B. Gupta, “Terahertz (THz) frequency sources and antennas - A brief review,” *Int. J. Infrared Millimeter Waves*, vol. 29, no. 12, pp. 1091–1102, Dec. 2008, doi: 10.1007/s10762-008-9423-0.

[34] L. Ren *et al.*, “Collective antenna effects in the terahertz and infrared response of highly aligned carbon nanotube arrays,” *Phys. Rev. B - Condens. Matter Mater. Phys.*, vol. 87, no. 16, p. 161401, Apr. 2013, doi: 10.1103/PhysRevB.87.161401.

[35] S. Joshi and G. Moddel, “Simple Figure of Merit for Diodes in Optical Rectennas,” *IEEE J. Photovoltaics*, vol. 6, no. 3, pp. 668–672, May 2016, doi: 10.1109/JPHOTOV.2016.2541460.

[36] G. Y. Slepyan, S. Vlasenko, and D. Mogilevtsev, “Quantum Antennas,” *Adv. Quantum Technol.*, p. 1900120, 2020, doi: 10.1002/qute.201900120.

[37] L. Novotny, “Effective wavelength scaling for optical antennas,” *Phys. Rev. Lett.*, vol. 98, no. 26, pp. 1–4, 2007, doi: 10.1103/PhysRevLett.98.266802.

[38] M. Y. Sfeir *et al.*, “Optical spectroscopy of individual single-walled carbon nanotubes of defined chiral structure,” *Science (80-.).*, vol. 312, no. 5773, pp. 554–556, Apr. 2006, doi: 10.1126/science.1124602.

[39] J. H. Shin *et al.*, “Ultrafast metal-insulator-multi-wall carbon nanotube tunneling diode employing asymmetrical structure effect,” *Carbon N. Y.*, vol. 102, pp. 172–180, 2016, doi: 10.1016/j.carbon.2016.02.035.

[40] Y. Wang *et al.*, “Receiving and transmitting light-like radio waves: Antenna effect in arrays of aligned carbon nanotubes,” *Appl. Phys. Lett.*, vol. 85, no. 13, pp. 2607–2609, 2004, doi: 10.1063/1.1797559.

[41] M. S. Eggleston, K. Messer, L. Zhang, E. Yablonovitch, and M. C. Wu, “Optical antenna enhanced spontaneous emission,” *Proc. Natl. Acad. Sci.*, vol. 112, no. 6, pp. 1704–1709, 2015, doi: 10.1073/pnas.1423294112.

[42] Y. Lan, B. Zeng, H. Zhang, B. Chen, and Z. Yang, “Simulation of carbon nanotube THz antenna arrays,” *Int. J. Infrared Millimeter Waves*, vol. 27, no. 6, pp. 871–877, Jun. 2006, doi: 10.1007/s10762-006-9123-6.

[43] Shilpi, K. Bhatt, Sandeep, S. Kumar, and C. C. Tripathi, “Potential challenges and issues in implementation of MIM diodes for rectenna application,” in *Proceedings of the International Conference on Inventive Communication and Computational Technologies, ICICCT 2017*, Mar. 2017, pp. 83–88, doi: 10.1109/ICICCT.2017.7975164.

[44] B. Eliasson, “Metal-Insulator-Metal Diodes For Solar Energy Conversion,” *PhD Thesis, Univ. Color. Boulder*, pp. 1–228, 2001, [Online]. Available: papers://eb55bc93-f531-4c22-b526-28517328312d/Paper/p1826.

[45] J. G. Simmons, “Electric Tunnel Effect between Dissimilar Electrodes Separated by a Thin Insulating Film John,” *J. Appl. Phys.*, vol. 34, no. 6, pp. 1793–1803, 1963, doi: 10.1063/1.1702682.

[46] T. E. Hartman, “Tunneling of a wave packet,” *J. Appl. Phys.*, vol. 33, no. 12, pp. 3427–3433, Dec. 1962, doi: 10.1063/1.1702424.

[47] M. Nagae, “Response time of metal-insulator-metal tunnel junctions,” *Jpn. J. Appl. Phys.*, vol. 11, no. 11, pp. 1611–1621, Nov. 1972, doi: 10.1143/JJAP.11.1611.

[48] J. J. Yang, M. D. Pickett, X. Li, D. A. A. Ohlberg, D. R. Stewart, and R. S. Williams, “Memristive switching mechanism for metal/oxide/metal nanodevices,” *Nat. Nanotechnol.*, vol. 3, no. 7, pp. 429–433, Jul. 2008, doi: 10.1038/nnano.2008.160.

[49] B. Govoreanu, C. Adelmann, A. Redolfi, L. Zhang, S. Clima, and M. Jurczak, “High-performance metal-insulator-metal tunnel diode selectors,” *IEEE Electron Device Lett.*, vol. 35, no. 1, pp. 63–65, Jan. 2014, doi:

10.1109/LED.2013.2291911.

[50] R. D. Clark, “Emerging applications for high K materials in VLSI technology,” *Materials*, vol. 7, no. 4. Multidisciplinary Digital Publishing Institute, pp. 2913–2944, Apr. 10, 2014, doi: 10.3390/ma7042913.

[51] W. den Boer, *Active Matrix Liquid Crystal Displays: Fundamentals and Applications*. Elsevier, 2005.

[52] E. C. Kinzel, R. L. Brown, J. C. Ginn, B. A. Lail, B. A. Slovick, and G. D. Boreman, “Design of an MOM diode-coupled frequency-selective surface,” *Microw. Opt. Technol. Lett.*, vol. 55, no. 3, pp. 489–493, Mar. 2013, doi: 10.1002/mop.27363.

[53] N. Alimardani and J. F. Conley, “Enhancing metal-insulator-insulator-metal tunnel diodes via defect enhanced direct tunneling,” *Appl. Phys. Lett.*, vol. 105, no. 8, pp. 1–6, 2014, doi: 10.1063/1.4893735.

[54] P. Maraghechi, A. Foroughi-Abari, K. Cadien, and A. Y. Elezzabi, “Enhanced rectifying response from metal-insulator-insulator-metal junctions,” *Appl. Phys. Lett.*, vol. 99, no. 253503, p. 253503, Dec. 2011, doi: 10.1063/1.3671071.

[55] N. Alimardani, S. W. King, B. L. French, C. Tan, B. P. Lampert, and J. F. Conley, “Investigation of the impact of insulator material on the performance of dissimilar electrode metal-insulator-metal diodes,” *J. Appl. Phys.*, vol. 116, no. 2, p. 024508, Jul. 2014, doi: 10.1063/1.4889798.

[56] N. Alimardani, J. M. McGlone, J. F. Wager, and J. F. Conley, “Conduction processes in metal–insulator–metal diodes with Ta 2 O 5 and Nb 2 O 5 insulators deposited by atomic layer deposition,” *J. Vac. Sci. Technol. A Vacuum, Surfaces, Film.*, vol. 32, no. 1, p. 01A122, Jan. 2014, doi: 10.1116/1.4843555.

[57] N. Alimardani *et al.*, “Impact of electrode roughness on metal-insulator-metal tunnel diodes with atomic layer deposited Al 2 O 3 tunnel barriers,” *J. Vac. Sci. Technol. A Vacuum, Surfaces, Film.*, vol. 30, no. 1, p. 01A113, Jan. 2012, doi: 10.1116/1.3658380.

[58] E. W. Cowell *et al.*, “Advancing MIM electronics: Amorphous metal electrodes,” *Adv. Mater.*, vol. 23, no. 1, pp. 74–78, 2011, doi: 10.1002/adma.201002678.

[59] I. E. Hashem, N. H. Rafat, and E. A. Soliman, “Theoretical study of metal-insulator-metal tunneling diode figures of merit,” *IEEE J. Quantum Electron.*, vol. 49, no. 1, pp. 72–79, Jan. 2013, doi: 10.1109/JQE.2012.2228166.

[60] A. Y. Elsharabasy, A. S. Negm, M. H. Bakr, and M. J. Deen, “Global Optimization of Rectennas for IR Energy Harvesting at 10.6 μ m,” *IEEE J. Photovoltaics*, vol. 9, no. 5, pp. 1232–1239, 2019, doi: 10.1109/jphotov.2019.2927142.

[61] S. B. Herner, A. Belkadi, A. Weerakkody, B. Pelz, and G. Moddel, “Responsivity-Resistance Relationship in MIIM Diodes,” *IEEE J. Photovoltaics*, pp. 1–6, 2018, doi: 10.1109/JPHOTOV.2018.2791421.

[62] S. Grover and G. Moddel, “Engineering the current-voltage characteristics of metal-insulator-metal diodes using double-insulator tunnel barriers,” *Solid. State. Electron.*, vol. 67, no. 1, pp. 94–99, 2012, doi: 10.1016/j.sse.2011.09.004.

[63] N. Alimardani and J. F. Conley, “Step tunneling enhanced asymmetry in asymmetric electrode metal-insulator-insulator-metal tunnel diodes,” *Appl. Phys. Lett.*, vol. 102, no. 14, pp. 1–6, 2013, doi: 10.1063/1.4799964.

[64] S. B. Herner, A. D. Weerakkody, A. Belkadi, and G. Moddel, “High performance MIIM diode based on cobalt oxide/titanium oxide,” *Cit. Appl. Phys. Lett*, vol. 110, p. 223901, 2017, doi: 10.1063/1.4984278.

[65] I. Nemr Noureddine, N. Sedghi, I. Z. Mitrovic, and S. Hall, “Barrier tuning of atomic layer deposited Ta2O5 and Al2O3 in double dielectric diodes,” *J. Vac. Sci. Technol. B, Nanotechnol. Microelectron. Mater. Process. Meas. Phenom.*, vol. 35, no. 1, p. 01A117, 2017, doi: 10.1116/1.4974219.

[66] A. Singh, R. Ratnadurai, R. Kumar, S. Krishnan, Y. Emirov, and S. Bhansali, “Fabrication and current-voltage characteristics of NiOx/ZnO based MIIM tunnel diode,” *Appl. Surf. Sci.*, vol. 334, pp. 197–204, 2015, doi: 10.1016/j.apsusc.2014.09.160.

[67] F. Aydinoglu *et al.*, “Higher Performance Metal-Insulator-Metal Diodes using Multiple Insulator Layers,” *Austin J. nanomedicine Nanotechnol.*, vol. 1, no. 1, pp. 3–5, 2014, [Online]. Available: http://austinpublishinggroup.com/nanomedicine-nanotechnology/fulltext/ajnn-v1-id1004.php.

[68] B. Pelz and G. Moddel, “Demonstration of distributed capacitance compensation in a metal-insulator-metal infrared rectenna incorporating a traveling-wave diode,” *J. Appl. Phys.*, vol. 125, no. 23, p. 234502, Jun. 2019, doi: 10.1063/1.5083155.

[69] Z. Zhu, S. Joshi, and G. Moddel, “High performance room temperature rectenna IR detectors using graphene geometric diodes,” *IEEE J. Sel. Top. Quantum Electron.*, vol. 20, no. 6, 2014, doi: 10.1109/JSTQE.2014.2318276.

[70] Y. Yao *et al.*, “Broad electrical tuning of graphene-loaded plasmonic antennas,” *Nano Lett.*, vol. 13, no. 3, pp. 1257–1264, 2013, doi: 10.1021/nl3047943.

[71] X. He *et al.*, “Carbon nanotube terahertz detector,” *Nano Lett.*, vol. 14, no. 7, pp. 3953–3958, 2014, doi: 10.1021/nl5012678.

[72] W. I. Milne *et al.*, “Carbon nanotubes as field emission sources,” *J. Mater. Chem.*, vol. 14, no. 6, pp. 933–943, Mar. 2004, doi: 10.1039/b314155c.

[73] P. K. Tien and J. P. Gordon, “Multiphoton process observed in the interaction of microwave fields with the tunneling between superconductor films,” *Phys. Rev.*, vol. 129, no. 2, pp. 647–651, 1963, doi: 10.1103/PhysRev.129.647.

[74] S. Grover, S. Joshi, and G. Moddel, “Quantum theory of operation for rectenna solar cells,” *J. Phys. D. Appl. Phys.*, vol. 46, no. 13, p. 135106, 2013, doi: 10.1088/0022-3727/46/13/135106.

[75] L. Li, “Study of Metal-Insulator-Metal Diodes for Photodetection,” 2013.

[76] J. R. Tucker and M. F. Millea, “Photon detection in nonlinear tunneling devices,” *Appl. Phys. Lett.*, vol. 33, no. 7, pp. 611–613, 1978, doi: 10.1063/1.90479.

[77] J. R. Tucker, “Quantum Limited Detection in Tunnel Junction Mixers,” *IEEE J. Quantum Electron.*, vol. 15, no. 11, pp. 1234–1258, 1979, doi: 10.1109/JQE.1979.1069931.

[78] J. R. Tucker and M. J. Feldman, “Quantum detection at millimeter wavelengths,” *Rev. Mod. Phys.*, vol. 57, no. 4, pp. 1055–1113, Oct. 1985, doi: 10.1103/RevModPhys.57.1055.

[79] E. H. Shah, B. Brown, and B. A. Cola, “A Study of Electrical Resistance in Carbon Nanotube-Insulator-Metal Diode Arrays for Optical Rectenna,” *IEEE Trans. Nanotechnol.*, vol. 16, no. 2, pp. 230–238, Mar. 2017, doi: 10.1109/TNANO.2017.2656066.

[80] J. G. Simmons, “Conduction in thin dielectric films,” *J. Phys. D. Appl. Phys.*, vol. 4, no. 5, pp. 613–657, 1971, doi: 10.1088/0022-3727/4/5/202.

[81] K. Mistry, M. Yavuz, and K. P. Musselman, “Simulated electron affinity tuning in metal-insulator-metal (MIM) diodes,” *J. Appl. Phys.*, vol. 121, no. 18, p. 184504, 2017, doi: 10.1063/1.4983256.

[82] F.-C. Chiu, “A Review on Conduction Mechanisms in Dielectric Films,” *Adv. Mater. Sci. Eng.*, vol. 2014, pp. 1–18, Feb. 2014, doi: 10.1155/2014/578168.

[83] M. Houssa *et al.*, “Trap-assisted tunneling in high permittivity gate dielectric stacks,” *J. Appl. Phys.*, vol. 87, no. 12, p. 8615, 2000, doi: 10.1063/1.373587.

[84] G. R. Berdiyorov and H. Hamoudi, “Doping-Enhanced Current Rectification in Carbon Nanotube–Metal Junctions for Rectenna Applications,” *ACS Omega*, vol. 5, no. 1, pp. 189–196, Jan. 2020, doi: 10.1021/acsomega.9b02352.

[85] J. A. Bean, B. Tiwari, G. H. Berstein, P. Fay, and W. Porod, “Thermal Infrared Detection Using Antenna-Coupled Metal-Oxide-Metal Diodes,” *J. Vac. Sci. Technol. B Microelectron. Nanom. Struct. Process. Meas. Phenom.*, vol. 27, no. 1, pp. 11–14, 2009, doi: 10.1116/1.3039684.

[86] E. C. Anderson, T. L. Bougher, and B. A. Cola, “High Performance Multiwall Carbon Nanotube–Insulator–Metal Tunnel Diode Arrays for Optical Rectification,” *Adv. Electron. Mater.*, vol. 4, no. 3, p. 1700446, Jan. 2018, doi: 10.1002/aelm.201700446.

[87] E. C. Anderson and B. A. Cola, “Photon-Assisted Tunneling in Carbon Nanotube Optical Rectennas: Characterization and Modeling,” *ACS Appl. Electron. Mater.*, vol. 1, no. 5, pp. 692–700, 2019, doi: 10.1021/acsaelm.9b00058.

[88] F. Zhuge *et al.*, “Nanostructured Materials and Architectures for Advanced Infrared Photodetection,” *Adv. Mater. Technol.*, vol. 2, no. 8, p. 1700005, Aug. 2017, doi: 10.1002/admt.201700005.

[89] A. Rogalski, “Infrared detectors: An overview,” *Infrared Phys. Technol.*, vol. 43, no. 3–5, pp. 187–210, 2002, doi: 10.1016/S1350-4495(02)00140-8.

[90] X. W. Tu, J. H. Lee, and W. Ho, “Atomic-scale rectification at microwave frequency,” *J. Chem. Phys.*, vol. 124, no. 2, p. 021105, Jan. 2006, doi: 10.1063/1.2159491.

[91] E. Briones *et al.*, “Seebeck Nanoantennas for Infrared Detection and Energy Harvesting Applications,” *9th Eur. Conf. Antennas Propag.*, vol. 1, no. June, 2014, [Online]. Available: http://arxiv.org/abs/1412.2658.

[92] S. Joshi and G. Moddel, “Rectennas at optical frequencies: How to analyze the response,” *J. Appl. Phys.*, vol. 118, no. 8, pp. 1–6, 2015, doi: 10.1063/1.4929648.

[93] A. Belkadi, A. Weerakkody, and G. Moddel, “Large Errors from Assuming Equivalent DC and High-Frequency Electrical Characteristics in Metal-Multiple-Insulator-Metal Diodes,” *ACS Photonics*, vol. 5, no. 12, pp. 4776–4780, 2018, doi: 10.1021/acsphotonics.8b01399.

[94] R. L. Olmon and M. B. Raschke, “Antenna-load interactions at optical frequencies: Impedance matching to quantum systems,” *Nanotechnology*, vol. 23, no. 44. p. 444001, Nov. 09, 2012, doi: 10.1088/0957-4484/23/44/444001.

[95] H. Fischer and O. J. F. Martin, “Engineering the optical response of plasmonic nanoantennas,” *Opt. Express*, vol. 16, no. 12, p. 9144, Jun. 2008, doi: 10.1364/OE.16.009144.

[96] E. C. Anderson, T. L. Bougher, and B. A. Cola, “High Performance Multi-Insulator Carbon Nanotube Tunnel Diode Arrays,” in *Proceedings of the 16th International Heat Transfer Conference*, 2018, pp. 6977–6984, doi: 10.1615/IHTC16.nmt.023033.

[97] D. Trivich, P. A. Flinn, F. Daniels, and J. A. Duffie, “Maximum efficiency of solar energy conversion by quantum processes,” in *Solar Energy Research*, Univ. of Wisconsin Press, 1955, p. 143.

[98] D. Dregely, K. Lindfors, M. Lippitz, N. Engheta, M. Totzeck, and H. Giessen, “Imaging and steering an optical wireless nanoantenna link,” *Nat. Commun.*, vol. 5, no. 1, p. 4354, Jul. 2014, doi: 10.1038/ncomms5354.

[99] C. Song, Y. Huang, J. Zhou, J. Zhang, S. Yuan, and P. Carter, “A high-efficiency broadband rectenna for ambient wireless energy harvesting,” *IEEE Trans. Antennas Propag.*, vol. 63, no. 8, pp. 3486–3495, Aug. 2015, doi: 10.1109/TAP.2015.2431719.

[100] Z. Ma and G. A. E. Vandenbosch, “Optimal solar energy harvesting efficiency of nano-rectenna systems,” *Sol. Energy*, vol. 88, pp. 163–174, 2013, doi: 10.1016/j.solener.2012.11.023.

[101] E. H. Sargent, “Solution-processed infrared optoelectronics: Photovoltaics, sensors, and sources,” *IEEE J. Sel. Top. Quantum Electron.*, vol. 14, no. 4, pp. 1223–1229, 2008, doi: 10.1109/JSTQE.2008.925766.

[102] L. Yang, S. Wang, Q. Zeng, Z. Zhang, and L.-M. Peng, “Carbon Nanotube Photoelectronic and Photovoltaic Devices and their Applications in Infrared Detection,” *Small*, vol. 9, no. 8, pp. 1225–1236, Apr. 2013, doi: 10.1002/smll.201203151.

[103] T. F. Zhang *et al.*, “Broadband photodetector based on carbon nanotube thin film/single layer graphene Schottky junction,” *Sci. Rep.*, vol. 6, no. 1, p. 38569, Dec. 2016, doi: 10.1038/srep38569.

[104] S. R. Kasjoo and A. M. Song, “Terahertz detection using nanorectifiers,” *IEEE Electron Device Lett.*, vol. 34, no. 12, pp. 1554–1556, 2013, doi: 10.1109/LED.2013.2285162.

[105] M. Zhang and J. T. W. Yeow, “A flexible, scalable, and self-powered mid-infrared detector based on transparent PEDOT: PSS/graphene composite,” *Carbon N. Y.*, vol. 156, pp. 339–345, Jan. 2020, doi: 10.1016/j.carbon.2019.09.062.

[106] A. Kim, Y. Won, K. Woo, S. Jeong, and J. Moon, “All-solution-processed indium-free transparent composite electrodes based on Ag nanowire and metal oxide for thin-film solar cells,” *Adv. Funct. Mater.*, vol. 24, no. 17, pp. 2462–2471, 2014, doi: 10.1002/adfm.201303518.

[107] Y. Zhou *et al.*, “A Universal Method to Produce Low-Work Function Electrodes for Organic Electronics,” *Science (80-.).*, vol. 336, no. 6079, pp. 327–332, 2012, doi: 10.1126/science.1218829.

[108] A. H. Alshehri *et al.*, “Quantum-Tunneling Metal-Insulator-Metal Diodes Made by Rapid Atmospheric Pressure Chemical Vapor Deposition,” *Adv. Funct. Mater.*, vol. 29, no. 7, pp. 1–8, 2019, doi: 10.1002/adfm.201805533.

[109] D. Matsuura, M. Shimizu, and H. Yugami, “High-current density and high-

asymmetry MIIM diode based on oxygen-non-stoichiometry controlled homointerface structure for optical rectenna,” *Sci. Rep.*, vol. 9, no. 1, p. 19639, Dec. 2019, doi: 10.1038/s41598-019-55898-x.

[110] A. Kaur and P. Chahal, “RF Characterization of NiO and TiO2 based metal-insulator-metal (MIM) diodes on flexible substrates,” *IEEE Access*, vol. 6, pp. 55653–55660, 2018, doi: 10.1109/ACCESS.2018.2871635.

[111] D. Etor, L. E. Dodd, D. Wood, and C. Balocco, “High-performance rectifiers fabricated on a flexible substrate,” *Appl. Phys. Lett.*, vol. 109, no. 19, p. 193110, Nov. 2016, doi: 10.1063/1.4967190.

[112] T. Souier, M. Stefancich, and M. Chiesa, “Characterization of multi-walled carbon nanotube–polymer nanocomposites by scanning spreading resistance microscopy,” *Nanotechnology*, vol. 23, no. 40, p. 405704, 2012, doi: 10.1088/0957-4484/23/40/405704.

[113] V. Ghai, H. Singh, and P. K. Agnihotri, “Near perfect thin film flexible broadband optical absorber with high thermal/electrical conductivity,” *J. Appl. Polym. Sci.*, vol. 48855, pp. 1–7, 2019, doi: 10.1002/app.48855.

[114] K. E. Plass *et al.*, “Flexible polymer-embedded Si wire arrays,” *Adv. Mater.*, vol. 21, no. 3, pp. 325–328, Jan. 2009, doi: 10.1002/adma.200802006.

[115] F. Du, L. Qu, Z. Xia, L. Feng, and L. Dai, “Membranes of vertically aligned superlong carbon nanotubes,” *Langmuir*, vol. 27, no. 13, pp. 8437–8443, 2011, doi: 10.1021/la200995r.

[116] J. Ouyang, C. W. Chu, F. C. Chen, Q. Xu, and Y. Yang, “High-conductivity poly(3,4-ethylenedioxythiophene):poly(styrene sulfonate) film and its application in polymer optoelectronic devices,” *Adv. Funct. Mater.*, vol. 15, no. 2, pp. 203–208, Feb. 2005, doi: 10.1002/adfm.200400016.

[117] J. G. Simmons, “Generalized Formula for the Electric Tunnel Effect between Similar Electrodes Separated by a Thin Insulating Film,” *J. Appl. Phys.*, vol. 34, no. 6, pp. 1793–1803, 1963, doi: 10.1063/1.1702682.

[118] R. A. Yotter and D. M. Wilson, “A review of photodetectors for sensing light-emitting reporters in biological systems,” *IEEE Sensors Journal*, vol. 3, no. 3. pp. 288–303, Jun. 2003, doi: 10.1109/JSEN.2003.814651.

[119] D. A. B. Miller, “Device requirements for optical interconnects to silicon chips,” *Proc. IEEE*, vol. 97, no. 7, pp. 1166–1185, 2009, doi: 10.1109/JPROC.2009.2014298.

[120] M. L. Brongersma, R. Zia, and J. A. Schuller, “Plasmonics - The missing link between nanoelectronics and microphotonics,” *Appl. Phys. A Mater. Sci. Process.*, vol. 89, no. 2, pp. 221–223, 2007, doi: 10.1007/s00339-007-4151-1.

[121] G. Rajan, Y. Semenova, J. Mathew, and G. Farrell, “Experimental analysis and demonstration of a low cost fibre optic temperature sensor system for engineering applications,” *Sensors Actuators, A Phys.*, vol. 163, no. 1, pp. 88–95, Sep. 2010, doi: 10.1016/j.sna.2010.07.010.

[122] A. Alù and N. Engheta, “Input impedance, nanocircuit loading, and radiation tuning of optical nanoantennas,” *Phys. Rev. Lett.*, vol. 101, no. 4, pp. 1–4, 2008, doi: 10.1103/PhysRevLett.101.043901.

[123] A. Dasgupta, M. M. Mennemanteuil, M. Buret, N. Cazier, G. Colas-Des-Francs, and A. Bouhelier, “Optical wireless link between a nanoscale antenna and a transducing rectenna,” *Nat. Commun.*, vol. 9, no. 1, pp. 1–7, Dec. 2018, doi: 10.1038/s41467-018-04382-7.

[124] C. Liu, P. Chen, and K. Li, “A 500 W low-temperature thermoelectric generator: Design and experimental study,” *Int. J. Hydrogen Energy*, vol. 39, no. 28, pp. 15497–15505, Sep. 2014, doi: 10.1016/j.ijhydene.2014.07.163.

[125] E. Tervo, E. Bagherisereshki, and Z. Zhang, “Near- field radiative thermoelectric energy converters : a review,” vol. 1, no. c, pp. 1–17, 2017.

[126] S. J. Byrnes, R. Blanchard, and F. Capasso, “Harvesting renewable energy from Earth’s mid-infrared emissions,” *Proc. Natl. Acad. Sci.*, vol. 111, no. 11, pp. 3927–3932, 2014, doi: 10.1073/pnas.1402036111.

[127] A. J. Nozik, G. Conibeer, and M. C. Beard, “Quantum Rectennas for Photovoltaics,” in *Advanced Concepts in Photovoltaics*, The Royal Society of Chemistry, 2014, pp. 506–546.

[128] N. M. Miskovsky *et al.*, “Nanoscale devices for rectification of high frequency radiation from the infrared through the visible: A new approach,” *Journal of Nanotechnology*, vol. 2012. Hindawi Publishing Corporation, 2012, doi: 10.1155/2012/512379.

[129] R. A. Hanel *et al.*, “The Nimbus 4 infrared spectroscopy experiment: 1. Calibrated thermal emission spectra,” *J. Geophys. Res.*, vol. 77, no. 15, pp. 2629–2641, May 1972, doi: 10.1029/JC077i015p02629.

[130] Z. Zhu, “Graphene Geometric Diodes for Optical Rectennas,” University of Colorado Boulder, 2014.

[131] B. Pelz, “Traveling-wave metal-insulator-metal diodes for infrared rectennas,” University of Colorado Boulder, 2018.

[132] S. Monaghan, P. K. Hurley, K. Cherkaoui, M. A. Negara, and A. Schenk, “Determination of electron effective mass and electron affinity in HfO2 using MOS and MOSFET structures,” *Solid. State. Electron.*, vol. 53, no. 4, pp. 438–444, Apr. 2009, doi: 10.1016/j.sse.2008.09.018.

[133] J. W. Yoon, T. Sasaki, and N. Koshizaki, “Dispersion of nanosized noble metals in TiO2 matrix and their photoelectrode properties,” *Thin Solid Films*, vol. 483, no. 1–2, pp. 276–282, Jul. 2005, doi: 10.1016/j.tsf.2005.01.006.

[134] S. K. Kim, W. D. Kim, K. M. Kim, C. S. Hwang, and J. Jeong, “High dielectric constant TiO2 thin films on a Ru electrode grown at 250°C by atomic-layer deposition,” *Appl. Phys. Lett.*, vol. 85, no. 18, pp. 4112–4114, Nov. 2004, doi: 10.1063/1.1812832.

[135] Y. T. Shih, M. K. Wu, M. J. Chen, Y. C. Cheng, J. R. Yang, and M. Shiojiri, “ZnO-based heterojunction light-emitting diodes on p-SiC(4H) grown by atomic layer deposition,” *Appl. Phys. B Lasers Opt.*, vol. 98, no. 4, pp. 767–772, 2010, doi: 10.1007/s00340-009-3809-0.

[136] J. R. Martínez-Castelo *et al.*, “Structural and electrical characterization of multilayer Al2O3/ZnO nanolaminates grown by atomic layer deposition,” *Mater. Sci. Semicond. Process.*, vol. 71, 2017, doi: 10.1016/j.mssp.2017.08.007.

[137] J. Robertson and B. Falabretti, “Band offsets of high K gate oxides on III-V semiconductors,” *J. Appl. Phys.*, vol. 100, no. 1, 2006, doi: 10.1063/1.2213170.

[138] S. Yu, X. Guan, and H.-S. P. Wong, “Conduction mechanism of TiN/HfO x /Pt resistive switching memory: A trap-assisted- tunneling model,” *Appl. Phys. Lett*, vol. 99, no. 063507, 2011, doi: 10.1063/1.3624472.

[139] M. P. Houng, Y. H. Wang, and W. J. Chang, “Current transport mechanism in trapped oxides: A generalized trap-assisted tunneling model,” *J. Appl. Phys.*, vol. 86, no. 3, pp. 1488–1491, Jul. 1999, doi: 10.1063/1.370918.

[140] X. Yan, Z. Zhou, B. Ding, J. Zhao, and Y. Zhang, “Superior resistive switching memory and biological synapse properties based on a simple TiN/SiO2/p-Si tunneling junction structure,” *J. Mater. Chem. C*, vol. 5, pp. 2259–2267, 2017, doi: 10.1039/c6tc04261a.

[141] G. González-Cordero, F. Jiménez-Molinos, J. B. Roldán, M. B. González, and F. Campabadal, “In-depth study of the physics behind resistive switching in TiN/Ti/HfO 2 /W structures,” *J. Vac. Sci. Technol. B, Nanotechnol. Microelectron. Mater. Process. Meas. Phenom.*, vol. 35, no. 1, p. 01A110, Jan. 2017, doi: 10.1116/1.4973372.

[142] Q. M. Zou *et al.*, “Thermally Stable and Electrically Conductive, Vertically Aligned Carbon Nanotube/Silicon Infiltrated Composite Structures for High-Temperature Electrodes,” *ACS Appl. Mater. Interfaces*, vol. 9, no. 42, pp. 37340–37349, 2017, doi: 10.1021/acsami.7b12087.